AMSLLE PUBLIC LUMBERT

# **JOURNAL**

A PUBLICATION OF THE AMERICAN ROCKET SOCIETY VOLUME 30 NUMBER 7 **JULY 1960** 



bilique Shock Relations for Air at Mach 7.5 and 7200 R Stagnation Temperature
H. T. Nagamateu, J. B. Workman and R. E. Sheer Jr. 619

Effect on a Rocket of the Oblateness of a Planet ..... William A. Allen 623

### FECHNICAL NOTES

RUSSIAN SUPPLEMENT 657-704



### because this oxidizer's stored aboard

Nitrogen Tetroxide provides immediate, hypergolic ignition with amine fuels. Even after 9 years of storage, nitrogen tetroxide is ready for instant use. Combustion efficiencies closely approach the theoretical 99%.

N<sub>2</sub>O<sub>4</sub>—Requires no refrigeration—can be stored indefinitely in missiles at launching sites.—Can be used with most fuels—including those containing carbon.—Eliminates rough starts—fast reaction prevents accumulation of propellants in thrust chambers.—Allows throttleable control of motors.

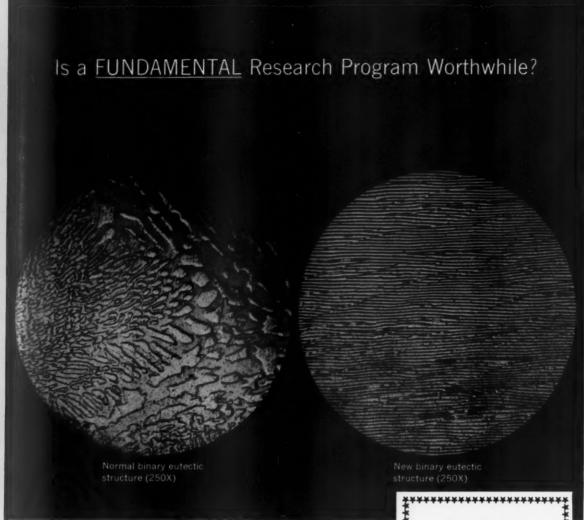
We'll gladly supply technical literature, including: a 59-page Product Bulletin, and a brochure entitled "Large Scale Handling of Nitrogen Tetroxide."

For specifications and local offices, see our insert in Chemical Materials Catalog, pages 475-482 and in Chemical Week Buyers Guide, pages 37-44.

BASIC TO AMERICA'S PROGRESS



NITROGEN DIVISION
Dept. NT14-21-1, 40 Rector Street, New York 6, N.Y.



We, at the Research Laboratories, are convinced that it is worthwhile. For example, one of the fundamental scientific programs being undertaken is a study of the mechanism of solidification of polyphase alloys.

This study is still in its early stages. However, we now have a better understanding of the solidification process. And we have demonstrated that the microstructure of certain eutectics can be significantly altered by controlled solidification. The contrast is illustrated above.

It is possible that these binary alloys with preferred orientation may have unusual physical and mechanical properties.

Perhaps you are interested in corporate—sponsored studies into the fundamental nature of matter. If so, we can offer a research environment that seems to stimulate scientists to extra achievement. It may be due to the way we encourage an internal crossfertilization of ideas; or because of a unique complex of complementary services that free the scientist from routine analysis and experimental chores.

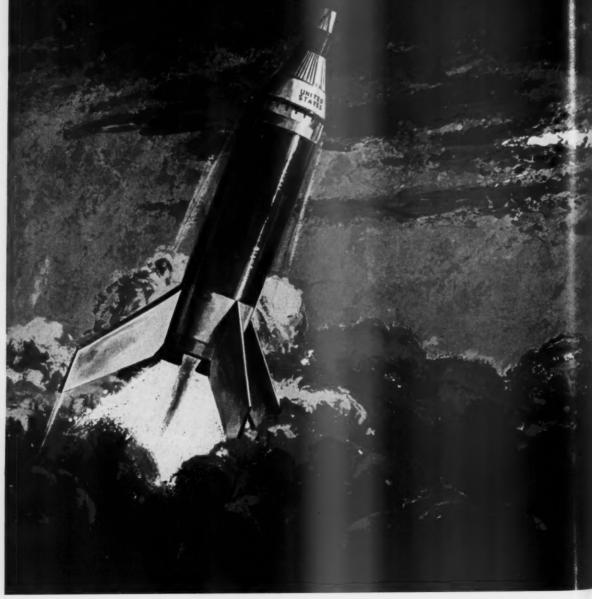
RESEARCH LABORATORIES

400 Main Street, East Hartford 8, Conn.

Opportunities for scientists in the physics of solids, liquids, gases, and plasmas. Current studies range from the fundamental properties of matter to the application of scientific knowledge to promising new products.

For more specific information, please write to Mr. W. F. Walsh, at the Research Laboratories.

# NASA / Little Joe



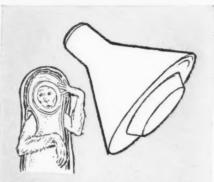
# Consistently successful flight performance in Project Mercury confirms unsurpassed reliability of THIOKOL solid rocket motors.

Time after time, NASA's workhorse, Little Joe, has soared into space, checking out the workability of materials, propulsion and escape systems, and reaction of research animals to the environment of space flight.

Pollux, Recruit, Castor—solid rocket motors from THIOKOL'S Elkton and Redstone Divisions—have unfailingly provided the thrust and power for Little Joe in its developmental flights.

THIOKOL's record of propulsion reliability in the spatial program is long and brilliant, reaching back to the X-17 which flew successfully in 96% of its launches, and to earlier research vehicles.

In NASA's Little Joe series, THIOKOL booster motors in various configurations have developed up to 250,000 lbs. thrust, today's ICBM class. Smaller THIOKOL rockets have been used to free escape capsule from booster.



Little Joe has carried this research and development capsule and research animals to varying altitudes to obtain engineering and medical data prior to launching man into orbit with subsequent safe recovery. The reliable THIOKOL solid rocket motors used in these missions are virtually off-the-shelf items and are available to other research groups.

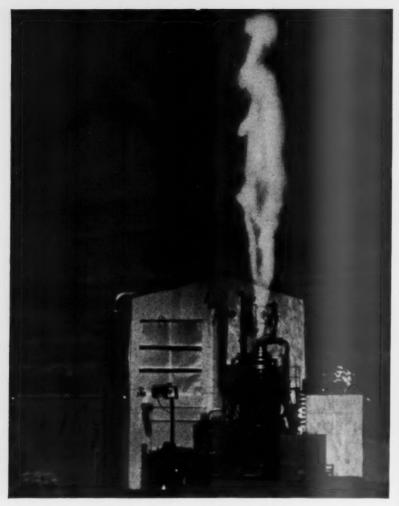
# Thiokol® Chemical Corporation BRISTOL, PENNA.

Plants in:

TRENTON, N. J.; MOSS POINT, MISS.; DENVILLE, N. J.; ELKTON, MD.; HUNTSVILLE, ALA.;

MARSHALL, TEXAS; BRIGHAM CITY, UTAH.

® Registered trademark of the Thiokol Chemical Corporation for its liquid polymers, rocket propellants, plasticizers, and other chemical products.



# Space Propulsion for the future . . .

from the MI family of Nuclear Reactors

Los Alamos Scientific Laboratory has the major responsibility for research, development and testing in the AEC-NASA Rover program . . . another of the many investigations at Los Alamos into peacetime uses of nuclear energy.

PHOTO: First field test of a KIWI nuclear propulsion reactor.

For employment information write: Personnel Director Division 60-61



### Scope of ARS JOURNAL

Scope of ARS JOURNAL

This Journal is devoted to the advancement of astronautics through the dissemination of original papers disclosing new scientific knowledge and basic applications of such knowledge. The sciences of astronautics are understood here to embrace scleeted aspects of jet and rocket propulsion, spacedight mechanics, high speed aerodynamics, flight guidance, space communications, atmospheric and outer space physics, materials and structures, human engineering, overall system analysis, and possibly certain other scientific areas. The selection of papers to be printed will be governed by the pertinence of the topic to the field of astronautics, by the current or probable future significance of the research, and by the importance of distributing the information to the members of the Society and to the profession at large.

### Information for Authors

Information for Authors

Manuscripts must be as brief as the proper presentation of the ideas will allow. Exclusion of dispensable material and comiseness of expression will influence the Editors' acceptance of a manuscript. In term of standard-size double-spaced typed pages a typical maximum length is 22 pages of ext (including equations). I page of referes es, I page of abstract and 12 illustrations. Fewerillustrations permit more text, and ice versa. Greater length will be acceptable only in exceptional cases.

Short manuscripts, more than one quarter of the maximum length stated for ull articles, may qualify for publication as Technical Motes or Technical Comments. They may be devoted to new developments requiring prompt disclosure or to comments on previously published papers. Such manuscripts are published within a few months of the date of receipt.

Sponsored manuscripts are published erequirements as to subject, scope or length, but which nevertheless deserves widespread distribution among jet propulsion engineers, may be printed as an extra part of the Journal or as a special supplement, if the author or his sponsor will reimburse the Society for actual publication costs. Estimates are available on request. Acknowledgment of such financial sponsorship appears as a footnote on the first page of the article, Publication is prompt since such papers are not in the ordinary backlog.

Manuscripts must be double spaced on one side of paper only with wide margins to allow for instructions to printer. Include a 100 to 200 word abstract. State the authors' positions and affiliations in a footnote on the first page. Equations and symbols may be handwritten, distinguish between capital and lower case letters, and indicate subscripts and superscripts. References are to be grouped at the end of the manuscript and are to be given as follows. For journal, volume, year, page numbers; for books: Authors first, then title, publisher, city, edition and page or chapter numbers. Line drawings must be clear and sharp to make

Submit manuscripts in duplicate (original plus first carbon, with two sets of illustrations) to the Managing Editor, ARS JOURNAL, 500 Fifth Avenue, New York 36, N.Y.

AGENEAL, 500 Fifth Avenue, New York 36, N.Y.

ARS JOURNAL is published monthly by the American Rocket Society, Inc. and the American Interplanetary Society at 20th & Northampton Sts., Easton, Pa., U.S. A. Editorial offices: 500 Fifth Ave., New York 36, N. Y. Price: \$12.50 per year, \$2.00 per single copy. Second-class mail privileges authorized at Easton, Pa. This publication is authorized to be mailed at the special rates of postage prescribed by Section 132.122. Notice of change of address should be sent to the Secretary, ARS, at least 30 days prior to publication. Opinions expressed herein are the authors' and do not necessarily reflect the views of the Editors or of the Society. © Copyright 1960 by the American Rocket Society, Inc.

ARS JOURNAL

JULY 19

Multi-Use Automated Maintenance

# DIF



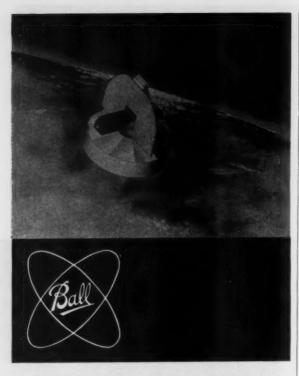
The recent demonstration of multi-purpose test equipment (MPTE), developed by RCA under a series of Army Ordnance contracts, highlights a new dimension in automated multi-use systems support and culminates a long-term RCA effort in this field. This General Evaluation Equipment is an automated, transistorized, dynamic checkout system. It contains a completely modularized array of electronic and mechanical

evaluation equipment, capable of checking a variety of electromechanical devices, ranging from radar subassemblies to missile guidance computers. MPTE provides the stimuli, programming, control, measurement and test functions for the NIKE AJAX, NIKE HERCULES, LACROSSE, HAWK and CORPORAL missile systems and has been extended to other weapons systems related to our defense efforts.



# RADIO CORPORATION of AMERICA

DEFENSE ELECTRONIC PRODUCTS
CAMDEN, NEW JERSEY



# **CONTRACT RESEARCH,** DEVELOPMENT, **FABRICATION**

# Specializing in the fields of

- Rocket and Satellite Instrumentation
- Payload Systems
- Solar and Stellar Pointing Systems
- Guidance and Control Systems

WRITE FOR BROCHURE



EDITOR

Martin Summerfield

When 9, 19 mont 1960 lantic

Aft

itary

Proje

Atlas

of the

ment

Divisi

Arma,

propu

in

bea

Am

Spa

ASSOCIATE TECHNICAL EDITOR

Irvin Glassman Barbara Nowak

MANAGING EDITOR ART EDITOR

John Culin

CONTRIBUTOR

George F. McLaughlin

### ASSOCIATE EDITORS

J. George Adashko, Russian Supplement; Ali Bulent Cambel, North western University, Book Reviews; Igor Jurkevich, G. E. Space Scient Laboratory, Russian Articles; Charles J. Mundo Jr., Raytheon Ma facturing Co., Guidance; Bernard H. Palewonsky, Aeronautical Res.
Associates of Princeton, Flight Mechanics; M. H. Smith. Princeton University, Technical Literature Digest

### ASSISTANT EDITORS

Julie Hight, Carol Rubenstein, Estelle Viertel

ADVERTISING AND PROMOTION MANAGER William Chenoweth

ADVERTISING PRODUCTION MANAGER Walter Brunke

### ADVERTISING REPRESENTATIVES

New York

D. C. Emery and Associates 400 Madison Ave., New York, N. Y. Telephone: Plaza 9-7460

Los Ann

James C. Galloway and 6535 Wilshire Blvd., Los Angeles, 0 Telephone: Olive 3

Chicago

Jim Summers and Associates 35 E. Wacker Dr., Chicago, Ill. Telephone: Andover 3-1154

R. F. Pickrell and Vincent Pur 318 Stephenson Bldg., Detroit, M Telephone: Trinity 14

Robert G. Melendy 17 Maugus Ave., Wellesley Hills, Mass. Telephone: Cedar 5-6503

John W. For 239 4th Ave., Pittsburgh Telephone: Atlantic 1-2

### American Rocket Society

500 Fifth Avenue, New York 36, N. Y.

Founded 1930

OFFICERS

President Vice-President Executive Secretary Treasurer General Counsel Director of Publications Howard S. Seil Harold W. Ritch James J. Harin Robert M. Lawre Andrew G. Hi Irwin He

### BOARD OF DIRECTORS

Terms expiring on dates indicated

Ali B. Cambel Richard B. Canright James R. Dempsey Herbert Friedman Robert A. Gross Samuel K. Hoffman A. K. Oppenheim

1961 1962

William H. Pickering
Simon Ramo
William L. Rogers
David G. Simons
John L. Sloop
Martin Summerfield
Wernher von Braun

Maurice J. Zucrow 1960

### TECHNICAL COMMITTEE CHAIRMEN

Ali B. Cambel, Magnetohydrodynamics William H. Dorrance, Hypersonics James S. Farrior, Guidance and Navigation

Herbert Friedman, Physics of the

George Gerard, Structures and Materials Martin Goldsmith, Liquid Rockets

Andrew G. Haley, Space Law and Sociology

Samuel Herrick, Astrodynamics Maxwell W. Hunter, Missiles and Space

David B. Langmuir, Ion and Plasma

Max A. Lowy, Communications Irving Michelson, Education Peter L. Nichols Jr., Propellants and

Eugene Perchonok, Ramjets Richard A. Schmidt, Test Ope and Support

John I. Shafer, Solid Rockets

C. J. Wang, Nuclear Propulsion Stanley C. White, Human Factors Bioastronautics

George F. Wislicenus, Underwater Propulsion John E. Witherspoon, Instrument and Control

Abe M. Zarem, Power Systems

ARS JOURNAL

The co tant po

> namics instrun your re

SPA

P. O. Bo Santa M JULY 1

When crews of SAC's 1st Missile Division successfully launched the USAF ICBM Atlas from Vandenberg Air Force Base, September 9, 1959, the world became aware that the United States had brought into being a formidable retaliatory power for peace. Within four months after the first operational launch, the Air Force doubly underlined this missile's capability. On a single day, January 26, 1960, the 16th and 17th consecutive successful Atlases were fired intercontinental ranges to predetermined targets from both Atlantic and Pacific bases.

After only five years of intensive development, including concurrent research, testing and fabrication under this nation's top military priority, Atlas is extremely versatile as well as powerful. It was the Project Score satellite vehicle and is scheduled for use in Project Mercury, the Man in Space Program, and in other space exploration missions. Thus, used as a booster for space projects, Atlas provides the nation with a key capability in scientific as well as military applications.

Space Technology Laboratories provides the systems engineering and technical direction for the Atlas as well as other portions of the Air Force Ballistic Missile Program. Much of what was learned in building Atlas has helped cut the lead-time in the development of such other Air Force Ballistic Missiles as Thor. Titan and Minuteman.

Among the industrial organizations which have worked in concert in developing Atlas are such major contractors as: Convair, Division of General Dynamics Corp. for airframe, assembly and test; General Electric Co. and Burroughs Corp. for radio guidance; Arma, Division of American Bosch and Arma Corp. for inertial guidance; Rocketdyne Division of North American Aviation, Inc., for propulsion; General Electric Co. for re-entry vehicle; Acoustica Associates for propellant utilization.

America's first intercontinental ballistic missile...is helping to bear the burden of today's power for peace

JULY 1960



The continuing development of Atlas as well as other USAF missiles and related space probes, has created important positions on STL's technical staff for scientists and engineers with outstanding capabilities in: thermodynamics, aerodynamics, electronics, propulsion systems, structures, physics, computer technology, telemetry, and instrumentation. If you believe you can contribute in these or related fields and disciplines, you are invited to send your resume to:

## SPACE TECHNOLOGY LABORATORIES, INC

P. O. Box 95004, Los Angeles 45, California, Attention: Richard A. Holliday Los Angeles · San Diego Santa Maria · Sacramento · Denver · Cheyenne · Cape Canaveral · Washington, D.C. · Manchester, England · Singapore · Hawaii 595

# **ARS Expands Its Publication Program**

IT HAS BEEN well known for some time, by ARS members and by contributors to the ARS JOURNAL, that the flow of manuscripts and preprints to the JOURNAL has been running far above the capacity of the JOURNAL to publish them. This problem has been a matter of concern to the Society's publication staff and its Board of Directors for at least a year.

The Board has always regarded the publication of technical papers as one of the most fundamental duties of our Society, and it has always voted generous budgets for the Journal, in comparison with other engineering societies of comparable size. The Journal budget programmed for this year is larger than that of last year, and new plans have been approved for tapping additional sources of revenue to permit even greater expansion of the Journal next year.

Despite this expansion program for the ARS JOURNAL, which will always be limited by the revenues available to the Society, a statistical forecast indicates that there will still be an excess of qualified papers above the publishing capacity of the JOURNAL. To solve this problem, a new publishing vehicle is needed that can pay its own way and expand or contract according to the flow of papers. In particular, a severe load is expected as a result of the increasing number of specialized symposia in various fields that are being scheduled by the Technical Committees of the Society for 1960, 1961 and future years.

A solution has been found. The ARS has signed a long-term contract with Academic Press, Inc., for the publication and distribution of a series of books that will function as a supplement to, and an extension of, the ARS JOURNAL. The first book in the series will comprise a

selection of the papers of the Solid Propellant Rocket Research Symposium, and will be placed on the market about Sept. 15, 1960.

Some of the features of this new program are the following:

- 1 Each book will be cloth-bound, hard-covered, good looking, about  $6\frac{1}{2} \times 9\frac{1}{2}$  in. in outer dimensions. Each book will be a dignified addition to the owner's library.
- 2 The title of the series will be: "Progress in Astronautics and Rocketry." The subtitle will be: "A Publication of the American Rocket Society." The first volume will be titled: "Volume 1: Solid Propellant Rocket Research," and underneath this line will be printed: "Based on a Symposium held at Princeton University, January 28-29, 1960. Each book will be edited by a specialist (or specialists) in the field, and his name (or names) will be featured as editor (or (editors).
- 3 The price will be down around \$5.00 for a book about 500 pp. in length, which will help to achieve the widest possible distribution. Similar low prices will be established for future volumes. For the Society, this will be a nonprofit venture. Our aim is to serve the technical community.
- 4 The Series will not be restricted in concept simply to the proceedings of ARS specialized symposia. Not all symposia held by the ARS will be published in this form. The contents will be selective; that is, the Series will be governed by criteria of acceptance similar to those of the ARS JOURNAL, although subjects of a nonarchive character may be covered by individual books

each matter slapp expeorde

phist

effects sale Librasubse main just vigor of brested and a

meet book this Liqui collec while suppl ate p not t duly.

book prompstand proce

# Contract Signed with Academic Press for ARS Progress Series

from time to time. A very important rule is that each volume will be coherent in itself as to subject matter. Heterogeneous collections will not be slapped together. The purchaser will not be expected to buy a lot of unrelated material in order to get the papers he wants.

- 5 Promotion of sales will be vigorous, sophisticated, at frequent intervals, and, we believe, effective. Our aim is to achieve a 3000 to 5000 sale of each volume of the series, as a minimum. Libraries will be encouraged to place standing subscription orders for the entire series, and to maintain complete sets right from Volume 1, just as they do for periodicals. Low price and vigorous selling are important for the achievement of broad distribution of the papers to the interested scientific community, both in the U. S. and abroad.
- 6 The projected time lag from the date of a meeting to the date of distribution of the printed book will be about three months. We expect this to apply to the July ARS Symposium on Liquid Rockets and Propellants, and to all future collections and symposia. Release will occur while the subject is still "hot." Reprints can be supplied to the author without delay, at a moderate price. (The number will be limited in order not to undermine the market for the book unduly.)

These features of the Series, that is, dignified book style, sequential publishing, low price, prompt release, availability of reprints, critical standards of acceptance, adaptability to nonproceedings collections, coherent contents, and vigorous, repetitive selling, all combine to make this Series attractively different from the runof-the-mill ineffective proceedings publications that are sold from time to time by various groups. This project has been approved with enthusiasm by the Technical Committee Chairmen of the ARS.

As a result, about five volumes are planned for 1960, and still more for 1961, in different fields, of course.

To achieve the low price and prompt publication, letterpress printing will have to be avoided. Instead, offset printing will be employed, with plates photocopied from the authors' typed sheets. For this purpose, all authors will be asked to prepare their manuscripts according to special typing instructions on photocopy sheets that will be supplied by ARS. Although this may seem to be an additional burden on the author, we feel it is a small price for him to pay for the advantage of prompt publication of his paper in a dignified, widely advertised book.

If this plan is successful, we can expect to see several results flowing from it. One will be a reduction in the ARS JOURNAL backlog, a reduction in publication delay, and as a consequence, an increase in offerings of worthy manuscripts to the Society.

A second result will be greater readiness on the part of our Technical Committees to hold specialized symposia, since they were often deterred in the past by the insoluble problem of getting the papers of such symposia published. Finally, with considerable optimism, we expect that this program will prove so successful that other technical societies will adopt similar plans to solve their publication backlogs.

Martin Summerfield Editor, ARS JOURNAL Editor, ARS Progress Series

# **Radio Astronomy Observations From Space**

FRED T. HADDOCK1

T for he ma

sto tvi

ver

ma

a l (be typ

low

rela

imu

bele

whi

sph

requ tion obse

mak

for t

sun. the

dista

dece

its fl

T

the l

the h

the i

secor

will l

corre

cosm

highe

event

radio

ionos  $\times 10$ 

mum

F-lay

perige

have :

cessio for me

Fig.

at Ea

tensiti

turbed

siopeia

backgr

greater gain an

log-per

directe

axes, w thereby

Howev

stand t

ment a

JULY 1

It ca

Th

It

University of Michigan Ann Arbor, Mich.

A description is given of four radio astronomy experiments that can be carried out with simple very low gain antennas at frequencies which are too low to penetrate, free of distortion, Earth's ionosphere. These are: 1 Measurement of the integrated radio flux from the galaxy at frequencies below 10 mc; 2 measurement of the dynamic spectra of solar bursts of frequencies below 30 mc; 3 measurement of the dynamic spectra of bursts at frequencies below 30 mc from the planet Jupiter; 4 measurement of the distribution of electron densities outward from the F-layer of Earth's ionosphere. These experiments can best be conducted aboard a highly eccentric artificial Earth satellite with an apogee greater than 5 to 10 Earth radii.

URING the past decade or so extensive radio astronomy observations have been conducted at many frequencies ranging principally from 10 to 10,000 mc (a frequency of 10 mc corresponds to a vacuum wave length of 30 m). Earth's lower atmosphere strongly absorbs and emits radio waves above a frequency of 10,000 mc, thereby limiting higher frequency observations. But since this observational limitation can be largely overcome by flying the receiving equipment in balloons or high altitude aircraft, satellite experiments at these frequencies are not yet urgent. At frequencies from about 10 to 10,000 mc, the vertical atmosphere is normally highly transparent. However, the ionosphere and troposphere, by distorting the phase fronts of incoming waves, limit the measurement of size and position of radio sources and the radio emission detail that can be seen on the sun and planets. Satellite observations would also overcome this limitation in resolution, but would require very large antennas or interferometers; one would need an antenna system extending over 10 km to resolve 1 min of arc at 100 mc.

On the other hand, satellite observations at frequencies below about 30 mc, even with low gain antennas, would be extremely valuable. It would be possible to extend the dynamic radio spectra of solar bursts and bursts from Jupiter down to 5 mc or lower and to check and extend the work of Reber and Ellis (1)2 who extended the spectrum of the general cosmic radio background emission to 1 mc by observing through occasional "holes" in the ionosphere. It would also be possible to determine the free-electron density distribution in Earth's atmosphere above the F-layer of the ionosphere and determine how this distribution blends into that of interplanetary space or the solar corona. These are important and basic experiments which hold promise of greatly increasing our knowledge of solar flares, solar corpuscular streams, the sun's outer atmosphere, the atmosphere of Jupiter, the interstellar medium, the galactic corona and the origin of cosmic rays, as well as of providing valuable design data for future satellite experiments relating to ambient radio noise levels (both steady-state and transient), the characteristics of the radio transmission through the solar system, and the leakage of natural static and manmade signals up through the ionosphere.

When more elaborate and highly directional satellite antennas are developed, it will be possible to extend the radio spectrum of the brighter radio sources. The determination of the spectra of radio sources at low frequencies is required to specify the physical parameters in the radiation process in the variety of interesting radio sources, such as the colliding galaxies in the constellation of Cygnus, the peculiar nebulosity in Cassiopeia, the supernova remnant in Taurus, the galactic center source, etc. In short, satellite observations make it possible to extend the radio astronomy spectrum downward by several octaves, to a limit determined only by the free electron in the interplanetary medium or solar corona.

The following radio astronomy satellite experiments can be made with simple long wire, short stub, or loop antennas with conventional radio receivers and will now be discussed individually:

- Dynamic spectra of solar radio bursts.
- Dynamic spectra of radio bursts from Jupiter.
- The spectrum of cosmic radio background radiation.
- The distribution of electron densities outward from the F-layer.

### Dynamic Spectra of Solar Radio Bursts

A description of solar activity and flares, how they are related to events on the sun and Earth, and their scientific and practical importance appears in many texts (2). Certain of the greater solar flares are accompanied by large bursts of radio emission which begin at the higher frequencies (above about 200 mc) and appear progressively later at the lower frequencies. The observed rates of this downward drift in frequency fall into two broad but distinct classes, as first noted by Wild and McCready (3) in 1949 from their sweep-frequency measurements of solar radio bursts. They denoted the fast drift rate bursts [of the order of 20 (mc/s) sec-1] as type III and the slower drift rate bursts [of the order of 0.25 (mc/s) sec<sup>-1</sup>] as type II bursts. They denoted as type I the narrow spectrum (a few mc wide), short duration (less than 1 to 20 sec) impulsive "noise storm" bursts. Wild (4) has interpreted the type III and II bursts as caused by corpuscular streams shot out from the region of a solar flare, at velocities of the order of 50,000 km per sec for type III and 1000 km per sec for type II. The streams excite plasma oscillations of decreasing frequency as they pass through successively more rarefied layers of the corona.

Presented at the ARS Semi-Annual Meeting, June 8-11, 1959, San Diego, Calif.

Professor of Astronomy and of Electrical Engineering.

Numbers in parentheses indicate References at end of paper.

The approximate heights of different plasma levels are known for optical eclipse determinations of coronal electron densities; hence the outward radial component of velocity can be estimated from the frequency drift. Wild further noted that the velocities of particles presumed to cause great geomagnetic storms following great flares are of the same order as the type II burst velocities, and that the time of flight velocities computed for the rare solar cosmic ray increases following very great flares correspond to the type III burst velocities.

Not all radio bursts of type II or III give rise to a magnetic storm or a cosmic ray increase. There is some evidence that a number of type II and type III events start at a high frequency, reach only a certain limiting frequency (because of a lack of kinetic energy in the stream?) and are turned back or stopped. It has been tentatively noted that type II and type III bursts which appear to terminate at a low frequency are not associated with geomagnetic index increases (5). In general, the type II bursts do show some correlation with the geomagnetic increases. Therefore it is important to make observations of solar spectra in a band below about 20 mc. This is difficult, even at those frequencies which normally penetrate the ionosphere, because the ionosphere is disturbed at the very time these observations are required. The satellite data can be correlated with observations from the ground to help identify the particular event observed and also to help identify bursts from the planet Jupiter and terrestrial interference.

The importance of this experiment is twofold: It would make possible the further checking of the stated hypothesis for the cause of the great bursts of radio emission from the sun, and it would also make possible, under this hypothesis, the determination of the decrease of electron density with distance from the sun, and perhaps the acceleration or deceleration of the corpuscular stream in the initial phase of

its flight from the sun to Earth.

The observation could consist, for example, of measuring the burst intensity as a function of frequency and time over the band of 5 to 30 mc with a receiver band pass of 0.2 mc while the receiver is tuned over the band one or more times a second.

It is expected that some type III and type II burst spectra will be recorded over the entire 5- to 30-mc band and would correlate with geomagnetic storms, aurorae and perhaps solar cosmic ray increases. Some will be detected only at the higher frequencies and may not be correlated with terrestrial events.

The orbit perigee should be sufficiently high to eliminate radio propagation disturbances of the solar signal by Earth's ionosphere. The critical electron density for 5 mc is 3.1  $\times$   $10^{5}~\rm cm^{-3}$ . This is about 10 times smaller than the maximum over England at noon during November 1957. The F-layer is likely to interfere with observations unless the perigee is above about 1200 km. A desirable orbit would have a polar inclination which would result in an orbit precession that would keep the sun under continuous surveillance for months.

Fig. 1 displays the variation with frequency of flux density at Earth (in MKS units) for average peak solar burst intensities (5,6). The flux density from the quiet or undisturbed sun, from the strongest cosmic radio source (Cassiopeia-A), and from the integrated intensity of the cosmic background radiation (labeled G=1) is also shown (1).

It can be seen that the average burst level is about 10 times greater than the cosmic background noise level when a low gain antenna is used. A long wire Vee antenna, perhaps of log-periodic structure, having its beam fixed in space and directed toward the sun from a satellite stabilized about three axes, would give a large increase in signal to noise ratio, and thereby make is possible to detect weaker solar radio bursts. However, such an antenna must be sufficiently stiff to withstand the tidal force of Earth in order to prevent its alignment along the Earth-satellite radius vector, unless the

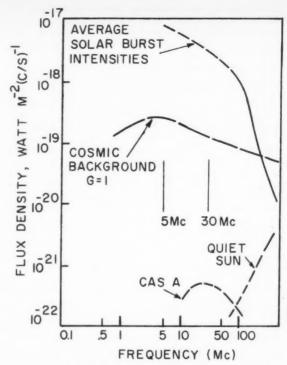


Fig. 1 Radio flux density spectrum of average solar burst intensities extrapolated downward from about 30 mc, the galactic background flux density measured on a spinning dipole pattern and the spectra of the strongest radio source Cas A and the quiet

satellite is in a planetary orbit around the sun. The maximum acceleration due to the tidal force near Earth is about  $5\times 10^{-8}\,l$  of surface gravity, where l is the distance (in meters) from the satellite center of gravity.

It would be important to have a number of related experiments operating concurrently in the same satellite and on the ground. For example, experiments for measuring UV, x-rays, cosmic rays, geomagnetic stream particles, Lyman- $\alpha$  spectroheliograms, geomagnetic perturbations, etc., could be in the same vehicle, or in other satellites, while the standard IGY experiments are conducted more intensively on the ground.

### Dynamic Spectra of Radio Bursts From Jupiter

In 1955, Burke and Franklin (7) unexpectedly discovered emission of intense bursts from the planet Jupiter at 22 mc. Since then a number of very interesting and important facts have emerged (8). It has been known for several years that about 20 per cent of the time the planet Jupiter emits very intense bursts of radio emission in the frequency band of 14 to 27 mc. Each individual burst has a rather narrow bandwidth of the order of 1 mc. They occur independently at different frequencies and last for 0.1 to 15 sec. The bursts are most numerous at about 18 mc; observations below 18 mc are rare, perhaps because of interfering signals and disturbance or blocking by Earth's ionosphere. The detection of bursts at frequencies above 30 mc has not been confirmed. Therefore the spectra of the radio bursts from Jupiter have an extremely sharp high frequency cutoff. Nothing definite is known about the low frequency cutoff; however,

if a Jovian ionosphere controls the duration of burst activity, then low frequency cutoffs from 8.5 to 20 mc are indicated. On the other hand, this concept has been criticized by Carr et al. (8). Gallet has suggested that corpuscular streams are ejected from the "surface" of Jupiter through a Jovian ionosphere, creating plasma oscillations and radio bursts (8).

A fact bearing on the importance of the radio bursts from Jupiter is that the radio energy of a single large burst is about 1012 watt-sec or of the order of the energy expended in an average volcano. The overall significance of radio bursts from Jupiter can be appreciated when it is noted that the radio observations to date strongly suggest the existence of an ionosphere on Jupiter, a magnetic field with a strength of at least 5 gauss, or 10 times that of Earth, and that the energy sources for the radio bursts are fixed to the surface of a solid rotating body. Recently it has been shown by Carr et al. (8) that the period of rotation of this body is 11.8 sec shorter than the period observed in the nonequatorial atmosphere of Jupiter. The determination of the energy source of bursts from Jupiter may bear on the composition and physical state of the invisible solid body of Jupiter, and detailed dynamic spectra studies may disclose information on the outer atmosphere, ionosphere and magnetic field of this planet.

The observation of Jupiter could employ the same receiver and antenna as proposed for the solar burst experiment. It is expected that numerous bursts will be found over the band of 18 to 30 mc. However, knowledge of the range and requency of occurrence of bursts below 18 mc will provide new and valuable data for testing hypotheses of the emission process and influence of a Jovian ionosphere on the bursts. Correlation of this range and frequency with solar induced effects in Earth's ionosphere can also be studied. It will be especially interesting to observe Jupiter during a sudden

disturbance of Earth's ionosphere.

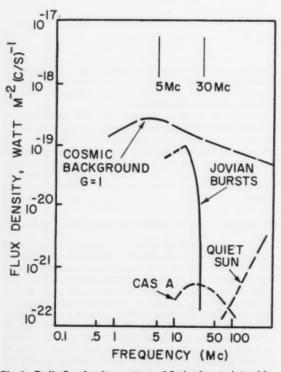


Fig. 2 Radio flux density spectrum of Jovian bursts, intensities extrapolated downward from about 50 mc, the galactic background flux density measured on a spinning dipole pattern and the spectra of the strongest radio source Cas A and the quiet sun

Fig. 2 is the same as Fig. 1 except that the solar burst spectrum has been replaced by the Jovian burst spectrum. Note that the intensity of Jovian bursts is somewhat less than that for solar bursts. Increased antenna gain would be desirable, but the orientation of a directive antenna toward Jupiter adds complexity.

### Spectrum of Cosmic Radio Background Radiation

The determination of the low frequency radio frequency spectrum of the cosmic background radiation at low and high galactic latitudes is required to separate the components of radio emission (both galactic and extragalactic), and thermal and nonthermal emission. The thermal and nonthermal emission processes that contribute to the cosmic background spectrum should produce a maximum brightness temperature at a frequency in the band of 1 to 20 mc; the spectrum then rapidly decreases at lower frequencies (9). Because of the intervention of Earth's ionosphere, it is not possible to make reliable observations from the ground bearing on this critical point; observations made from a satellite would make possible direct observation without absorption and reflection by Earth's ionosphere. The principal value of the experiment is the determination of the important parameters involved in the process of cosmic background emis-The source of the cosmic background radiation is important from the point of view of cosmolgy, galactic structure, the origin of radio sources and cosmic rays.

The only information available on the cosmic background intensity below 9 mc is from observations made by Reber and Ellis (1) in Tasmania at times when the ionosphere was transparent (at times of low solar activity and at night). were able to obtain estimates of the brightness of the cosmic background in the range of from 1 to 10 mc. However, the accuracy of their measurements depends upon estimating the size of the transparent hole in the ionosphere. it is proposed that experiments with eight single-frequency receivers operating on separate or the same antenna be performed. The frequencies should cover uniformly the range of about 65 kc to about 6 mc. This would make possible the determination of electron densities over a wide range of values and also make possible a great stride forward toward extending information on electron densities in the solar corona at large distances from the sun or in the interplanetary medium. The observation would consist of the continuous recording of the intensity on each channel. It would be desirable to scan the antenna beam over a great circle perpendicular to the galactic plane, and to continue the observations to note changes at the time of solar events and to record

bursts from the sun and Jupiter.

We would expect of find that the intensity of the cosmic background emission peaks at higher frequencies in the galactic plane than at the poles because of absorption by interstellar electrons which are concentrated in the galactic plane. The peak intensity of emission will occur near 0.5 mc in the plane, depending on the antenna directivity; whereas at the galactic pole the peak of emission may occur between 0.02

It appears likely that interplanetary electrons will prevent an unobstructed view of the galaxy at the lowest frequencies, even with the orbit at heights of a few Earth radii. If a density of 600 cm<sup>-3</sup> exists around the Earth-moon system, then the galaxy is blocked from view below about 0.22 mc. An orbit inclination perpendicular to the plane of the Milky Way is desirable only for a directive beam measurement. Some directivity is obtained by Earth occulting part of the galactic background. A low directivity measurement of the radio background intensity can be accomplished with a small loop or stub antenna, since antenna radiation efficiency is not too important because of the high background noise level.

A directive beam measurement of background radiation

at the low figure of the suffit of the suffi

can

way

in t

mor

two

the

eacl

WOU

Fo densi vent all fr of 600 the g kc.
Th tant It be

atmo

field

origin

from

of zoo The estimation of trans howe ionoz as a satell region

tron rocke ered should uring which probe Thi

from to 10 me of the rather short altitude

JULY

can be made by using a very long wire antenna (at least 10 wave lengths in each half) released from a satellite stabilized in three axes, orientated and locked onto Earth, in an orbit more or less perpendicular to the plane of the Milky Way-the two halves of the antenna being aligned by tidal forces with the Earth-satellite vector, one toward Earth and one away, each 45-km long (90 lb of AWG No. 30). This antenna would have a directive gain of 9 at 65 kc and somewhat higher at the higher frequencies. It is possible to obtain a sufficiently low ohmic-to-radiation-resistance ratio if a receiver noise figure is less than 3 db. The natural "pendulum" frequency of this long wire antenna is independent of length and is sufficient to keep the wire aligned with Earth and the satellite. A two-wire, balanced-fed antenna is required because the electrical capacity of the satellite is too low at act as a ground plane for efficient operation.

Fig. 3 displays the spectrum of cosmic radio background intensity, in temperature units, as extrapolated from higher frequency measurements (10) and as measured at a number of frequencies from 1 to 4 mc by Reber and Ellis (1). The shaded area represents speculation of a decrease in intensity at low frequencies. The decrease can be intrinsic to the emission process or, more likely, to absorption or reflection by the electrons in the sun's outer corona, by interplanetary electrons, or an extension of Earth's ionosphere.

It is expected that a sudden drop will be found in the background brightness around 0.14 to 0.3 mc.

# Distribution of Electron Densities Outward From the F-Layer

For the radio astronomer, knowledge of the electron density surrounding Earth is important, since electrons prevent cosmic radio waves from reaching an Earth satellite at all frequencies below a certain critical value. If an estimate of 600 electrons per cm³ is correct, it is not possible to observe the galaxy, or even the planets, with frequencies below 220 kc.

The electron density distribution around Earth is important for a number of geophysical and astrophysical problems. It bears directly on studies of Earth's ionosphere and upper atmosphere. It is important for studies of Earth's magnetic field and the interplanetary magnetic field, for the nature, origin, and heating of the sun's corona, the conduction of heat from the sun to the interplanetary medium, and the nature of zodiacal light.

The electron density distribution above the F-layer can be estimated from ionospheric theory, from the Faraday rotation of radio waves from moon radar echoes and from radio transmissions by rockets or satellites. These determinations, however, involve, or are affected by, the dense regions of ionozation in the F-layer, and therefore are not as attractive as a direct determination of the density surrounding a satellite as it travels from the dense to the distant tenuous regions.

A Langmuir probe method for the determination of electron temperature and density has been demonstrated on rockets in the E-layer of the ionosphere and has been considered for Earth-satellite measurments (11). This method should be compared with the following suggestion for measuring ambient electron densities; this is an r-f probe technique which may have certain advantages over the d-c Langmuir probe.

This experiment consists of tuning a radio frequency oscillator, attached to a matched long wire antenna extending from the satellite, over a frequency band from 20 kc to about 10 mc at a rate determined by the rate of change of altitude of the satellite. For a circular orbit this sweep rate could be rather slow; for an eccentric orbit the sweep period should be short compared to the time it takes a satellite to change its altitude. As the oscillator is swept over the frequency range,

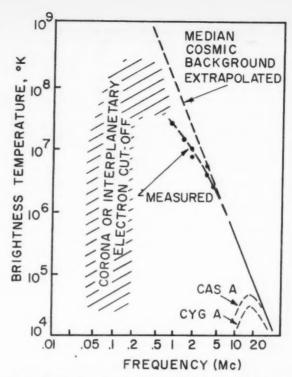


Fig. 3 The integrated cosmic ray background spectrum extrapolated below 10 mc with a few points measured by Reber and Ellis. Shaded area indicates probable spectrum at lower frequencies

the change in the impedance of the oscillator circuit is recorded. When the oscillator frequency approaches the critical frequency of the ambient electrons, there would be a change in the record. With magnetic fields at oblique angles with respect to the antenna, analysis would be needed to interpret the results. It may be possible that changes in aspect of the antenna with Earth's field will give additional information about the field. The rate at which information must be telemetered to Earth for this experiment depends largely on the orbit. The only data needed would be measurements of the change in the impedance with position of the satellite, and perhaps the antenna orientation. It may also be useful to record the phase of impedance as well as its magnitude. It would be extremely important to determine the change in magnitude and distribution of the electron density, following a flare or radio burst and during a geomagnetic storm or aurora.

It is expected that the electron density will be found to decrease from the F-layer maximum near 10<sup>6</sup> cm<sup>-3</sup> (depending on local time, season, solar activity and latitude) to several thousand cm<sup>-3</sup> at an altitude of 1000 to 4000 km, and then gradually to decrease to a few tens or hundreds at several Earth radii. The perigee should be about 250 to 300 km and the apogee several Earth radii. A polar orbit is preferred in order to determine the effect of the geomagnetic field on the electron distribution.

Fig. 4 illustrates schematically some possible distributions for the electron density about the F-layer. The right-hand ordinates are the critical plasma frequencies for the corresponding electron densities on the left-hand ordinates. The dashed line on the left represents the decrease above the F-layer maximum. Its slope is based on an article

on Sputnik I and II (12) and a recent Russian paper (13). The solid curve is based on a model by Dungey (14) which represents the electron density decrease with the distance R from Earth's center by 600 exp  $(2.5 R_e/R)$  cm<sup>-3</sup> where  $R_e$  is the radius of Earth. The two levels on the right-hand side of Fig. 4 labeled H represent the range of values given by van de Hulst (15) from a study of the polarization of zodiacal light. Six hundred cm<sup>-3</sup> is the asymptotic value by Dungey's model and was adjusted to this in order to fit both the zodiacal light determination and the results obtained from magneto-ionic-duct propagation studies ("whistler")(16). Later studies of "whistlers" indicated an electron density of 300 cm<sup>-3</sup> at a distance of 3 Earth radii (16).

Two recent models of the electron distribution of the terrestrial "corona" also based in part on very low frequency emission data are shown, one by Gallet (17) and one by Johnson (18).

The divergency of these curves reflects our lack of knowledge which should soon be reduced by satellite experiments.

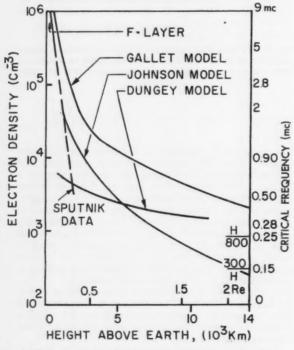


Fig. 4 Various models of the electron density distribution above

### References

1 Reber, G. and Ellis, G. R., "Cosmic Radio-Frequency Radiation Near One Megacycle," J. Geophys. Res., vol. 61, March 1956, pp. 1-10; Ellis, G. R., "On the Propagation of Radio Waves Through the Upper Atmosphere," J. Atmos. Terr. Phys., vol. 9, July 1956, pp. 51-55; Ellis, G. R., "Cosmic Radio-Noise Intensities Below 10 Mc/s," J. Geophys. Res., vol. 62, June 1957, pp. 229-234; Reber, G., "Long-Wave Radiation of Possible Celestial Origin," Symposium on Radio Astronomy (C.S.I.R.O. Radiophysics Lab., Sydney, 1957), p. 53; Ellis, G. R., "Low-Frequency Cosmic Radio Noise Spectra," ibid. p. 54; Reber, G., "Between the Atmospherics," J. Geophys. Res., vol. 63, March 1958, pp. 109-123.
2 Sec, for example, Kuiper, G. P., Ed., "The Sun," University of Chicago Press, Chicago, 1953, pp. 322-531.
3 Wild, J. P. and McCready, I. L., "Observations of the Spectrum of High-Intensity Solar Radiation at Metre Wavelengths. I. The Apparatus and Spectral Types of Solar Bursts Observed," Australian J. Sci. Res., vol. A3, Sept. 1950, pp. 387-398; Wild, J. P., et al., "Observational Radio Astronomy," in "Advances in Electronics and Electron Physics," Martin, L., Ed., Academic Press, N. Y., vol. 7, 1955, pp. 299-362.
4 Wild, J. P., "Radio Observations of Solar Flares," in "Joint Discussion on Solar Flares," Trans. of Internat. Astron. Union, Ninth General Assembly

L., Ed., Academic Press, N. Y., vol. 7, 1955, pp. 299-302.
4 Wild, J. P., "Radio Observations of Solar Flares," in "Joint Discussion on Solar Flares," Trans. of Internat. Astron. Union, Ninth General Assembly held in Dublin, Aug. 29 to Sept. 1955, Cambridge University Press, vol. 9, 1957, pp. 661-663; Wild, J. P. and Zirin, H., "On the Association of Solar Radio Emission and Solar Prominences," Australian J. Phys., vol. 9, Sept. 1956, pp. 315-323.

Davies, R. D., "An Analysis of Bursts of Solar Radio Emission and Association with Solar and Terrestrial Phenomena," Monthly Notices,

Roy. Astron. Soc., vol. 114, 1954, pp. 74-92.
7. Burke, B. F. and Franklin, K. L., "Observations of a Variable Radio Source Associated With the Planet Jupiter," J. Geophys. Res., vol. 60, June

Source Associated with the Planet Jupiter, J. Geophys. Res., vol. 60, Julie 1955, pp. 213-217.

S. Shain, C. A., "Location on Jupiter of a Source of Radio Noise," Nature, vol. 176, no. 4487, Oct. 29, 1955, pp. 836-837; Shain, C. A., "18.3 Mc/s Radiation from Jupiter," Australian J. Phys., vol. 9, March 1956, pp. 61-73; Gardner, F. F., "Radio Noise from Jupiter," Symposium on Radio Astronomy (C.S.I.R.O. Radiophysics Lab, Sydney, 1956), p. 38; Annual Research of D. Directorial Margaetic Margaetics D. (1998). Radio Astronomy (C.S.I.R.C). Radiophysics Lab, Sydney, 1990), p. 38; Annual Report of the Director of Dept. Terrestrial Magnetism, Washington, D. C., 1956, p. 72; Gallet, R. M., "The Results of the Observation of Jupiter's Radio Emissions on 18 and 20 Mc in 1956 and 1957, "Abstracts of IRE-URSI Spring Meeting 1957, IRE Trans. on Antennas and Propagation, vol. AP-5, no. 3, July 1957, pp. 327-328; Carr, T. D., Smith, A. G., Pepple, R. and Barrow, C. H., "18-Megacycle Observations of Jupiter in 1957," Astrophys. vol. 127, March 1958, pp. 274-283; Franklin, K. L. and Burke, B. F. adio Observations of the Planet Jupiter," J. Geophys. Res., vol. 63, no. 4 "Radio Obse pp. 807-824.

pp. 807–824.

9 Piddington, J. H., "The Origin of Galactic Radio-Frequency Radiation," Monthly Notices, Roy. Astron. Soc., vol. 111, no. 1, 1951, pp. 45–63; Greenstein, Jesse L. and Minkowski, Rudolph, "The Crab Nebula as a Radio Source," Astrophys. J., vol. 118, July 1953, pp. 1–15; Brown, R., Hanbury, and Hazard, C., "A Model of the Radio-Frequency Radiation from the Galaxy," Phil. Mag., vol. 44, Sept. 1953, pp. 339–963; Twiss, R. Q., "On the Nature of the Discrete Radio Sources," Phil. Mag., vol. 45, March 1954, pp. 249–258; Roman, N. G. and Haddock, F. T., "A Model for Nonthermal Radio-Source Spectra," Astrophys. J., vol. 124, July 1956, pp. 35–42; Lamden, R. J. and Lovell, A. C. B., "The Low-Frequency Spectrum of the Cygnus (19N4A) and Cassiopeia (23N5A) Radio Sources," Phil. Mag., Ser. 9, vol. 1, Aug. 1956, pp. 725–737.

1956, pp. 725-737.

10 Herbstreit, J. W. and Johler, J. R., "Frequency Variation of the Intensity of Cosmic Radio Noise," Nature, vol. 161, 1948, pp. 515-516.

11 Hok, G., Sicinski, H. S. and Spencer, N. W., "The Temperature and Electron Density Measurements in the Ionosphere by a Langmuir Probe," in "Scientific Uses of Earth Satellites," Van Allen, J. A., Ed., Univ. of Mich. Press, Ann Arbor, 1956, pp. 263-267.

12 "Research Based on Sputniks I and II Reported by Soviets" (author Care), Science vel. 127, pp. 2911, Lyne 12, 1958, pp. 1278-1281.

anon.), Science, vol. 127, no. 3311, June 13, 1958, pp. 1378-1381.

13 Alpert, Y. L., "State of the Outer Ionosphere," Privoda, vol. 6, 1958, pp. 85-87, translation by E. R. Hope, Def. Res. Board, Canada, no. 1958, pp. 89-97, transmisser.
 T304R, Sept. 1958.
 Dungey, J. W., "Electrodynamics of the Outer Atmosphere
 Dungey, J. W., "Electrodynamics of the Outer Atmosphere

14 Dungey, J. W., "Electrodynamics of the Outer Atmosphere," in "The Physics of the Ionosphere," The Physical Society, London, 1955, pp.

229–236.

15 van de Hulst, H. C., "On the Polarization of the Zodiacal Light,"

Memoires Soc. Roy. Sci. on "The Solid Particles Between the Stars," Liege,
Scr. 4, vol. 15, 1955, p. 89.

16 Blackwell, D. E., "The Transition from the Ionosphere to Interplanetary Space," Nature, vol. 181, no. 4618, 1958, pp. 1237–1238.

17 Gallet, R. M., "The Very Low-Frequency Emissions Generated in
the Earth's Exosphere," Proc. IRE, vol. 47, no. 2, pp. 211–231.

18 Johnson, F. S., "The Structure of the Outer Atmosphere Including
the Ion Distribution Above the F-2 Layer," Tech. Rep., IMSD-49719.
Lockheed Missiles and Space Division, April 28, 1959. (A revised version
has since appeared in J. Geophys. Res., vol. 65, Feb. 1960, pp. 577–584.)

602

ARS JOURNAL

hiele. possi is in liquio may impo Ther contr Suj of va fore. such lem a tions strict hand mean Th for m conce tanks theor type a rat vious which

> simili of lim suppi Th requi by ap between for tv

1 T course ORD 2 D 4 N JULY

# Simulation of Fuel Sloshing **Characteristics in Missile Tanks** by Use of Small Models'

H. NORMAN ABRAMSON<sup>2</sup> GUIDO E. RANSLEBEN Jr.3

Southwest Research Institute San Antonio, Texas

Similitude theory is applied to the problem of fuel sloshing in accelerated tanks to establish criteria for the design of model experiments. It is found that dynamic modeling is possible even if liquid viscosity is considered, and the ranges of significant parameters and the selection of model liquids are discussed. The results of experiments made with small models are compared with those obtained with full-scale tanks, for two different types of damping devices.

S LOSHING motions of fuel in partially filled tanks may be established by essentially lateral accelerations of the ve-Such fuel motions are of importance, for there is the possibility of extreme oscillations if the excitation frequency is in the neighborhood of one of the natural frequencies of the liquid fuel. The forces exerted by the fuel on the tank walls may then lead to perturbations in the flight trajectory, or may impose severely high stresses on structural components. There is further the ever-present danger of resonance at the control system frequencies.

Suppression of sloshing modes has been attempted by means of various mechanical devices and baffle systems, and, therefore, it is of some importance to evaluate the effectiveness of such devices. Purely mathematical approaches to this problem are exceedingly difficult because of the boundary conditions introduced by such suppression devices, and are restricted, therefore, essentially to simple cases. On the other hand, it may be possible to evaluate suppression devices by means of suitably designed and conducted model tests.

The problem considered here is the specification of criteria for model tests which will give useful quantitative information concerning sloshing and slosh suppressors in full-scale fuel tanks. This is accomplished by the application of similitude theory to obtain appropriate expressions for the model-prototype relationships. These may be employed in turn to yield a rational design of model tests. This is in contrast to previous experimental studies of the fuel sloshing problem (1-4),4 which have apparently been conducted without regard to similitude requirements, and consequently are believed to be of limited usefulness for evaluation of the effectiveness of slosh suppression devices.

The purposes of the present paper are to discuss the basic requirements for model studies of fuel sloshing in rigid tanks by application of similitude theory, and to show correlation between tests made on small models and on full-scale tanks, for two different suppression devices.

### Similitude Relations for Fuel Sloshing

The vehicle is considered to be in vertical flight with constant acceleration directed along the flight path, and sloshing is assumed to be excited by time-dependent accelerations acting essentially normal to the flight path. For purposes of the present study, the exciting accelerations will be considered either as purely translational or purely rotational about an axis normal to the flight path.

The essential features of the sloshing motion are further governed by the physical properties of the liquid and the pressurizing gas. The importance of the liquid density and total mass is obvious; however, viscosity and surface tension require additional comment. If suppression devices are incorporated, it is clear that their effectiveness must, to a very substantial degree, depend upon the damping forces they can provide as the result of viscous action of the liquid. If models of very small size are employed, it is conceivable that the effects of sloshing may be substantially modified by surface tension forces acting on the suppression devices and at the tank walls. As will be discussed later, it does not seem possible to provide rigorous modeling if surface tension forces are included, and, further, it is believed that the total contribution of such forces would be small compared to the inertial and viscous forces. Consequently, surface tension forces will be omitted in the analysis. Similarly, it is supposed that the forces produced by the pressurizing gas are negligible compared with the other forces, and therefore will be omitted. The gas pressure may be accounted for implicitly, however, because it is included in the total pressure at the tank wall by direct superposition, since the gas volume remains essentially constant during sloshing.

Further restrictions to the analysis are provided by the assumptions of small excitations, rigid tank and the existence of geometrical similarity in all respects between model and prototype. The model and prototype suppression devices themselves are considered geometrically similar in all respects, and the corresponding inertial and apparent mass forces associated with them are neglected in comparison with the viscous forces.

Received April 17, 1999.

The results presented in this paper were obtained during the course of research conducted under Contract no. DA-23-072-ORD-1251, sponsored by the Army Ballistic Missile Agency.

Director, Department of Applied Mechanics. Member ARS.

Senior Research Engineer, Department of Applied Mechanics.

<sup>&</sup>lt;sup>4</sup> Numbers in parentheses indicate References at end of paper.

### Similitude Relations—Translational Excitation

The relevant parameters, based on the preceding discussion, will be taken as

a = longitudinal acceleration on tank, LT<sup>-2</sup>

d = tank diameter, L

F = resultant liquid force on tank wall, MLT-2

h = depth of liquid in tank, L $X_0 = \text{excitation amplitude, L}$ 

 $X_0$  = excitation amplitude, L  $\mu$  = liquid viscosity,  $ML^{-1}T^{-1}$ 

 $\rho$  = liquid density, ML<sup>-3</sup>

 $\tau$  = excitation period, T

An equation relating these eight parameters analytically can be written in the general form (5)

$$\varphi'(\pi_1, \pi_2, \pi_3, \ldots, \pi_{n-m}) = 0$$
 [1]

where

n = number of physical parameters involved

m = number of fundamental dimensions (in this casen - m = 8 - 3 = 5)

The  $\pi$ 's are dimensionless combinations of the parameters listed. Proceeding in conventional fashion, similitude theory yields expressions for the various dimensionless groups. The general solution of the form of Equation [1] may then be written in terms of the  $\pi$ 's as

$$\frac{F}{(\rho d^3)(d/\tau^2)} = \varphi \left[ \frac{a}{d/\tau^2} \cdot \frac{h}{d} \cdot \frac{X_0}{d} \cdot \frac{\rho d(d/\tau)}{\mu} \right]$$
 [2]

We note that all linear dimensions are scaled in the same ratio as the diameter, that the group  $a\tau^2/d$  is equivalent to Froude's number, and that the group  $\rho d(d/\tau)/\mu$  is equivalent to Reynolds' number.

Should interest reside not in the resultant liquid *force* on the tank wall, but rather in the resultant liquid *pressure*, a similar analysis would yield

$$p = f(F/d^2) ag{3}$$

so that in place of the dimensionless force  $F/[(\rho d^3)(d/\tau^2)]$  in Equation [2], we may write

$$\frac{p\tau^2}{\rho d^2} = \frac{p}{\rho (d/\tau)^2} \tag{4}$$

which is in the form of a pressure coefficient (Euler number).

The preceding analysis has considered the excitation to be a

The preceding analysis has considered the excitation to be a displacement, in anticipation of actual model experiments. The excitation could, however, have been taken equally well as a force P (or even an acceleration), in which case the appropriate dimensionless group would become

$$P/[(\rho d^3)(d/\tau^2)]$$
 [5]

Consideration of the surface tension in the foregoing analysis would have resulted in a new dimensionless group of the form  $\rho d^3/\sigma \tau^2$ , which corresponds to a Weber number. As will be seen later, the simultaneous solution of this new group and  $\rho d(d/\tau)/\mu$  would be exceedingly difficult, in view of the model liquids readily available. Further, we assume that surface tension forces are small compared with the inertial and viscous forces, and consequently we shall omit any additional consideration of surface tension.

### Similitude Relations—Rotational Excitation

In this case the pertinent parameters remain the same as in the translational case, except that the excitation is now defined by two parameters, the angular rotation  $\theta_0$  and the location of the rotational axis b. Since we consider only small excitation amplitudes, it may be noted that  $b\theta_0 \simeq X_0$ , and, therefore, the general functional Equation [2] applies to both kinds of excitation. The use of a moment M = Pb as the

excitation would result in a group formed by Equation [5] multiplied by the ratio b/d.

larg

or l

has

reas

ven

pro

For

divi

The

goir

mod

the

mod

tion

reno

inal

sati

mod

Sca

tie

full-

the

wer

sim

fore

Me

it is

Jui

# Modeling Considerations Based on the Similitude Relations

### General

Equation [2], and the associated alternate expressions for special cases, governs the design of models to simulate a given prototype. If all dimensionless groups in this equation have the same numerical value for both model and prototype, then the forces and pressures measured on the model are directly applicable to the prototype.

We note that fluid depth and excitation displacement amplitude are scaled in the same proportion as the geometrical scale. Thus (the ratio of model to prototype parameters is denoted by the subscript r)

 $d_{\tau} = d_m/d_p \tag{6}$ 

$$h_r = X_{0_r} = b_r = d_r$$
  $\theta_r = 1$  [7]

The remaining model parameters are to be established by further study of Equation [2].

### Modeling Considerations-Viscosity Neglected

In the case that viscous effects are neglected throughout, the Reynolds number group drops out of the analysis given previously, and the relation between model and prototype depends on the geometrical factors discussed and the time scale factor

$$\tau_r^2 = d_r/a_r \tag{8}$$

This result means that any size model in a 1-G acceleration field can be used to simulate any size prototype in any acceleration field by varying the time scale, and would further permit the use of any model liquid, since only the density appears in the force (or pressure) parameter.

In presenting measured data, the parameter  $a\tau^2/d$  may be used as the primary independent variable. Since frequency is a more commonly used variable, it may be introduced for the inverse of the period to give  $d\omega^2/a$ . The force (or pressure) group may also be modified by introduction of Equation [8] to

$$\frac{F}{\rho ad^2}$$
 or  $\frac{p}{\rho ad}$  [9]

The measured data may then be presented with  $d\omega^2/a$  as the primary independent variable,  $F/\rho ad^3$  as the dependent variable, and the remaining quantities as secondary independent variables.

### Modeling Considerations-Viscosity Included

With viscous forces included, the data may still be presented as indicated; however, the model design is now subject to certain restrictions arising from the Reynolds number group. Introducing Equation [8] we find

$$\frac{\rho d(d/\tau)}{\mu} = \frac{\rho d^{3/2} a^{1/2}}{\mu}$$
 [10]

from which

$$d_r = (\mu_r/\rho_r)^{2/3} a_r^{-1/3}$$
 [11]

This important result shows that the geometrical scale is determined by the acceleration, liquid density and liquid viscosity ratios. If it is desired to test models so as to cover a range of prototype accelerations, we may either fix the model diameter and vary the liquid properties, or fix the model liquid and vary the model size. Since the range of liquid properties is very restricted, a combination of these courses may be chosen.

In order to employ models of reasonably small size to study large prototypes, the model liquids must have high density or low viscosity, or both, compared to the prototype liquid, as inspection of Equation [11] indicates. Mercury, of course, has a very high density, but is undesirable for a variety of reasons, such as toxicity and cost; some of the organic solvents have very low viscosity and, therefore, offer some promise.

As an example of model simulation, assume the following typical case:

Parameter	Prototype (kerosene)	Model (methyl- ene chloride)		
Specific gravity	0.83	1.336		
Viscosity	2.5 cp	0.465 cp		
Acceleration	$15$ $\hat{G}$	1 G		
Diameter	9 ft	(to be derived)		

For a prototype acceleration of 1 G

$$d_{\rm r} = (1)^{-1/3} \left(\frac{1}{8.65}\right)^{2/3} = \frac{1}{4.21}$$

$$d_m = d_p d_r = \frac{9}{4.21} = 2.14 \text{ ft}$$

For any other prototype acceleration, the model size is 2.14 divided by the cube root of the acceleration ratio. Thus

$$(d_m)_{bG} = 2.14/(1/5)^{1/s} = 3.66 \text{ ft}$$

Therefore, a 9-ft diameter prototype with kerosene fuel undergoing accelerations from 1–5 G may be simulated by a series of models of 2.14 to 3.66-ft diameters with methylene chloride as the model liquid. The range of excitation frequencies for the model is determined from Equation [8] as

$$\omega_r = \frac{1}{\tau_r} = \left(\frac{a_r}{d_r}\right)^{1/2} = 2.502 - 0.701$$

It is clear from the foregoing that the inclusion of an additional group to account for surface tension would have rendered the model design virtually impossible, because of the inability to find a model liquid of appropriate properties to satisfy all dimensionless groups simultaneously in a small model.

## Modeling Considerations—For Comparison With Full-Scale ABMA Tests

The availability of test results obtained by the Army Ballistic Missile Agency on a full-scale missile tank provides the means for verifying the results of the foregoing analysis. The full-scale tank tests were conducted on the ground with water as the "fuel" and with the excitation as translational. Two different types of suppression devices employed in these tests were simulated with the model.

The prototype (full-scale) parameters pertinent to the similitude requirements are

d, tank diameter = 8.75 ft

 $\rho$ , liquid density = 1.938 slugs/ft<sup>3</sup>

 $\mu$ , liquid viscosity = 1.00 cp

a, acceleration = 1 G

The model is necessarily in a 1-G acceleration field, therefore its diameter is determined by Equation [11] as

$$d_m \, = \, 8.75 \bigg( \frac{\mu_m}{\rho_m} \cdot \frac{1.938}{1.00} \bigg)^{1/3} \bigg( \frac{1}{1} \bigg)^{-1/2}$$

In order to obtain a reasonably small model  $(\frac{1}{4} - \frac{1}{10} \text{ scale})$ , it becomes necessary to choose a liquid with suitable values of viscosity and density, in accordance with this equation. Methylene chloride appears suitable as a model liquid, since it is nonflammable and relatively free of toxic hazards; how-

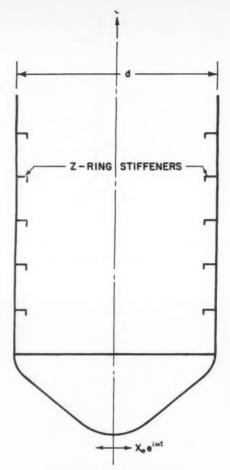


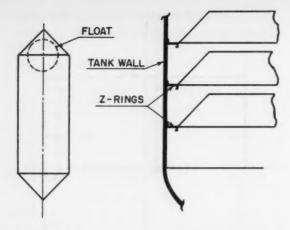
Fig. 1 Basic tank configuration

ever, it does have the disadvantage of being a solvent for most plastics and thus eliminates the use of models made of transparent Plexiglas or lucite. Inserting the properties of methylene chloride (6) into the previous equation yields a model diameter of 4.33 ft, which is somewhat larger than desirable. Since no other suitable model fluids could be found. models of 14.4- and 25.0-in. diameters were finally selected. This meant that exact simulation of the ABMA full-scale tests (with water) could not be accomplished (although "in-flight" simulation was possible, as mentioned previously). However, it appeared that by employing various model sizes and liquids (e.g., water, methylene chloride, methylene bromide), it would be possible to provide a sufficient variation in Reynolds number to yield useful information regarding the damping effectiveness of slosh suppression devices. This will be discussed later.

### **Experimental Arrangements**

### Models

The models were fabricated from rolled steel cylinders with spun conical bottoms, geometrically similar to the full-scale tank (see Fig. 1). The Z-ring stiffeners have a width of approximately 3 per cent of the tank diameter and are perforated with lightening holes. The two types of suppressor configurations consisted of floating can devices and truncated



FLOATING CAN

CONICAL RINGS

Fig. 2 Suppressor configurations

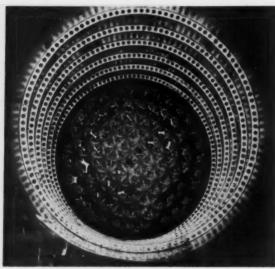


Fig. 3 Floating cans on liquid surface

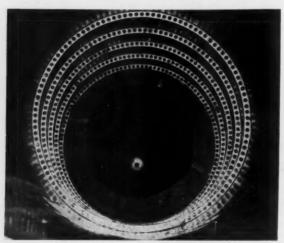


Fig. 4 Conical rings mounted in tank

conical rings, both of perforated material (approximately 25 per cent open). The cans and conical rings are shown in Figs. 2–4. The model suppressor devices were also geometrically similar to their full-scale counterparts.

### Test Facility

The excitation system basically involves a rigid platform whose motion can be held to straight line oscillation in a horizontal plane, driven by a slider-crank mechanism of variable crank-throw and variable crank velocity. The slider-crank mechanism gives sinusoidal motion to the slider element with a maximum error of 2 per cent. The platform oscillates on four pairs of cam-follower rollers, which roll on hardened steel bars. Sidewise movement is prevented by four small cam-follower rollers whose axes are at right angles to the main rollers. The system is mounted on a heavy test frame bolted to a concrete floor, with a dummy platform to provide balance for the system set up at the opposite end of the test frame. The dummy platform oscillates at the same amplitude and frequency as the tank platform, but with a phase displacement which produces smooth sinusoidal motion. The mass of the dummy platform is matched to that of the tank platform by adding or removing weights. The drive for the system consists of a variable speed d-c motor, driven by a motor-generator set.

The complete facility is shown in Fig. 5. It may be mentioned that this facility has been designed and constructed to produce rotational excitation of the model tank, if desired.

### Instrumentation

Instrumentation is provided to measure the following quantities:

- 1 Tank displacement.
- 2 Total force produced by the fluid on tank wall.
- 3 Total moment produced by the fluid about tank
  - 4 Pressure distribution of the fluid on tank wall.

All quantities are recorded simultaneously on a 16-channel oscillograph. The trace of tank displacement, measured by the deflection of a thin cantilever beam, is used as a reference for phase relationships of all other parameters.

Total force and moment measurements are considered together, since a single system can be designed to provide both measurements (7). The measurement is accomplished by use of a cantilever beam dynamometer system. The model is mounted on four instrumented beams or arms. For force measurements, the force strain gages on the individual arms

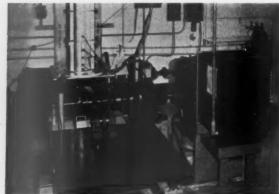


Fig. 5 Experimental facility

are

me

ori

arr

DU

pro

wit

the

thu

The sul The onle car und dyn

fina the tion

Ju

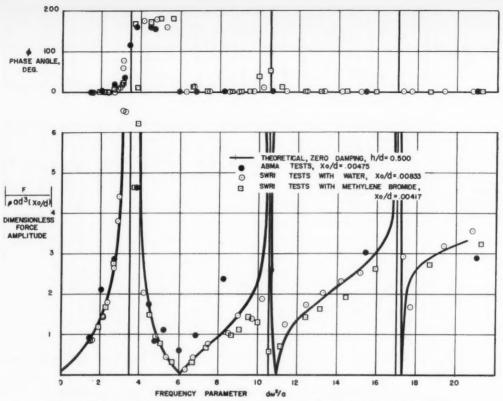


Fig. 6 Comparison of model and ABMA full-scale tests, no damping device, h/d=0.505

are oriented in the bridge circuit to be sensitive only to bending (or lateral) loads in the arms, and the four arms are summed in the bridge to measure the total force. For moment measurements, the moment gages on the individual arms are oriented in the bridge so as to be sensitive only to axial (or vertical) loads in the arms. The outputs from the two forward arms in the line of motion are summed in the bridge and output from the aft arms subtracted. Hence the difference is proportional to the pitching moment about an axis in line with the pinned platform attachment.

A major disadvantage to this type of dynamometer system is that part of the signal output is due to the mass inertia of the tank model, platform and dynamometer arms. These inertia forces may be of the same order of magnitude as the forces due to liquid motion, or in some cases may be even higher; thus separate calibration of the inertia response is required. The loads resulting from liquid motion are then obtained as the difference between two large loads [(inertia + liquid) inertia]. It is possible, however, to cancel the signals resulting from inertia loads directly in the electrical circuits. The remaining signal is then proportional to the liquid loads only, and may be amplified to obtain reliable readings. The cancellation is accomplished by providing a separate system undergoing the same motion, dynamically similar to the dynamometer-tank system but without the liquid loading. The output from this "balance" system is fed into the dynamometer bridge circuit with a phase difference of 180 deg. The balance mass may be adjusted mechanically to nearly cancel the inertia signal from the dynamometer system, and final trim may be accomplished by electrical attenuation of the balance system. A dynamic check of the static calibration, using a rigid mass in the tank, established the accuracy of the net (remaining) signal response.

Pressure distributions on the tank wall are measured by

means of pressure cells mounted essentially flush with the tank wall. Pressure measurements can be made at various heights in the tank and along the circumference at one height, for the purpose of integrating the pressure distribution for correlation with the total force and theory.

Only the total force measurements shall be discussed in the present paper; it is planned to present other measured data in subsequent papers.

### Test Results

### Force Data

Figs. 6-11 compare force data from some of the model tests and the ABMA full-scale tests. The liquid height to tank diameter ratios of 0.785, 0.595 and 0.505 correspond to the height of the liquid above the bottom of an equivalent flat bottomed tank of the same volume. In all of these figures, the abscissa is the dimensionless excitation frequency  $d\omega^2/a$ , and the ordinate is the dimensionless total fluid force  $F/(\rho ad^3)(X_0/d)$ . This form of the dimensionless total force differs from that of Equation [9] by the introduction of the excitation amplitude, and has been employed only for convenience. Also for convenience, the total force has been given in terms of absolute magnitude and phase angle  $\phi$ . Theoretical response curves applicable, of course, only for the case of zero damping, have been shown in some of the figures for comparative purposes. Only a small portion of the test data actually obtained is presented in the present paper because of space limitations.

Fig. 6 presents the results of one of a series of tests with no damping device. The model tests were made with both

<sup>&</sup>lt;sup>5</sup> The tests referred to here actually do involve the Z-ring stiffeners, which may be regarded as a type of damping device.

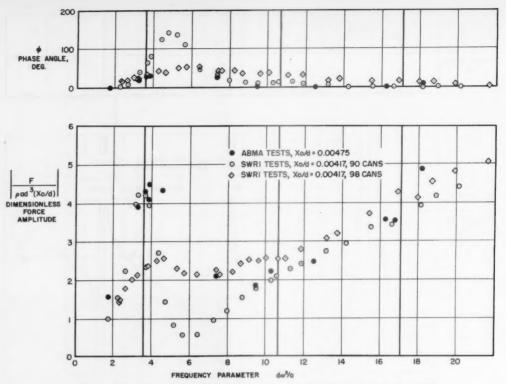


Fig. 7 Comparison of model and ABMA full-scale tests, floating cans,  $\hbar/d=0.595$ 

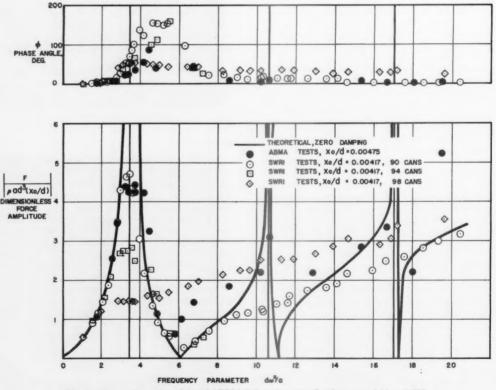


Fig. 8 Comparison of model and ABMA full-scale tests, floating cans,  $h/d\,=\,0.505$ 

ARS JOURNAL

608

neg that is fu the ing this sho F test nific equ the the par tha mod

the

acei

dan the sary

deri S may (Fig

the

from

wat

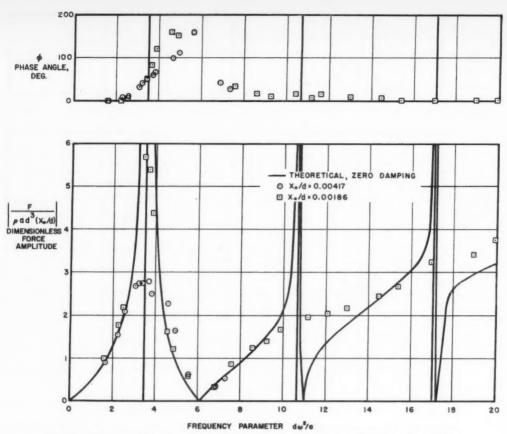


Fig. 9 Effect of excitation amplitude on damped forces, floating cans (94 cans), h/d=0.505

water and methylene bromide. Since the points appear to coincide, it is apparent that the Z-ring stiffeners add only negligible damping to sloshing characteristics, and therefore that viscous effects are negligible for this configuration. This is further indicated, in Fig. 6, where the points generally follow the theoretical curve corresponding to the case of zero damping (8–11). Agreement with the ABMA full-scale tests in this configuration is very good, except that the full-scale tests show considerable scatter.

Figs. 7, 8, 10 and 11 are comparisons of model and full-scale tests with the two types of suppression devices. Since significant damping is present with these configurations and the equivalent Reynolds numbers are quite different (1.680  $\times$  106 for the model tests and  $13.95 \times 10^{6}$  for the full-scale tests), the model tests may not be regarded as exact simulation of the full-scale tests. Therefore these results should be compared only on a qualitative basis. Thus, it may be noted that although the peak forces in the first mode, comparing model and full-scale data, are of the same order of magnitude, the large scatter in the full-scale data does not permit any accurate comparison of these peak forces. Since the effects of damping (except for very large values) are significant only in the immediate neighborhood of resonance, it is therefore necessary to discuss the magnitude of the damping in terms of derived damping factors, as given later in the paper.

Some interesting features of these comparisons, however, may be discussed on a qualitative basis. The floating cans (Figs. 2 and 3) provided the data of Figs. 7 and 8. Tests

were first made with 90 cans (91 were actually used in the full-scale tests), which show general agreement with the full-scale tests although, again, the latter show considerable scatter. Tests were then made with 98 cans, the number required to cover the liquid surface completely; these tests showed considerably more damping, the effect being more pronounced as the liquid height was decreased. An additional run was made through the first resonance at h/d=0.505 (Fig. 8) with 94 cans; the damping appeared to affect only the peak force.

These tests were made at approximately the same excitation amplitude to tank diameter ratio as that of the full-scale tests  $(X_0/d=0.00417$  for the model tests vs. 0.00475 for the full-scale tests). An additional run at roughly half the previous amplitude was made at h/d=0.505 with 94 cans to investigate the effect of excitation amplitude on damping. As indicated in Fig. 9, there is little difference in the measured forces except at the peak of the first mode. The effect here is considerable. The dimensionless peak force at the lower excitation amplitude is nearly twice that of the higher excitation amplitude, showing a large increase in damping with increasing excitation amplitude.

Results of tests with perforated conical rings (Figs. 2 and 4) are presented in Figs. 10 and 11. As with the 90 floating cans, agreement with the full-scale tests is relatively good, especially in the region of the first mode, although the full-scale test data again show considerable scatter.

Rather extensive data for tanks in translation or rotation, with and without suppressors and applicable to a variety of "in-flight" conditions, have been or are currently being obtained as part of the present program, and may be presented in subsequent papers.

<sup>&</sup>lt;sup>6</sup> The analyses of these several references are equivalent; the theoretical curves shown in the present paper were computed from the particular form of the analysis given in (8).

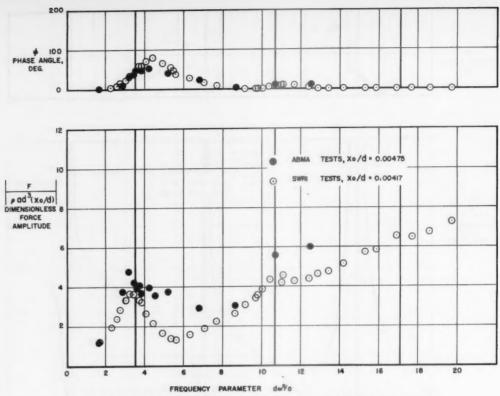


Fig. 10 Comparison of model and ABMA full-scale tests, conical rings,  $\hbar/d\,=\,0.785$ 

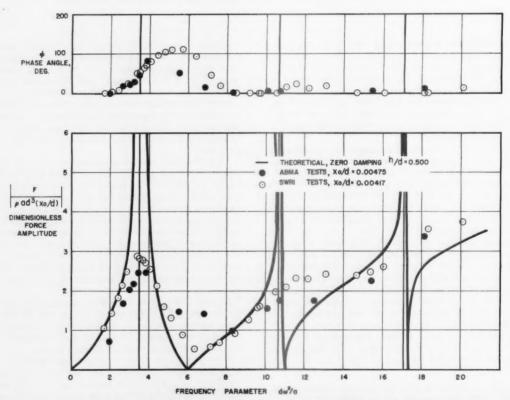


Fig. 11 Comparison of model and ABMA full-scale tests, conical rings,  $\it h/d = 0.505$ 

Dam

The device tests by an inque Fig. Reym room noted is eas slight tests fluids

tank-It : to the the colors at Al celers on da believ of da mode respo of the

floati those and a taine consid data,

Da

and slautho

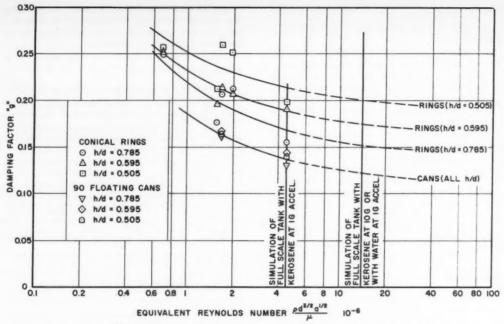


Fig. 12 Variation of damping factor with equivalent Reynolds number,  $X_0/d=0.0045$ 

### Damping Factors

The damping provided by these two types of suppression devices was measured from the force response data, from tests with two sizes of models (14.4 and 25.0 in. in diameter) by an iterative procedure based on the half bandwidth technique applied to the test data, as given and described in (12).

Fig. 12 shows a plot of damping factor g vs. the effective Reynolds number, using values of density and viscosity at room temperature taken from published tables (6). It is noted from this figure that simulation of full-scale conditions is easily possible for kerosene at 1 or more G by employing a slightly larger model tank, but that simulation of full-scale tests for water at 1 G is not possible with any of the model fluids employed. Values of  $\rho d^{3/3} a^{1/2}/\mu$  for the various model tank-liquid combinations are given in Table 1.

It may be further noted from Fig. 12 that the damping due to the 90 floating cans is consistently lower than that due to the conical rings. The damping factors at  $\rho d^{3/2}a^{1/2}/\mu=13.95\times 10^6$ , corresponding to the full-scale water tests made at ABMA, and also to the same tank with kerosene at an acceleration of 10 G, are obtained by extrapolation. These data on damping factors appear to be relatively consistent, and it is believed that the extrapolation is reasonable. Comparisons of damping factors, as obtained by this extrapolation from model data (Fig. 12), and as obtained from iteration of force response and comparison with a family of theoretical curves of the ABMA tests (12), are given in Table 2.

Damping factors obtained from the model tests with both floating cans and conical rings agree reasonably well with those obtained from a comparison between the full-scale tests and a family of theoretical curves. The damping factors obtained directly by iteration from the full-scale tests are not considered to be reliable because of the large scatter of the data, and are given here only to complete the comparison.

The former procedure introduces some smoothing of the data and should provide more accurate values, although there is some evidence to indicate that the damping factors thereby obtained are somewhat high. Thus, a reduction of those values would tend to improve even further the agreement with those obtained from the model test data.

The essential result to be noted from Fig. 12 is, however, that the damping factors are quite definitely dependent upon the equivalent Reynolds number. Although there is some scatter in the damping factors obtained from the model test data, this does not negate the principal feature involved. These results demonstrate quite clearly that model studies in which damping or slosh suppression devices are involved cannot be conducted without due regard for the requirements imposed by similitude theory.

Table 1 Effective Reynolds numbers for various models

Model tank—liquid	Effective Reynolds number, $\rho d^{3/2}a^{1/2}/\mu$
small-water	$0.686 \times 10^{6}$
large-water	$1.565 \times 10^{6}$
small-methylene bromide	$1.680  imes 10^{6}$
small-methylene chloride	$1.970 \times 10^{6}$
large—methylene chloride	$4.500 \times 10^{6}$

Table 2 Damping factor g at  $\rho d^{2/2} a^{1/2} / \mu = 13.95 \times 10^6$ 

			ABMA Results				
		SwRI results from Fig. 12		From comparison with theoretical curves		By iteration from full-scale experiment	
h/d	cans	rings	cans	rings	cans	rings	
0.505	0.125	0.200	0.136	0.28	0.20	0.25	
0.595	0.125	0.175	0.146	0.28	0.25	0.28	
0.785	0.125	0.152	0.191	0.16	0.211	0.21	

<sup>&</sup>lt;sup>7</sup> The viscosity of methylene bromide given in (6) is incorrect and should be multiplied by 10. This error was pointed out to the authors by Professor Paul E. Sandorff of MIT.

### Conclusions

The data presented in the present paper permit several conclusions to be drawn:

1 Model experiments performed in accordance with the similitude requirements derived herein can be used to provide quantitative data which can be applied directly to full-scale tanks, even with large amounts of damping present. The relatively good agreement obtained between the model and full-scale tests lends confidence to the prospect of simulation of "in-flight" sloshing characteristics.

2 Stiffener rings with lightening holes, of the order of width used in this configuration (3 per cent of tank diameter),

add negligible damping to sloshing forces.

3 The amount of damping produced by both floating cans and conical rings is strongly dependent upon excitation amplitude. For this configuration, the perforated conical rings provide more damping than the 90 floating cans, and approximately the same amount of damping as 94 cans (at an excitation amplitude of  $X_0/d = 0.00417$ ). The damping provided by conical rings is furthermore dependent on the depth of liquid in the tank.

### Acknowledgments

The authors wish to express their appreciation to the Army Ballistic Missile Agency for permission to publish this paper. Special appreciation is due to the staffs of the Mechanical De-

velopment Section and the Computations Laboratory of the Department of Applied Mechanics of Southwest Research Institute, and particularly to Luis R. Garza, for invaluable assistance during this program.

the

ใดส

lim

the

has

boo

hor

ang

Dro

cor

tio

atio

coa

era

hol wit

ran

sta

niii ver me val am rep

Eq

cele

and dur

rocl

The

iect

kine pen the

Equ

pro

intr

App

mat

Jui

### References

Brown, K., "Laboratory Test of Fuel Sloshing," Douglas Aircraft Co.,
 Inc., Rep. no. SM-Dev. 783.
 Case, K. and Parkinson, W. C., "The Damping of a Liquid in a Right
 Circular Cylindrical Tank," Ramo-Wooldridge, Los Angeles, Rep. CM

48-75, Sept. 1956.

3 Howell, E. and Ehler, F. G., "Experimental Investigation of the Influence of Mechanical Baffles on the Fundamental Sloshing Mode of Water

fluence of Mechanical Baffles on the Fundamental Sloshing Mode of Water in a Cylindrical Tank," Ramo-Wooldridge, Los Angeles, Rep. GM 45, 3-87, GM-TR-69, July 1956.

4 Eulitz, W., R., unpublished work, ABMA, Huntsville, Ala., 1957.

5 Langhaar, H. S., "Dimensional Analysis and Theory of Models," John Wiley and Sons, Inc., N. Y., 1953.

6 Hodgman, C. D., Ed., "Handbook of Chemistry and Physics," Chemical Rubber Publishing Co., Cleveland, 34th ed., 1952, p. 1887.

7 Epperson, T. B., Pengelley, C. D., Ransleben, G. E., Jr., Wilson, L. E., and Younger, D. G., "Nonstationary Airload Distributions on a Straight, Flexible Wing Oscillating in a Subsonic Wind Stream," Classified Title Unclassified), WADC TR 55-323, Jan. 1956.

8 Bauer, H. F., "Fluid Oscillations in a Circular Cylindrical Tank," ABMA Rep. no. DA-TR-1-58, April 1958.

9 Miles, John W., "On the Sloshing of Liquid in a Cylindrical Tanl." Ramo-Wooldridge, Los Angeles, Rep. AM 6-5, April 1956.

Ramo-Wooldridge, Los Angeles, Rep. AM 6-9, April 1490.

10 Kachigan, K., "Forced Oscillations of a Fluid in a Cylindrical Tank."

Convair, San Diego, Rep. ZU-7-046, Oct. 1956.

11 Schmitt, A. F., "Forced Oscillations of a Fluid in a Cylindrical Tank

Undergoing Both Translation and Rotation," Convair, San Diego, Rep. ZU-7-069, Oct. 1956.
 12 Bauer, H. F., "Fluid Oscillations in a Cylindrical Tank with Damping," ABMA, Huntsville, Ala., Rep. DA-TR-4-58, April 1958.

# **Rocket Boost Trajectories for Maximum Burnout Velocity**

L. J. KULAKOWSKI<sup>2</sup> R. T. STANCIL<sup>3</sup>

Convair-Fort Worth Div., General Dynamics Corp. Fort Worth, Texas

The problem considered is the definition of optimal trajectory programs which allow a given rocket boost vehicle to launch its payload with maximum velocity, for prescribed burnout values of the path angle and altitude. Methods of the calculus of variations are employed to achieve the desired solutions. The equations of motion consider a spherical nonrotating Earth model and include the effects of aerodynamic forces. Inequality constraints suitable for satisfying certain practical vehicle design and physiological limits are introduced. An optimal coasting period of initially unspecified duration may be included in the trajectory to provide increased burnout altitude. Numerical results illustrating the utility and validity of the method are included.

THE ADVENT of spaceflight and quasi-spaceflight places particularly stringent requirements on the performance of rocket boost systems. Maximum mission performance is

realized only by insuring the most efficient transfer of impulse from the given boost system to the spacecraft. may be achieved by properly programming the boost trajectory, with due consideration of the constraints imposed by the vehicle design and the capabilities of the control system employed. It is currently common practice to program boost trajectories by what may best be described as "educated" guessing of the values of certain control parameters.

This paper presents a method for the determination of optimal boost trajectory programs (extremals) which yield

Received Jan. 15, 1959.

<sup>1</sup> The authors are indebted to L. G. Walker of the Convair-Fort Worth Computation Laboratory for the IBM 704 computer programming of the procedure and to J. L. Lindsey of the Aero Sciences Group for contributing to the problem statement for

the computer program.

<sup>2</sup> Design Specialist, Aero Sciences Group. Member ARS.

<sup>3</sup> Sr. Aerodynamics Engineer, Aero Sciences Group.

the maximum burnout velocity for a specified booster, payload and mission. The proposed method is useful in the preliminary booster design period for defining ultimate performance capability, indicating efficient means of utilizing the available control systems and providing a systematic basis for evaluating performance trades resulting from design modifications.

Specifically, the proposed method yields the time history of the two-dimensional boost trajectory which results in the maximum burnout velocity attainable by a given multistage booster configuration, subject to specified initial and final boundary conditions. Initial conditions used (velocity, path angle and altitude) allow for either ground or air launching; the final conditions include the path angle and altitude appropriate to the mission under consideration. Effects of aerodynamic forces are included. The trajectories may be constrained to satisfy limits imposed by structural deformation longitudinal stability, aerodynamic heating and accelerations acting on the crew of the spacecraft. An optimal coasting period may be included in the extremal, if desired.

Solutions derived herein are based upon application of methods from the calculus of variations. As such, the general approach to the problem is similar to those used by Liebhold and Brown (1)<sup>4</sup> and Leitmann (2), who were concerned with the derivation of boost trajectories yielding maximum range for ballistic missiles. Inclusion of an optimal coasting stage between powered stages is made possible by a special interpretation of the basic variational problem.

Use of a high speed digital computer is required to calculate numerical solutions by the proposed method. In the interest of promoting efficient computer utilization, a rapidly converging iteration technique is adapted to the proposed method.

Two numerical examples are included to illustrate the validity and utility of the proposed method. In these examples, extremals are determined for the launching of circular satellite and boost-glide vehicles by a hypothetical booster representative of a moderately advanced solid rocket.

### **Equations of Motion**

In this analysis the rocket is taken to be a point mass moving in the vicinity of a spherical nonrotating Earth (or other celestial body). Orientation of the rocket relative to Earth and the force, velocity and acceleration vectors which exist during flight are illustrated in Fig. 1. The trajectory of the rocket satisfies the following equations

$$\begin{split} m\dot{\vartheta} &= T\cos\alpha - D - mg\sin\gamma \\ m\vartheta\left(\dot{\gamma} - \frac{\vartheta}{R+h}\cos\gamma\right) &= T\sin\alpha + L - mg\cos\gamma \\ \dot{h} &= \vartheta\sin\gamma \end{split}$$

where the dots above the symbols denote time derivatives. The first two of these are the equations of motion for trajectory oriented reference axes whereas the third is a purely kinematic relationship required to allow the use of four dependent variables  $(\vartheta, \gamma, h \text{ and } \alpha)$  in the problem. Since the time derivative for the angle of attack does not appear in Equations [1], the angle of attack  $\alpha$  is the control variable (i.e., driving function) in the problem.

A spherical nonrotating Earth model was selected as a compromise which provides useful trajectory results without introducing the complications of oblateness and rotation. Approximate gross effects of Earth's rotation may be applied to solutions derived by the proposed method for closer estimates of burnout conditions. Effects of thrust deflection

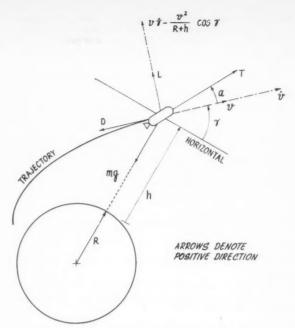


Fig. 1 Orientation and vector system of rocket

were also ignored, principally to eliminate an additional dependent variable from the problem. In most instances the errors resulting from neglecting thrust deflection will be well within the accuracy levels ordinarily associated with preliminary design studies.

For the purposes of this analysis it is assumed that the mass, thrust, lift, drag and acceleration of gravity are known at all points of the boost trajectory and have the following prescribed functional dependence: m = m(t), T = T(h, t),  $L = L(\theta, \alpha, h)$ ,  $D = D(\theta, \alpha, h)$  and g = g(R + h). Note that this excludes the effects of aerodynamic lag in the application of the aerodynamic forces.

### **Trajectory Optimization**

Prior to initiating the analytical development of an optimization technique, due consideration must be given to the selection of the parameter to be extremized. This involves the character of the vehicle considered as well as its general mission capabilities. Numerous papers appearing in the literature discuss the single mission concept, i.e., maximizing such things as ballistic range, satellite orbit altitude, burnout height, etc., leading the uninitiated reader to believe that variational techniques are somewhat specialized. The value of any vehicle/mission optimization technique is directly dependent on the overall utility of the technique in designing vehicles or programming their trajectories for a variety of missions. A primary goal of the subject study involves formulation of a technique having wide utility.

The principal purpose of a rocket booster is to convert the latent energy of its propellants into useful energy of the payload. In this sense, useful energy is defined as the energy required to perform a given mission most efficiently. It is not to be confused with maximum energy which is, in most instances, neither required nor desired. For sensible mission planning, the useful energy so imparted must be suitably directed by specifying the direction of the velocity vector and the burnout altitude. In this format, the proposed tech-

 $<sup>^{4}</sup>$  Numbers in parentheses indicate References at end of paper.

nique to be described provides valuable design information for the many types of missions whose extremals are members, defined by appropriately specified values of burnout altitude and path angle, of the family of maximum velocity trajectories.

Rocket burnout velocity is determined by integration of the first of Equations [1]

$$\vartheta_f = \int_{t_0}^{t_f} \dot{\vartheta} dt + \vartheta_0$$
 [2]

The problem considered here is to determine those functions  $\vartheta(t)$ ,  $\gamma(t)$ , h(t) and  $\alpha(t)$  which maximize the integral [2] subject to certain specified boundary conditions and constraints. Initial boundary conditions used specify the velocity, path angle and altitude at the beginning of the trajectory, i.e.

at 
$$t = t_0$$
,  $\vartheta = \vartheta_0$   $\gamma = \gamma_0$   $h = h_0$  [3]

Terminal boundary conditions used are:

at 
$$t = t_i$$
,  $\gamma = \Gamma$   $h = H$  [4]

Values of  $\Gamma$  and H are deduced from the mission being considered.

Three of the constraints employed require that Equations [1] be satisfied at all points of the trajectory. These equations are written in the form

$$\varphi_1 = \dot{\vartheta} - F(\vartheta, \gamma, h, \alpha, t) = 0$$
  
 $\varphi_2 = \dot{\gamma} - G(\vartheta, \gamma, h, \alpha, t) = 0$   
 $\varphi_3 = \dot{h} - \vartheta \sin \gamma = 0$ 

Solutions obtained with use of only these three constraints are of interest, but may be impractical when the physical limitations of the vehicle or its crew are considered. Such a contingency is anticipated, and may be avoided, by the addition of an inequality constraint of the form

$$\varphi_4 = L_m - l_m(\vartheta, \gamma, h, \alpha) \ge 0 \qquad m = 1, 2, 3 \dots$$
 [6]

where each  $l_m$  must be an explicit function of  $\alpha$ , and  $L_m$  is the corresponding limiting value.

Since there are four dependent variables in the problem, using the equality form of just one of the constraints [6] together with Equations [5] uniquely determines the boost trajectory. For practical applications a number of limitations are prescribed for a given problem. In the event that more than one limit is violated at a given time, the computer selects and uses the most critical. An extremal must be free of all the constraints [6] for some portion of the powered flight. Otherwise, the variational problem degenerates into an ordinary assumed trajectory program problem.

### Design and Physiological Constraints

Before proceeding with further discussion of the variational problem it is appropriate to note some types of limitations which may be satisfied by use of the inequality constraints [6]. One of the more obvious vehicle design limitations is the normal load factor. This may be satisfied by a dual purpose constraint. Let the angle  $\beta$  be measured positive aft of the normal to the vehicle longitudinal axis. Then, the acceleration vector acting in the  $\beta$ -direction has the magnitude

$$l_1 = -\frac{T}{m}\sin\beta + \frac{L}{m}\cos(\alpha + \beta) + \frac{D}{m}\sin(\alpha + \beta) \quad [7]$$

When  $\beta$  equals zero deg, Equation [7] gives the normal acceleration.

In manned vehicles, the principal physiological limitations during boost are prescribed by human tolerance to acceleration, which is affected significantly by the direction of the acceleration vector. Thus, Equation [7] may be used to satisfy such limitations, provided that  $\beta$  is specified in the direction of the least human tolerance to acceleration.

Other vehicle design limitations are imposed by structural deformation, longitudinal stability and aerodynamic heating. Accurate definition of these limits requires complex analyses which are not appropriate to the present study. However, trajectory constraint may be achieved without undue complication by use of certain similarity-type parameters.

A structural bending of the boost vehicle may be caused by aerodynamic loads which, for most boost trajectories, are critical at relatively low altitudes and moderate supersonic speeds. If the booster is aerodynamically stabilized or is carrying a winged payload, the aerodynamic loading acting on the fins or wing produces most of the bending moment. This loading is nearly proportional to the product of the dynamic pressure and angle of attack. Hence, the relationship

$$l_2 = (1/2)\rho \vartheta^2 |\alpha|$$
 [8]

may be used to control the structural bending.

Vehicle static longitudinal stability is ordinarily acceptable if the angle of attack remains within certain limits at a given Mach number. Thus, an appropriate control parameter is

$$l_3 = |\alpha|$$
 [9]

In this case  $L_0$  may be specified as a function of Mach number. Aerodynamic heating limitations may be satisfied by using a control parameter of the form

$$l_4 = T_{ew}(\vartheta, h, \alpha)$$
 [10]

where  $T_{ew}$  is the equilibrium wall temperature at an adroitly selected point of the vehicle's surface. The presumption here is that the equilibrium wall temperature at the selected point will be representative of that over the remainder of the body and, therefore, serves as a suitable control over the total heat absorbed. Forms of equations used for computing  $T_{ew}$  will depend on the vehicle surface shape and the location selected for the monitored point. A general representation may be achieved by approximating  $T_{ew}$  in Equation [10] with a polynomial surface within a critical region of the  $\vartheta$ , h,  $\alpha$  space.

The control functions noted in Equations [7 through 10] are used solely to modify unsuitable extremals. That is, an unconstrained extremal is determined first and the controls are used only as required to derive a constrained optimal path which satisfies the pertinent vehicle design and physiological limitations.

### **Euler-Lagrange Equations**

The variational problem is stated as a modification of Lagrange's form (3); i.e., it is required to find a stationary value of the integral

$$I = \int_{t_0}^{t_1} \left( \dot{\vartheta} + \sum_{i=1}^4 \lambda_i \varphi_i \right) dt + \int_0^{t_f - t_1} \left( \dot{\vartheta} + \sum_{i=1}^4 \lambda_i \varphi_i \right) d\tau$$
$$\tau = t - t_1$$

where the Lagrangian multipliers  $\lambda_i$  are time dependent and  $t_1$  represents the variable time at the end of the optimal coasting period. Note that the relationship  $\lambda_i \varphi_i = 0$  must be satisfied in this formulation. A necessary condition (proof of sufficiency is beyond the scope of this paper) for the existence of such a stationary value is that the first variation of I must vanish

$$\begin{split} \delta I &= [F^*(t)\delta t]_{t_0}^{t_1} + \int_{t_0}^{t_1} \delta F^*(t) dt \ + \\ & [F^*(\tau)\delta \tau]_o^{if-t_1} + \int_0^{t_f-t_1} \delta F^*(\tau) \ d\tau = 0 \end{split} \ [12]$$

where

$$F^*(t) = \dot{\chi}_1 + \sum_{i=1}^4 \lambda_i \varphi_i(\chi_k, \dot{\chi}_k, t)$$

wh

ger

of

mu

sar

Co

con of

pro

sta

Sion

froi

with the notation  $\chi_k$ , k = 1, 2, 3, 4 representing  $\vartheta$ ,  $\gamma$ , h and  $\alpha$ , respectively, being adopted for brevity. In the first integral of Equation [12] the trajectory comparisons are made at the same values of time. Hence

$$\delta F^*(t) = \sum_{k=1}^{4} \left[ \frac{\partial F^*}{\partial \chi_k} \left( \delta \chi_k - \dot{\chi}_k \delta t \right) + \frac{\partial F^*}{\partial \dot{\chi}_k} \frac{d}{dt} \left( \delta \chi_k - \dot{\chi}_k \delta t \right) \right] [13]$$

Furthermore

$$\int_{t_0}^{t_1} \frac{\partial F^*}{\partial \chi_k} \frac{d}{dt} (\delta \chi_k - \dot{\chi}_k \delta t) dt =$$

$$\left[ \frac{\partial F^*}{\partial \dot{\chi}_k} (\delta \chi_k - \dot{\chi}_k \delta t) \right]_{t_0}^{t_1} - \int_{t_0}^{t_1} (\delta \chi_k - \dot{\chi}_k \delta t) \frac{d}{dt} \left( \frac{\partial F^*}{\partial \dot{\chi}_k} \right) dt \quad [14]$$

In the second integral of Equation [12] the comparisons are made at the same values of  $\tau$ , and results corresponding to Equations [13 and 14] may be derived by replacing t with  $\tau$  in those equations. Substituting these results in Equation [12] yields the complete expression for the first variation

Integrating the Euler-Lagrange equations, [16] yields the expressions

$$\frac{\partial F^*}{\partial \dot{\chi}_k} = \int \frac{\partial F^*}{\partial \chi_k} dt + C \qquad k = 1, 2, 3$$
 [19]

where C is an integration constant. Since  $F^*$  is bounded and continuous within each stage of the trajectory, it follows that the values of  $\lambda_i(i=1,2,3)$  are continuous over the entire trajectory, including staging points.

The corner conditions yield no information about  $\alpha$  and  $\lambda_4$ . When the trajectory is not constrained by one of the  $L_m$  limits ( $\varphi_4 > 0$  and  $\lambda_4 = 0$ ), the fourth Euler-Lagrange equation of [17] shows that  $\alpha$  may be discontinuous at staging. This is the result of assuming the rocket to be a point mass without inertia and including aerodynamic forces in the analysis. Though an instantaneous jump in angle of attack is unrealistic, its effect on the overall trajectory is insignificant. When the trajectory is constrained by one of

$$\delta I = \left[ \left( F^* - \sum_{k=1}^4 \dot{\chi}_k \frac{\partial F^*}{\partial \dot{\chi}_k} \right) \delta t \right]_{t_0}^{t_1} + \left[ \sum_{k=1}^4 \frac{\partial F^*}{\partial \dot{\chi}_k} \delta \chi_k \right]_{t_0}^{t_1} + \left[ \left( F^* - \sum_{k=1}^4 \dot{\chi}_k \frac{\partial F^*}{\partial \dot{\chi}_k} \right) \delta \tau \right]_0^{t_f - t_1} + \left[ \sum_{k=1}^4 \frac{\partial F^*}{\partial \dot{\chi}_k} \delta \chi_k \right]_0^{t_f - t_1} + \sum_{k=1}^4 \left[ \int_{t_0}^{t_1} \left( \frac{\partial F^*}{\partial \chi_k} - \frac{d}{dt} \frac{\partial F^*}{\partial \dot{\chi}_k} \right) (\delta \chi_k - \dot{\chi}_k \delta t) dt + \int_0^{t_f - t_1} \left( \frac{\partial F^*}{\partial \chi_k} - \frac{d}{dt} \frac{\partial F^*}{\partial \dot{\chi}_k} \right) (\delta \chi_k - \dot{\chi}_k \delta \tau) d\tau \right] = 0 \quad [15]$$

Since the variations  $\delta\chi_k$  are arbitrary, application of the basic lemma of the calculus of variations yields

$$\frac{\partial F^*}{\partial \chi_k} - \frac{d}{dt} \frac{\partial F^*}{\partial \chi_k} = 0 \qquad k = 1, 2, 3, 4$$
 [16]

or, in terms of the physical variables

$$\begin{split} \dot{\lambda}_1 + \lambda_1 \frac{\partial F}{\partial \vartheta} + \lambda_2 \frac{\partial G}{\partial \vartheta} + \lambda_3 \sin \gamma - \lambda_4 \frac{\partial \varphi_4}{\partial \vartheta} &= 0 \\ \dot{\lambda}_2 + \lambda_1 \frac{\partial F}{\partial \gamma} + \lambda_2 \frac{\partial G}{\partial \gamma} + \lambda_3 \vartheta \cos \gamma - \lambda_4 \frac{\partial \varphi_4}{\partial \gamma} &= 0 \\ \dot{\lambda}_2 + \lambda_1 \frac{\partial F}{\partial h} + \lambda_2 \frac{\partial G}{\partial h} - \lambda_4 \frac{\partial \varphi_4}{\partial h} &= 0 \\ \lambda_1 \frac{\partial F}{\partial \alpha} + \lambda_2 \frac{\partial G}{\partial \alpha} - \lambda_4 \frac{\partial \varphi_4}{\partial \alpha} &= 0 \end{split}$$

These are the Euler-Lagrange equations for the problem, which make both integrals of Equation [15] vanish.

Inspection of Equations [17] reveals that they are homogeneous in the multipliers  $\lambda_i$ . This property, which was also noted by Cicala and Miele (6) and Breakwell (4), makes solutions of these equations independent of the initial values of one of the multipliers. In the present analysis,  $\lambda_1$  was the multiplier selected. The Euler-Lagrange equations retain the same form except that the multipliers and their time derivatives are replaced by

$$\lambda_i^* = \frac{\lambda_i}{\lambda_i}$$
  $\dot{\lambda}_i^* = \frac{\dot{\lambda}_i}{\lambda_i}$  [18]

The initial values  $\lambda_{10}$  are arbitrary.

### **Corner Conditions**

Staging points of the trajectory are characterized by discontinuities of arbitrary magnitude in the thrust and mass of the rocket. In the physical case (and in the variational problem) it is required that  $\vartheta$ ,  $\gamma$ , h and  $\dot{h}$  be continuous at staging, whereas  $\dot{\vartheta}$  and  $\dot{\gamma}$  may be discontinuous. Conclusions regarding some of the other parameters are deduced from the Erdmann-Weierstrass corner conditions.

the  $L_m$  limits ( $\varphi_4 = 0$  and  $\lambda_4 \neq 0$ ),  $\alpha$  may be either continuous or discontinuous at staging, depending on the form of control parameter  $l_m$  which is involved. The multiplier  $\lambda_4$  may also be discontinuous at staging. In view of these circumstances, the character of the trajectory may change at staging, i.e., from constrained to unconstrained.

### **End Conditions**

Satisfying the remainder of Equation [15] provides the required end conditions for the problem. Applying the corner conditions and noting that no initial variations are allowed, Equation [15] becomes

$$\left(F^* - \sum_{k=1}^4 \dot{\chi}_k \frac{\partial F^*}{\partial \dot{\chi}_k}\right)_{t=t_1} \delta t_c + \left(\sum_{k=1}^4 \frac{\partial F^*}{\partial \dot{\chi}_k} \delta \chi_k\right)_{t=t_f} = 0 \quad [20]$$

where  $t_{\varepsilon}$  is the total coasting time and  $\delta \tau = 0$ , since the burning times of the stages following the coasting period are specified. By definition,  $\lambda_{i}\varphi_{i}$  equals zero on trajectories, so Equation [20] may be written as

$$-(\lambda_1 \dot{\vartheta} + \lambda_2 \dot{\gamma} + \lambda_3 \dot{h})_{t=t_1} \delta t_t + \lambda_{1_f} \delta \vartheta_f + \lambda_{2_f} \delta \gamma_f + \lambda_{3_f} \delta h_f = 0$$
[21]

Final values of  $\gamma$  and h are specified by conditions [4], so  $\delta \gamma_f = \delta h_f = 0$ . Furthermore, on an extremal,  $\delta \vartheta_f$  is equal to zero, so Equation [21] reduces to

$$(\lambda_1 \dot{y} + \lambda_2 \dot{\gamma} + \lambda_3 \dot{h})_{t=t_1} = 0$$
 [22]

for extremals containing an optimal coasting period. Hence, Equations [4 and 22] define the desired extremal in this case. When such a coasting period is not included,  $\delta t_c$  of Equation [21] is also zero and the only conditions required are those given in [4]. In the latter case every trajectory computed is an extremal for the particular end conditions achieved.

### **Extremal Solutions**

In the preceding section the problem under consideration has been stated in terms of the initial conditions [3], the terminal conditions [4] (and [22], if desired) and the set of Equations [5, 6 and 17]. Thus, it is seen that the boundary value

problem involved has its boundary conditions applied both at the beginning and end of the trajectory. The Lagrangian multipliers provide, in effect, dummy initial conditions which permit the initiation of a given trajectory integration.

Consider the problem of finding an extremal which contains a coasting stage. In this case the appropriate equations of the set [5, 6 and 17] are solved, using the initial conditions [3] in conjunction with guessed values of  $\lambda_{20}^*$ ,  $\lambda_{20}^*$  and  $t_c$ , to determine a given trajectory. The desired extremal is found by iterating on the guessed values until the terminal conditions [4 and 22] are satisfied within prescribed tolerances. When a coasting stage is not included, the problem is handled in an analogous fashion, with  $t_c = 0$  and condition [22] eliminated. Methods used for trajectory integrations and iteration for the desired extremal are next described.

### **Trajectory Integrations**

All trajectory integrations are performed by means of the Runge-Kutta four point scheme for several dependent variables, using time as the independent variable and beginning with the given initial conditions. Trajectory segments which are computed fall into four categories: Unconstrained, constrained, mixed and initial.

Unconstrained trajectories are true variational paths which are not constrained by any of the  $L_m$  limits. In this case  $\lambda_i$  is equal to zero and the integration involves the simultaneous solution of equations, [5 and 17]. The angle of attack at any instant is calculated by an iterative solution of the last equation of [17].

Constrained trajectories are defined as those constrained by one of the prescribed  $L_m$  limits. The path is uniquely determined by the solution of Equations [5 and 6], with  $\alpha$ being determined from Equation [6], either directly or by iteration. The Euler-Lagrange equations, [17] are then solved independently, with  $\lambda_4 \neq 0$ , to determine the values of the Lagrangian multipliers.

Mixed trajectories have both unconstrained and constrained segments. Computations for these segments use the techniques noted, but special tests are required to accommodate entering and leaving a constrained segment. Locating the point where a trajectory first becomes constrained involves an interpolation to determine the time when Equation [6] becomes an equality. A similar interpolation is employed to determine the time when the trajectory leaves a constrained segment, except that  $\lambda_4 = 0$  must be satisfied in this instance. When more than one limit is imposed in a given problem these tests are coupled in a manner appropriate for selecting the most critical.

When the velocity is zero the set of equations involved in the proposed method becomes singular. Hence, for ground launched rockets, an initial, pre-programmed trajectory segment spanning the time interval  $0 \le t \le t_0$  must be computed by solving either  $\gamma = \gamma_0$ , or  $\gamma + \alpha = \text{constant}$ , together with Equations [5]. Lagrangian multipliers are not computed during this period, and the variational problem begins at  $t = t_0$ , with  $v_0 = v(t_0)$ ,  $\gamma_0 = \gamma(t_0)$  and  $h_0 = h(t_0)$ . The angle of attack will ordinarily be discontinuous at this time.

### Iteration Procedure

Use of an efficient iteration technique is mandatory for finding desired extremals with reasonable expenditures of computer time. The technique adopted for use with the proposed method was attributed by Montague (5) to Mark Robinson. To illustrate the adaptation of this technique, write the desired end conditions for an extremal with a coasting stage as

$$\xi = \Gamma - \gamma_f = 0$$
  $\eta = H - h_f = 0$   
 $\zeta = (\lambda_1 \vartheta + \lambda_2 \dot{\gamma} + \lambda_3 h)_{i=i_1} = 0$ 
[23]

The procedure begins with the computation of four trajectories having the following initial conditions and final results

$$\lambda_{2_0}^*, \lambda_{3_0}^*, t_c \to \xi_{l}, \eta_{l}, \zeta_{1}$$

$$\lambda_{2_0}^* + \Delta \lambda_{2_0}^*, \lambda_{3_0}^*, t_c \to \xi_{l}, \eta_{l}, \zeta_{2}$$

$$\lambda_{2_0}^*, \lambda_{3_0}^* + \Delta \lambda_{3_0}^*, t_c \to \xi_{l}, \eta_{l}, \zeta_{1}$$

$$\lambda_{2_0}^*, \lambda_{3_0}^*, t_c + \Delta t_c \to \xi_{l}, \eta_{l}, \zeta_{1}$$

The first of these trajectories defines the residuals produced by the guessed values of  $\lambda_{2_0}^*$ ,  $\lambda_{3_0}^*$  and  $t_c$ :  $R_1 = \xi_1$ ,  $R_2 = \eta_1$  and  $R_3 = \xi_1$ , and the subsequent three trajectories define the derivatives

ALTITUDE - FT. X 10-4

em

are

cien

In t

equa

Boo

The

rat

spe

bu

sta

JUL

$$\frac{\partial \xi}{\partial \lambda_{2_0}{}^*} = \frac{\xi_1 - \xi_1}{\Delta \lambda_{2_0}{}^*} \qquad \frac{\partial \eta}{\partial \lambda_{2_0}{}^*} = \frac{\eta_1 - \eta_1}{\Delta \lambda_{2_0}{}^*} \qquad \frac{\partial \zeta}{\partial \lambda_{2_0}{}^*} = \frac{\zeta_2 - \zeta}{\Delta \lambda_{2_0}{}^*}$$

etc. To find the desired extremal, it is necessary that all of the residuals vanish. For assumed linear variations between the initial and final conditions, this will be true if, in matrix notation

$$|A_{sr}| \left\{ \Delta p_r' \right\} = \left\{ -R_s(p_r) \right\} \quad r = 1, 2, 3 \quad s = 1, 2, 3 \quad [24]$$

where  $p_1$ ,  $p_2$  and  $p_{\bar{\epsilon}}$  are  $\lambda_{2_0}^*$ ,  $\lambda_{3_0}^*$  and  $t_{\epsilon}$ , respectively, and

$$|A_{sr}| = \begin{vmatrix} \frac{\partial \xi}{\partial \lambda_{2_0}^*} & \frac{\partial \xi}{\partial \lambda_{2_0}^*} & \frac{\partial \xi}{\partial t_c} \\ \frac{\partial \eta}{\partial \lambda_{2_0}^*} & \frac{\partial \eta}{\partial \lambda_{2_0}^*} & \frac{\partial \eta}{\partial t_c} \\ \frac{\partial \zeta}{\partial \lambda_{2_0}^*} & \frac{\partial \zeta}{\partial \lambda_{2_0}^*} & \frac{\partial \zeta}{\partial t_c} \end{vmatrix}$$

Solving Equations [24] yields the next approximations to the initial values

$$p_{r'} = p_r + \Delta p_{r'}$$

that are used to compute the fifth trajectory.

This procedure, which may be cycled to accomplish the complete iteration, has the disadvantage of requiring three redundant trajectory computations per correction. Such redundancy is avoided by using the matrix modification procedure suggested by Robinson. The modified matrix satisfies the relationship

$$|A_{sr} + \Delta A_{sr}| \left\{ \Delta p_{r'} \right\} = \left\{ R_{s}(p_{r'}) - R_{s}(p_{r}) \right\}$$
 [25]

where the  $\Delta A_{sr}$  represent modifications of the individual matrix elements, and the residuals  $R_s(p_{s'})$  are computed from results of the fifth trajectory. Subtracting Equation [25] from [24] yields

$$|\Delta A_{sr}| \left\{ \Delta p_r' \right\} = \left\{ R_s(p_r') \right\}$$

which has a solution (non-unique) of the form

$$\Delta A_{sr} = [R_s(p_r')] \Delta p_r' / \sum_{r=1}^{3} (\Delta p_r')^2$$

The next corrections are

$$\Delta p_{r}'' = |A_{sr} + \Delta A_{sr}|^{-1} \left\{ -R_{s}(p_{r}') \right\}$$

and the next approximations to the initial values are

$$p_{r''} = p_{r'} + \Delta p_{r''}$$

Subsequent approximations are computed in an analogous manner, with one trajectory integration per correction. The same iteration technique, with appropriate reduction to two parameters, is used for finding extremals that do not have coasting periods.

### **Numerical Results**

The method previously described was coded on an IBM 704 computer at Convair-Fort Worth and is now being used in design studies. To confirm the analytical formulation

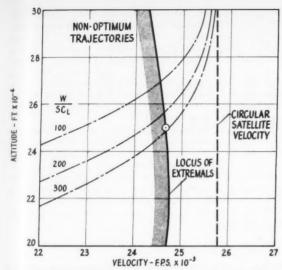


Fig. 2 Extremum selection for boost-glide vehicle launching,  $\Gamma = \mathbf{0}, \, W_p = \mathbf{4000} \, \mathbf{lb}$ 

employed, numerical results for two hypothetical missions are presented and analyzed below. In these calculations the mass flow rate and thrust were represented by

$$\dot{m} = -(1/c)(T_R + A_{ex}P_R)$$
 [26]

and

$$T = T_R + A_{ex}(P_R - P) \tag{27}$$

where

 $T_R$  = rated thrust (may be time variant) at an altitude having the ambient pressure  $P_R$ 

Acz = nozzle exit area

e = effective exhaust velocity

P = ambient pressure at the operating altitude

The general representations used for the lift and drag coefficients are

$$C_L = (C_{L_{\alpha}} + K \mid \sin \alpha \mid) \sin \alpha$$
 [28]

$$C_D = C_{D_0} + C_L \sin \alpha \tag{29}$$

In the examples next discussed, K=0. The particular forms [28 and 29] were selected to make the fourth Euler-Lagrange equation of [17] be continuous for all  $\alpha$  values.

### **Boost Rocket**

Two missions were selected for the illustrative examples. These consist of launching a hypersonic glider and a satellite, each weighing 4000 lb from the surface of Earth. Characteristics of the boost rockets employed are given in Table 1.

	Table 1	Boo	st rockets	
	Stage	1	Stage 2	Stage 3
rated thrust,				
$lb \times 10^{-8}$	840, sea	lev.	140, vacuum	15.12, vacuum
specific impulse,				
sec	250, sea	lev.	280, vacuum	280, vacuum
burning time, sec	60		60	60
stage weight,				
$1b \times 10^{-3}$	219.1		32.6	3.6
propellant weight,				
lb × 10 <sup>-3</sup>	201.6		30.0	3.24
nozzle exit area, ft2	25		4	

These hypothetical vehicles are representative of current solid rocket technology. Stages 1 and 2 were sized to accommodate the boost-glide mission, and stage 3 was subsequently added to achieve a low satellite orbit. In the examples, the rated thrust was assumed constant and realistic values of the lift and drag coefficients were employed in conjunction with the ARDC 1956 atmosphere model.

### Trajectory Selection

Selection of the desired boost trajectories simply consists of matching the booster capability with the general mission requirements. Fig. 2 illustrates the mode of trajectory selection employed for the launching of a hypersonic glider. The broken lines in this figure represent equilibrium glide paths computed by specifying  $\dot{\gamma} = 0$  in the second equation of [1]. The two-stage booster capability, labeled the locus of extremals, was computed by specifying  $\Gamma = 0$  and several burnout altitudes, with the initial pitch point arbitrarily set at 10 sec. Some difficulty was encountered in ascertaining suitable values of  $\lambda_{20}^{*}$  and  $\lambda_{30}^{*}$  to achieve convergence to the desired extremal in these calculations. This difficulty was attributed to the sensitivity of the trajectories to the initial values of the Lagrangian multipliers, caused by specifying burnout altitudes in regions where the aerodynamic forces are significant.

One of the computed trajectories has the time history indicated in Fig. 3. End conditions of this trajectory are indicated by the circled point of Fig. 2, having h=250,000 ft, v=24,653 fps and  $W/SC_L=288$ . The relatively short burning time of the rocket caused considerable turning throughout the entire trajectory.

Trajectory selection for the satellite launch example is illustrated in Fig. 4. In this instance the required conditions are given by the circular satellite velocity relationship

$$\vartheta_f = \sqrt{g_f(R + h_f)}$$

where the values of R and the sea-level acceleration of gravity were those of the ARDC 1956 atmosphere model. The locus of extremals was computed for  $\Gamma=0$  and several values of H, with the coasting time optimization included. In this case no convergence difficulties were encountered, with the

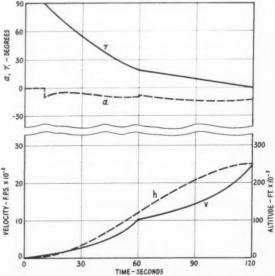


Fig. 3 Time history of selected extremal for boost-glide vehicle launching

desired extremal being found after an average of 12 trajectory integrations, a small number for a three-parameter iteration.

The intersection of the circular satellite velocity line with

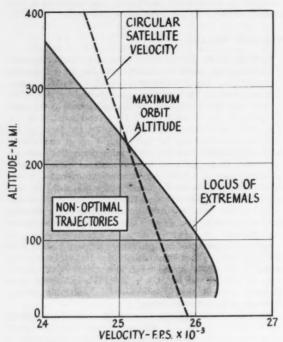
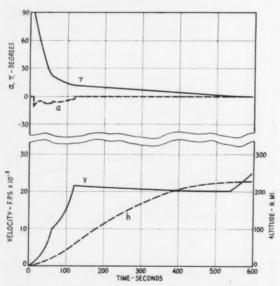


Fig. 4 Extremum selection for satellite launching,  $\Gamma = 0$ ,  $W_p =$ 4000 lb



Time history of extremal for satellite launching

the locus of extremals represents the maximum orbit altitude attainable (227 nautical miles) with the particular rocketpayload configuration assumed. Fig. 5 shows the time history of the maximum orbit altitude trajectory, having an optimum coasting time of 416 sec. This figure indicates that the gravity turn program, highly touted for liquid rockets, is hardly optimum for solid rockets of the type assumed in this example. The short burning time of the first two stages does not permit sufficient gravity turning prior to

Both of the trajectories indicated in Figs. 3 and 5 could be closely simulated by realistic guidance and control programs. For example, three constant attitude angle rates  $(\dot{\gamma} + \dot{\alpha})$ , one in each powered stage, would yield very nearly the same burnout conditions. Losses in final velocity caused by approximating the optimum control program will be small since the optimization technique requires that the derivative of final velocity with respect to instantaneous angle of attack be equal to zero.

### **Summary of Results**

An evaluation of the numerical results shown is summarized in Table 2, where the ideal velocity-velocity losses caused by gravity, turning and drag-and fraction of ideal velocity attained are shown, respectively, from left to right. Ideal velocities shown include the effects of thrust variations caused by ambient pressure changes along the respective trajectory. The high percentages of ideal velocity obtained substantiate the validity and utility of the method.

Table 2 Evaluation of numerical results

					cent
	Did	$\Delta \vartheta_g$	$\Delta \vartheta_{\alpha}$	$\Lambda \vartheta D$	Did
Glider laun	ching				
stage 1	13,085	-1,458	-125	-1,345	77.6
stage 2	15,430	-314	-415	-205	94.0
mission	28,515	-1,772	-540	-1,550	86.5
Satellite lau	nching				
stage 1	12,655	-1,464	-80	-1,275	77.7
stage 2	12,350	-527	-30	-80	94.8
coast		-1,463			
stage 3	5,005	-1			100.0
mission	30,010	-3,455	-110	-1,355	$83.6^a$

a Including coast stage loss.

### References

1 Liebhold, E. M. and Brown, R. R., "Application of the Calculus of Variations to Guided Missile Flight Paths for Obtaining Maximum Range," Rand Corp., Los Angeles, Calif., R-138, Feb. 1949.

2 Leitmann, G., "Trajectory Programming for Maximum Range," Franklin Institute J., vol. 284, Dec. 1957, pp. 443-452.

3 Bliss, G. A., "Lectures on the Calculus of Variations," first ed., University of Chicago Press, Chicago, 1946, chaps. 1 and 7.

4 Breakwell, J. V., "The Optimization of Trajectories," J. Soc. Ind. Appl. Math., vol. 7, no. 2, June 1959, pp. 215-247.

5 Montague, H. B., "Integration Technique for Stagnation Point Heat Transfer Problems," Bumblebee Aerodynamics Panel—Minutes of 40th Meeting, vol. 1, APL/JHU, May 1959.

6 Cicala, C. and Miele, A., "Brachistochronic Maneuvers of a Variable Mass Aircraft in a Vertical Plane," J. Aeron. Sci., vol. 22, no. 8, Aug. 1955, pp. 577-578.

tere

tict effe

sho the gas dep suc

erti tha and diss cal

mee pro of k

one

pro

dyn tres

kine and thro sho of t to e all kno

pra

tech

JUL

Per

# **Oblique Shock Relations for** Air at Mach 7.8 and 7200 R Stagnation Temperature

H. T. NAGAMATSU.2 J. B. WORKMAN<sup>3</sup> and R. E. SHEER Jr.4

Research Laboratory, General Electric Co. Schenectady, N. Y.

Oblique shock relations for dissociated air in thermodynamic equilibrium have been calculated for a free stream flow Mach number of 7.8 in the test section with an equilibrium stagnation temperature of 7200 R in the reservoir. The results for the density, pressure and temperature ratios, and flow deflection across the shock wave are presented as functions of the shock wave angle. Complete equilibrium has been assumed in the calculations, utilizing the best available thermodynamic properties of air for the region considered. The real gas oblique shock relations have been experimentally verified by testing an adjustable two-dimensional wedge model in a hypersonic shock tunnel. Correlations of the calculated and experimental pressure ratios and shock wave angles are presented as functions of flow deflection angle. When allowance was made for the boundary layer displacement effect, the correlation was seen to be good. The reservoir conditions were selected to insure that the flow in the shock tunnel would be close to equilibrium.

THE ADVENT of missiles and space vehicles traveling at hypersonic flight speeds has recently stimulated much interest in the shock waves produced by such bodies. In particular, there has been considerable discussion of the "real gas effects" in the air immediately behind high Mach number shock waves. By "real gas effects" is meant the departure of the thermodynamic properties of the medium from a perfect gas with a constant specific heat ratio of 1.4. Although air departs from this perfect gas model at temperatures as low as 540 R, this concept has been used with considerable success in the past for analyzing low Mach number shock properties. However, at any flow condition even approaching that under consideration here, this model must be abandoned and, instead, the actual thermodynamic properties of air used.

As soon as shock waves strong enough to excite vibration, dissociation or ionization and strong enough to produce chemical reactions are considered, the reaction rate question immediately comes to the forefront. In dealing with shock processes wherein a gas is required to absorb large quantities of kinetic energy as internal energy virtually instantaneously, one must be concerned not only with the final thermodynamic properties, but also with the time needed to achieve thermodynamic equilibrium. A rigorous analytical method for treating the shock problem would be to set up a careful kinetic theory model of the gas molecules with reaction rates, and then to analyze exactly what happens as the flow proceeds through the momentum and energy readjustments at the shock region. Unfortunately, there is insufficient knowledge of the properties and reaction rates of air at the present time to employ such a method. It is conceivable also that even if all of the rate constants and interaction parameters were known, the complexity of the calculation would prevent a practical solution.

Recently (1,2)<sup>5</sup> shock relations for air under the assumption of instantaneous thermodynamic equilibrium downstream of the shock wave for two-dimensional conditions have been calculated. But, only a negligible amount of experimental data is available to correlate with these calculations. This paper presents the oblique shock relations for the assumption of thermodynamic equilibrium downstream of the shock wave, using the high temperature thermodynamic properties of air given in (3 and 4). The calculated shock wave angles and surface pressures are compared with the experimental data obtained in a hypersonic shock tunnel (5) on an adjustable wedge model.

### Analysis of Oblique Shock Relations in Real Gas

The thermodynamic properties of air across the range of shock wave angles have been calculated using a procedure similar to that discussed by Moeckel (1) and others. The basic concepts of conservation of mass, momentum and energy were applied assuming the fluid to be a continuum, inviscid and always in thermodynamic equilibrium. If it is assumed that equilibrium is attained immediately behind the shock wave, the wave may be assumed to be infinitely thin for purposes of analysis. In solving for the conditions after the oblique shock wave, the available references on equilibrium thermodynamic properties for air were utilized. For temperatures above 3600 R the information presented by Feldman (3) was employed; from 540 to 3600 R, Hirschfelder and Curtiss (4). Below 540 R the air was assumed to be a perfect gas with a specific heat ratio of 1.4.

The oblique shock wave relations for air in thermodynamic equilibrium were calculated for the following free stream condition: A flow Mach number of 7.8, ambient temperature of 810 R, static pressure of 0.0206 psia, and stagnation temperature after a normal shock wave of 6070 R. These values were obtained in the test section of a hypersonic shock tunnel (6) with a reservoir equilibrium stagnation temperature of 7200 R, a pressure of 500 psi and a nozzle area ratio of 576.

Received June 4, 1959.

<sup>&</sup>lt;sup>1</sup> This work was supported in part by the Ballistic Missile Division of the U. S. Air Force under Contract AF 04-647-269.

<sup>2</sup> Research Associate; also Adjunct Professor, Rensselaer Polytechnic Institute. Member ARS.

Presently attending Princeton University. <sup>4</sup> Gas Dynamics Division.

<sup>&</sup>lt;sup>5</sup> Numbers in parentheses indicate References at end of paper.

For this particular test condition, both static and impact pressures were measured along the axis of the conical nozzle. The results agreed very closely with the calculated values obtained assuming equilibrium during the expansion process.

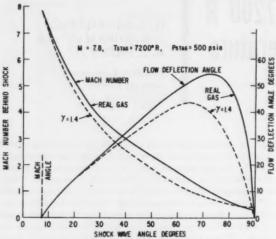


Fig. 1 Calculated Mach number behind shock and flow deflection angle vs. shock wave angle

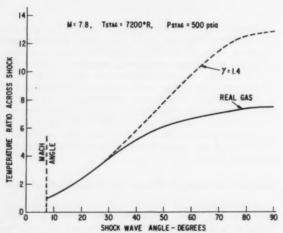


Fig. 2 Calculated temperature ratio across shock vs. shock wave angle

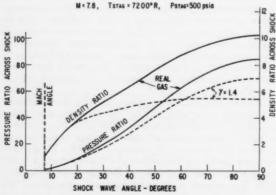


Fig. 3 Calculated pressure ratio and density ratio across shock vs. shock wave angle

The relation between the flow deflection angle across the shock wave  $\theta$  and the shock wave angle  $\beta$  is shown in Fig. 1 for these initial conditions. For shock wave angles greater than 30 deg the flow deflection for  $\gamma=1.4$  is much less than that for the real gas. The maximum flow deflection angle at detachment is 54.5 deg for the present case, whereas for a constant specific heat ratio of 1.4 and a flow Mach number of 7.8 the deflection angle is only 43.5 deg. This large difference in the flow deflection angle is caused by the increase in the density ratio across the shock wave and by the decrease in the ratio of specific heats which occurs at these elevated temperatures.

ps:

M

th

fac

Th

loc

ob

sys

sir

the

col

1186

ori

Th

tit

the

hy

en

to

Th

an

th

dat

Op

the

nu

eva

are

to

ten

Th

cui

64-

ter

kne

dri

car

tio

rar

tio

bas

wa

tur

cor

the

sio

Ju

For the same upstream flow Mach number of 7.8, the flow Mach number after the shock wave is always less for the  $\gamma=1.4$  case than for the real gas case, up to a nearly normal shock wave as indicated in Fig. 1. It is also apparent from this figure that for a Mach number of unity the shock wave angle, after the shock, has increased from 65 to 72.5 deg. Thus, with a detached shock wave for a symmetrical blunt body at hypersonic flight conditions, the sonic point on the shock wave wave from  $\gamma=1.4$ . The flow Mach number after a normal shock wave,  $\beta=90$  deg, decreases from 0.39 to 0.30 owing to the real gas effects.

In Fig. 2 the temperature downstream of the shock is shown as a function of the shock wave angle for both  $\gamma = 1.4$ and the real gas conditions. For the same flow Mach number, the perfect gas temperatures are higher than those for the real gas flow. Because of the energy absorbed in dissociation, chemical formation and ionization, the equilibrium temperature is lower. The greatest temperature difference between the two cases occurs when the shock wave is normal to the free stream flow. For an infinitesimal disturbance in the free stream condition, with the shock wave angle equal to the Mach angle, the temperature ratio for both cases is the same, since there is no real gas effect. But as the shock wave angle becomes greater, corresponding to a stronger shock, the temperature after the shock increases and the real gas effect becomes greater. Thus, with an adjustable wedge it is possible to have the free stream condition ahead of the shock wave to be that of a perfect gas, and after the shock wave to control the degree of real gas effect by adjusting the flow deflection of

the wedge angle. The pressure and density ratios are shown in Fig. 3 as functions of the shock wave angle for both the perfect gas, y 1.4, and the real gas case. The real gas effects increased the pressure after the strong shock waves. This corresponds to large shock wave angles, as indicated in the figure. It is evident from these results that the density ratio has the greatest effect upon the flow parameter due to the real gas effects. For a normal shock wave,  $\gamma = 1.4$  and infinite flow Mach number, the limiting density ratio is 6. In the present calculation with a free stream temperature of 810 R and a flow Mach number of 7.8, the density ratio across the normal shock wave is 10.25, as shown in Fig. 3. This larger density ratio causes the shock wave to move closer to the wedge surface as indicated in Fig. 1, and causes the detached shock wave for a blunt body to move closer to the body surface (6).

### **Experimental Procedure**

### Hypersonic Shock Tunnel

It is possible to check the calculations for the oblique shock wave for thermodynamic equilibrium, discussed in the previous section, by using a two-dimensional wedge model in a hypersonic shock tunnel. A detailed description of this research equipment for producing hypersonic flows in the 24-in. diam test section at high stagnation temperatures is presented in (5). The free stream conditions in the test section for which the calculations were made correspond to a reservoir equilibrium stagnation temperature of 7200 R at a pressure of 500

psi just ahead of the entrance to the hypersonic nozzle. Previously it has been shown (6) that such a flow will be close to equilibrium conditions when expanded in the nozzle. It was for this reason that these particular upstream conditions were selected.

### **Model and Instrumentation**

An adjustable, 60-deg included angle, wedge model with three pressure orifices on both surfaces was used in the investigation. Wedge angles of 50 and 10 deg, 45 and 15 deg, 40 and 20 deg, or 30 and 30 deg may be tested to obtain surface pressure for two different flow deflections at one time. The span of the model was 5 in. with the pressure orifices located near the center of the model.

The Schlieren photograph (Fig. 4) of the shock wave was obtained with a single pass symmetrically arranged Schlieren system with a short duration condenser discharge spark for the light source. A delay circuit was used in conjunction with the Schlieren system to obtain Schlieren photographs at any desired time after the establishment of the flow.

Piezoelectric barium-titanate gages were used to measure the surface pressure on the wedge. These were specifically constructed at the General Electric Research Laboratory for use in fundamental hypersonic research investigations. An orifice diameter of  $\frac{1}{16}$  in. was used to measure the pressure. This small diameter was adequate for the small barium-titanate gages.

All the pressure gages were installed in the wedge model and then calibrated at the end of the shock tube portion of the hypersonic shock tunnel. A weak wave reflected from the end of the tube where the wedge model was installed was used to produce the increment in pressure for calibrating the gages. The shock Mach number for these calibration tests was about 1.5, at which the agreement between the experimentally and analytically predicted pressures is quite good. It was found that the pressure gages must be dynamically calibrated in the model in order to obtain consistent and reliable pressure data in the hypersonic shock tunnel.

### **Operating Procedure**

The model was then installed on the sting and positioned in the test section of the shock tunnel (see Fig. 4). The aluminum diaphragm at the entrance to the conical nozzle was installed, after which the dump tank housing the nozzle exit was evacuated to about 25  $\mu$  of mercury pressure. For a nozzle area ratio of 576, this dump tank pressure was low enough to minimize the strength of the starting shock wave.

By adjusting the initial pressures in the driver and in the driven tube, the desired reflected pressures and stagnation temperatures at the end of the driven tube can be produced. The shock wave velocity is determined at 12 stations along the driven tube. At the end of the driven tube, a more accurate measurement of the shock velocity is made over a  $6\frac{1}{4}$ -ft distance by means of a Berkeley counter. Thus, by determining the shock Mach number at the end of the tube and knowing the initial pressure and temperature of the air in the driven tube, the reflected equilibrium stagnation temperature can be calculated by using available thermodynamic information for air (7,8). It is assumed that equilibrium is attained rapidly after the shock wave. At high pressures the assumption of equilibrium after the reflected wave seems to be valid, based on recent results. The pressure after the reflected wave was measured with two pressure gages installed very close to the entrance of the conical nozzle. These reflected temperatures and pressures constitute the reservoir conditions for the convergent-divergent conical nozzle.

Using these reservoir conditions, it is possible to calculate the pressure and temperature in the nozzle, assuming that the flow is always in equilibrium and isentropic during the expansion process. For a reflected pressure of 500 psi and an

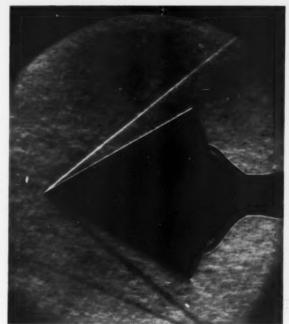


Fig. 4 Schlieren photograph of adjustable wedge at 30 and 30 deg angles from centerline

equilibrium stagnation temperature of 7200 R the static and impact pressure along the centerline of the nozzle agreed very well with the value calculated for an equilibrium isentropic expansion (6). Thus, the initial free stream conditions assumed in the oblique shock wave calculations were actually the same as the results obtained for this nozzle. For the present investigation, the shock tunnel was operated with these reservoir conditions to obtain the oblique shock wave angle and wedge surface pressure as functions of flow deflection.

### Results

### **Shock Wave Angle**

For wedge angles less than 15 deg, measured from the free stream direction, the boundary layer becomes very thick because of the low pressure downstream of the shock wave. In this case the outer edge of the boundary layer was displaced approximately 2.3 deg from the wedge surface. At lower wedge angles the flow deflection caused by the viscous effects becomes very large. For the wedge surface parallel to the free stream direction, the flow deflection may be as large as 9 deg. This is due entirely to viscosity as determined from the shock wave experiments with a flat plate (9). A detailed discussion of these experiments along with the associated theory for the slip phenomena and the strong shock waveboundary layer interaction is presented in (9 and 10).

Since the flow deflection due to viscous effects is large for the range of 0- to 10-deg wedge deflection, no pressure information was obtained with the present wedge model. A flat plate model with pressure gages and with an adjustable angle of attack will be used to investigate the shock wave-boundary layer interaction at small flow deflections. In this case, the boundary layer displacement angle is the same order of magnitude as the surface deflection. To minimize these effects, the present wedge shock wave angles and surface pressures were obtained for wedge angles in the range 15 to 45 deg. The maximum angle was limited by the shock wave becoming curved as the flow detachment angle was approached for real gas conditions (Figs. 1 and 5).

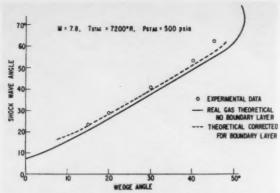


Fig. 5 Comparison of experimental and theoretical shock wave angle as function of wedge angle

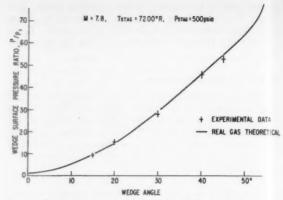
The shock wave angles in Fig. 5 were determined from the Schlieren photographs (Fig. 4) and are plotted as a function of the wedge angle without any boundary layer correction. For all wedge angles the shock wave angles are greater than those calculated for the real gas case as shown in Fig. 5. If the wedge angle is corrected by the boundary layer displacement angle as estimated from the Schlieren results, the real gas theoretical shock wave angle approaches the observed shock wave angle as indicated in Fig. 5. The corrected results agree very well for the lower wedge angles, but become slightly lower at the higher wedge angles. It is evident by comparing the perfect gas case  $\gamma = 1.4$ , presented in Fig. 1, with the observed shock angles, that the real gas effects decrease the shock angle for a given flow deflection. The angle for flow detachment is increased. Thus for the present test condition the assumption of flow being in thermodynamic equilibrium before and downstream of the shock wave is a reasonable one based upon the shock wave angle corrected approximately for the boundary layer displacement.

Further investigations will be conducted to obtain shock wave and pressure information in the flow deflection range from 45 to approximately 54 deg, using symmetrical wedge models. With the present wedge model, it was not possible to obtain reliable results in the vicinity of the shock wave detachment angle because of the unsymmetrical shape. For a flow Mach number of 7.8 at the test conditions, the flow deflection angle for shock detachment was approximately 43.5 deg for  $\gamma=1.4$ , and 54.5 deg for the real gas (Fig. 1). The observed shock wave angles in Fig. 5 indicate this delay in the detachment flow angle.

### Wedge Surface Pressure

The experimental wedge surface pressure ratios were obtained in conjunction with the shock wave angles and under the same free stream condition. Corresponding to this free stream condition in the test section, the equilibrium stagnation temperature behind a normal shock wave was 6070 R. This stagnation temperature in the test section was lower than the 7200-R stagnation temperature at the entrance to the nozzle because of the shock wave in the real gas. The departure from a perfect gas in the test section was caused by the low pressure at high temperature.

In Fig. 6 the wedge surface pressure ratio (surface pressure divided by the free stream pressure) for a wedge angle range of 15 to 45 deg is presented as a function of the wedge angle. The theoretical real gas pressure ratios were calculated by assuming the flow to be in equilibrium ahead and down-



tl

H

Fig. 6 Comparison of experimental and theoretical pressure ratio as function of wedge angle

stream of the oblique shock wave and using the thermodynamic data for air presented in (3 and 4). The calculations were made assuming the flow to be inviscid; that is, the boundary layer on the wedge surface was neglected. The vertical bars for the pressure ratios indicate the approximate range of the pressure measured by the gages for a given wedge angle.

The agreement between theoretical and experimental pressure results is quite satisfactory for the wedge angles considered (Fig. 6). The agreement is approximately within the experimental scatter of the pressure gages. At a wedge angle of 43.5 deg, the shock wave will be detached for the case of perfect gas with  $\gamma=1.4$ , as indicated in Fig. 3. For this condition the pressures on the wedge will be close to the normal shock pressure ratio of 70. But, due to the real gas effects, the shock wave is attached at a 45-deg wedge deflection angle, and the surface pressure ratio is approximately 53. Thus for this moderately high stagnation temperature in the test section, the real gas effect upon the wedge surface pressure was appreciable for a large flow deflection.

### Conclusions

It has been possible to measure the surface pressure for a wedge at several angles of attack for high stagnation temperature by the use of barium-titanate pressure gages.

The experimentally observed shock wave angles agreed with the theoretical values by assuming the flow to be in thermodynamic equilibrium ahead and downstream of the shock wave for a stagnation temperature of 6070 R after a normal shock wave and flow Mach number of 7.8.

At low wedge angles the flow deflection caused by the boundary layer was appreciable, and, consequently, the actual shock wave angle was much greater than the calculated inviscid value.

The real gas effects delayed the flow deflection angle at which the shock wave becomes detached from 43.5 deg for a perfect gas with  $\gamma = 1.4$  to approximately 54.5 deg.

The observed experimental surface pressure ratio agreed very closely with the theoretical results for equilibrium flow conditions. The pressure ratios at the large wedge deflection angles were appreciably less than that for the perfect gas  $\gamma=1.4$  result.

### Acknowledgments

Mr. C. H. Hunt assisted in the operation and reduction of

a o to o rette to

J

the data and Miss Ann Warner performed the calculation for the oblique shock relations. Messrs. L. A. Osburg and K. H. Carv assisted with the design of the model and the instrumentation.

#### References

- 1 Moeckel, W. E., "Oblique Shock Relations at Hypersonic Speeds for Air in Chemical Equilibrium," NACA TN 3895, Jan. 1957.
  2 Romig, M. F., "The Normal Shock Properties of Air in Dissociated Equilibrium," J. Aeron. Sci., vol. 23, no. 2, Feb. 1956, pp. 185-186.
  3 Feldman, S., "Hypersonic Gas Dynamic Charts for Equilibrium Air," Avco Research Lab. Rep., Jan. 1957.

- 4 Hirschfelder, J. and Curtiss, C., "Thermodynamic Properties of Air II," Univ. of Wisconsin, Rep. CM-518, Dec. 1948.
  5 Nagamatsu, H. T., Geiger, R. E. and Sheer, R. E., Jr., "Hypersonic Shock Tunnel," ARS JOURNAL, vol. 29, no. 5, May 1959, pp. 332-340.
  6 Nagamatsu, H. T., Geiger, R. E. and Sheer, R. E., Jr., "Real Gas Effects in Flow Over a Blunt Body at Hypersonic Speeds." J. Aero/Space Sci., vol. 27, no. 4, April 1960, pp. 241-251.
  7 Gilmore, F. R., "Equilibrium Composition and Thermodynamic Properties of Air at 24,000° K," Rand Rep. RM-1543, Aug. 1955.
  8 Hilsenrath, J. and Beckett, C. W., "Tables of Thermodynamic Properties of Argon-Free Air to 15,000° K," Arnold Engng. Dev. Ctr., TN 56-12, Sept. 1956.

- 9 Nagamatsu, H. T. and Sheer, R. E., Jr., "Hypersonic Shock Wave-Boundary Layer Interaction and Leading Edge Slip," ARS JOURNAL, vol. 30,
- no. 5, May 1960, pp. 454-462.

  10 Nagamatsu, H. T. and Li, T. Y., "On Hypersonic Flow Near the Leading Edge of a Flat Plate," Phys. Fluids, vol. 3, no. 1, Jan.-Feb. 1960

# Effect on a Rocket of the Oblateness of a Planet

WILLIAM A. ALLEN<sup>1</sup>

U. S. Naval Ordnance Test Station China Lake, Calif.

An approximation technique is used to solve the mathematical problem of a rocket moving radially away from a planet. The acceleration of the rocket is given by the relation  $\partial^2 r/\partial t^2$  + g(r) = c, where c is a constant and g(r) is the radial acceleration due to gravity at the distance r measured from the center of the planet. The planet is characterized by a gravitational potential that includes effects of its oblateness. A first integral, relating velocity and distance, is obtained immediately; a second integral, relating time and distance, is obtained by a quadrature. This second relation is expressible approximately in terms of elliptic integrals reducible to elementary types that have been tabulated. Inclusive of second-order terms the solution has been carried through completely, and the inclusion of fourth-order terms has been indicated. The approximate results are compared with the exact values obtained by numerical integration. Evaluation of a numerical example indicates that the solution inclusive of second-order terms is equivalent to the exact solution, and that the fourth- and other higher-order terms are negligible for the case of a rocket leaving Earth with an acceleration about 10 times that due to gravity.

PAPER has appeared (1)2 in which the problem was solved of a rocket that starts from rest, moves radially away from a planet and recedes to infinity against a force of gravity which diminishes as the inverse square of the distance measured from the center of the planet. The motion of the rocket at a given distance r was determined by the requirement that its acceleration relative to the planet, plus the acceleration due to gravity at that distance, was equal to a constant value c. Thus, an accelerometer within the rocket would always record this constant value c; there would be no rate of change of radial acceleration within the rocket.

The purpose of the present paper is to generalize the previous results to the case where the external gravitational potential of the planet can be characterized by the relation (2)

$$U(r,\,\theta)\,=\,-ga\left[\left(\frac{a}{r}\right)\,-\,\left(\frac{2}{3}\right)P_2J\left(\frac{a}{r}\right)^3\,+\,\left(\frac{8}{35}\right)P_4D\left(\frac{a}{r}\right)^6\right] \endaligned \endalig$$

where  $P_2 \equiv P_2(\cos \theta)$  and  $P_4 \equiv P_4(\cos \theta)$  are the even Legendre polynomials defined by the relations

$$P_2(\cos\theta) = (1/2)(3\cos^2\theta - 1)$$
 [2]

$$P_4(\cos\theta) = (1/8)(35\cos^4\theta - 30\cos^2\theta + 3)$$
 [3]

The quantity r in Equation [1] is distance measured from

Received March 9, 1959.

Head, Plasma Physics Branch, Michelson Laboratory <sup>2</sup> Numbers in parentheses indicate References at end of paper.

**JULY 1960** 

the center of the planet;  $\theta$  is the co-latitude; g is a constant that specifies the acceleration due to gravity at the distance a if the mass of the planet were concentrated at, or were arranged symmetrically about, its center. The radius of such a hypothetical planet must be less than or equal to a. In the case of an oblate planet, the quantity a is the equatorial radius, and the two quantities J and D are coupling constants fitted to gravitational measurements on the surface of the planet. Equation [1] has the general form that applies for a homogeneous oblate ellipsoid (3). Most planets can be considered, as a first approximation, to be homogeneous oblate ellipsoids (4). Equation [1] has been used in recent papers to describe the effect of the oblateness of Earth on a near satellite (5,6,7).

# Mathematical Formulation and Solution of the Problem

The problem reduces to the solution of the partial differential equation

$$\ddot{r} + \partial U/\partial r = c ag{4}$$

The dots in Equation [4] signify differentiation with respect to time. Substitute Equation [1] into Equation [4], and make the substitutions  $s \equiv r/a$ ,  $k^2 \equiv g/c$ , to obtain the acceleration of the rocket relative to the planet; this acceleration can be expressed by the relation

$$\ddot{s} = ca^{-1} \left\{ 1 - k^2 \left[ s^{-2} - 2P_2 J s^{-4} + (8/7) P_4 D s^{-4} \right] \right\}$$
 [5]

Note that  $\dot{s} \equiv \dot{r}/a$  and  $\ddot{s} \equiv \ddot{r}/a$ . Integrate Equation [5], and introduce the boundary condition  $\dot{s} = 0$  when s = 1 to obtain the velocity of the rocket relative to the planet; this velocity

Equation [7] is an improper integral. Integrate by parts to transform Equation [7] into the expression

$$t = \left(\frac{2a}{c}\right)^{1/2} \left( \left[ \frac{s(s-1)}{s-k^2(1+M)} \right]^{1/2} + \frac{k^2}{2} \int_1^s \frac{s(s-1)^{1/2} (1+N) ds}{\left\{ s[s-k^2(1+M)] \right\}^{1/2}} \right) [9]$$

The quantity N in Equation [9] is specified by the relation

$$N = - (2/3) P_2 J (1 + 2s^{-1} + 3s^{-2}) + (8/35) P_4 D (1 + 2s^{-1} + 3s^{-2} + 4s^{-3} + 5s^{-4})$$
[10]

Equations [5, 6 and 9] constitute a rigorous formal solution of the problem. The integral of Equation [9], however, must be evaluated by numerical methods.

A perturbation technique will now be applied to obtain an approximate analytical solution of Equation [7] The quantities J and D in Equation [8] are small for most planets in comparison with unity; therefore M is small in comparison with unity, and the quantity in square brackets in Equation [7] can be expanded by means of the binomial theorem. Equation [7] can be approximated by the relation

$$t = \left(\frac{2a}{c}\right)^{1/2} \int_{1}^{s} \frac{1}{[1 + (1/2)k^{2}(s - k^{2})^{-1}M + (1/2)(3/4)k^{4}(s - k^{2})^{-2}M^{2} + \dots] s ds}{[4s(s - 1)(s - k^{2})]^{1/2}}$$
[11]

Substitute the value of M from Equation [8] into Equation [11] and collect terms to obtain the relation

$$t = \left(\frac{2a}{c}\right)^{1/2} \left\{ \int_{1}^{s} \frac{sds}{[4s(s-1)(s-k^{2})]^{1/2}} + k^{2} \left( -\frac{1}{3} P_{2}J + \frac{4}{35} P_{4}D \right) \int_{1}^{s} \frac{(1+s^{-1}+s^{-2})sds}{(s-k^{2})[4s(s-1)(s-k^{2})]^{1/2}} + \frac{4}{35} k^{2}P_{4}D \int_{1}^{s} \frac{(s^{-3}+s^{-4})sds}{(s-k^{2})[4s(s-1)(s-k^{2})]^{1/2}} + \frac{1}{6} k^{4}P_{2}^{2}J^{2} \int_{1}^{s} \frac{(1+2s^{-1}+3s^{-2}+2s^{-2}+s^{-4})sds}{(s-k^{2})^{2}[4s(s-1)(s-k^{2})]^{1/2}} + \dots \right\} [12]$$

can be expressed by the relation

$$\begin{split} \dot{s} &= \left(\frac{2cs}{a}\right)^{1/2} \left\{ s^{-2}(s-1)(s-k^2) + k^2 s^{-1} \left[ \left(\frac{2}{3}\right) P_2 J \left(1-s^{-3}\right) - \left(\frac{8}{35}\right) P_4 D \left(1-s^{-5}\right) \right] \right\}^{1/2} \end{split}$$
 [6]

Integrate Equation [6] to obtain the time elapsed for the rocket to reach the distance s; this interval can be expressed by the relation

$$t = \left(\frac{2a}{c}\right)^{1/2} \int_{1}^{s} \frac{sds}{\left\{4s(s-1)(s-k^2)[1-k^2(s-k^2)^{-1}M]\right\}^{1/2}} \quad [7]$$

Equation [12] constitutes an approximate solution of Equation [7] to terms of order D and  $J^2$ . Equation [12] can be expanded into the sum of 11 integrals of the form

$$I_{m,n} = \int_{1}^{s} \frac{s^{m-n} ds}{(s-k^2)^m \left[4s(s-1)(s-k^2)\right]^{1/2}}$$
[13]

where  $m=0, n=-1; m=1, n=0, 1, \ldots, 4; m=2, n=1, 2, \ldots, 5$ . By means of the substitution  $s=\sin^{-2}\varphi$ , Equation [13] can be transformed into the expression

$$I_{m,n} = \int_{\varphi_1}^{\pi/2} \frac{\sin^{2n} \varphi d\varphi}{(1 - k^2 \sin^2 \varphi)^{(1/2)(2m+1)}}$$
[14]

where  $\varphi_1 = \sin^{-1}(s^{-1/s})$ . Complete integrals of some of the forms indicated in Equation [14] have been tabulated (8). The incomplete integrals, however, must be reduced to simpler forms before evaluation can be effected. Integration of Equation [14] by parts yields the following recursion formula

$$\int_{\varphi_1}^{\pi/2} \frac{\sin^{2n} \varphi d\varphi}{(1 - k^2 \sin^2 \varphi)^{(1/2)(2m+1)}} = \int_{\varphi_1}^{\pi/2} \frac{\sin^{2n-2} \varphi d\varphi}{(1 - k^2 \sin^2 \varphi)^{(1/2)(2m+1)}} - \frac{2n - 2}{k^2(2m - 1)} \int_{\varphi_1}^{\pi/2} \frac{\sin^{2n-2} \varphi d\varphi}{(1 - k^2 \sin^2 \varphi)^{(1/2)(2m-1)}} + \frac{2n - 3}{k^2(2m - 1)} \int_{\varphi_1}^{\pi/2} \frac{\sin^{2n-4} \varphi d\varphi}{(1 - k^2 \sin^2 \varphi)^{(1/2)(2m-1)}} + \frac{1}{k^2(2m - 1)} \frac{s^{m-n+1/2} (s - 1)^{1/2}}{(s - k^2)^{(1/2)(2m-1)}}$$
[15]

The quantity M in Equation [7] is specified by the relation

$$M = -(2/3) P_2 J (1 + \varepsilon^{-1} + \varepsilon^{-2}) + (8/35) P_4 D (1 + \varepsilon^{-1} + \varepsilon^{-2} + \varepsilon^{-3} + \varepsilon^{-4})$$
[8]

The integrals of Equation [14] can be evaluated by means of successive application of Equation [15] and the use of standard reduction formulas (9).

Consider the order of magnitude of the second- and fourthorder corrections to the zero-order solutions previously pubtit

the

eff Eq

tai

folle

The

JUL

lished (1). The exact solutions, specified by Equations [5, 6 and 9], can be written in the approximate forms

0

]

$$\ddot{r} = \ddot{r_0} \left( 1 + \frac{\Delta^2 \ddot{r}}{\ddot{r_0}} + \frac{\Delta^4 \ddot{r}}{\ddot{r_0}} \right)$$
 [16]

$$\dot{r} = \dot{r}_0 \left( 1 + \frac{\Delta^2 \dot{r}}{\dot{r}_0} + \frac{\Delta^4 \dot{r}}{\dot{r}_0} \right)$$
 [17]

$$t = t_0 \left( 1 + \frac{\Delta^2 t}{t_0} + \frac{\Delta^4 t}{t_0} \right)$$
 [18]

where  $\ddot{r}_0$ ,  $\dot{r}_0$  and  $t_0$  are the zero-order solutions. The quan-

tute severe restrictions on the problem. In general, the corrections will be much smaller than those indicated.

### **Evaluation to Second Order**

In the case of the planet Earth, evaluation to fourth order is not justified in view of experimental uncertainty in D and  $J^2$ . There is considerably less information about the effect of the oblateness of the other planets. Evaluation of Equation [12] will be carried out only to terms of J in order to illustrate the method. Further extension of the calculation to terms of order D and  $J^2$  involve merely additional mathematical manipulations of the same kind as those performed. Equation [12] can be written in terms of J in the form

$$t = \left(\frac{2a}{c}\right)^{1/2} \left\{ \int_{\varphi}^{\pi/2} \frac{d\varphi}{\sin^2 \varphi (1 - k^2 \sin^2 \varphi)^{1/2}} - \frac{1}{3} k^2 P_2 J \left[ \int_{\varphi_1}^{\pi/2} \frac{d\varphi}{(1 - k^2 \sin^2 \varphi)^{3/2}} + \int_{\varphi_1}^{\pi/2} \frac{\sin^2 \varphi d\varphi}{(1 - k^2 \sin^2 \varphi)^{3/2}} + \int_{\varphi_1}^{\pi/2} \frac{\sin^4 \varphi d\varphi}{(1 - k^2 \sin^2 \varphi)^{3/2}} + \dots \right] \right\} \quad [25]$$

The last integral of Equation [25] can be reduced by Equation [15]; Equation [25] can then be written in the form

$$t = \left(\frac{2a}{c}\right)^{1/2} \left\{ \int_{\varphi_1}^{\pi/2} \frac{d\varphi}{\sin^2 \varphi (1 - k^2 \sin^2 \varphi)^{1/2}} - \frac{1}{3} k^2 P_2 J \left[ \int_{\varphi_1}^{\pi/2} \frac{d\varphi}{(1 - k^2 \sin^2 \varphi)^{3/2}} + 2 \int_{\varphi_1}^{\pi/2} \frac{\sin^2 \varphi d\varphi}{(1 - k^2 \sin^2 \varphi)^{3/2}} - \frac{2}{k^2} \int_{\varphi_1}^{\pi/2} \frac{\sin^2 \varphi d\varphi}{(1 - k^2 \sin^2 \varphi)^{1/2}} + \frac{1}{k^2} \int_{\varphi_1}^{\pi/2} \frac{d\varphi}{(1 - k^2 \sin^2 \varphi)^{1/2}} + \frac{1}{k^2} \left( \frac{s - 1}{s(s - k^2)} \right)^{1/2} + \dots \right] \right\}$$
 [26]

The elliptic integrals of Equation [17] have been tabulated (9,10). Equation [26] can be expressed in the form

$$t = \left(\frac{2a}{c}\right)^{1/2} \left\{K - F(\varphi_1, k) - E + E(\varphi_1, k) + \left[s^{-1}(s - 1)(s - k^2)\right]\right\} - \frac{1}{3} P_2 J \left(\frac{2a}{c}\right)^{1/2} \left\{-k^{-2}(2 + k^2) \left[K - F(\varphi_1, k)\right] + k^{-2}(1 - k^2)^{-1}(2 + k^4) \left[E - E(\varphi_1, k)\right] + \frac{1}{1 - k^2} \left[\frac{s - 1}{s(s - k^2)^3}\right]^{1/2} \left[(k^4 + k^2 + 1)s - k^4(2 + k^2) + k^2 - 1\right] + \dots\right\}$$
 [27]

tities  $\Delta^2 \ddot{r}$ ,  $\Delta^2 \dot{r}$ ,  $\Delta^2 t$  and  $\Delta^4 \ddot{r}$ ,  $\Delta^4 t$ , are the respective second- and fourth-order differential corrections obtained by the methods used in this paper. The differential corrections will have their maximum effect relative to the zero-order effect when s=1 and when c is comparable to g. Expand Equations [5, 6 and 9], and evaluate at the point s=1 to obtain the relations

$$\ddot{r} = \left(c - \frac{g}{s^2}\right) \left[1 + 2\left(\frac{g}{c - g}\right) P_2 J - \frac{8}{7} \left(\frac{g}{c - g}\right) P_4 D\right]$$
 [19]
$$\dot{r} = \left[\frac{2a(s - 1)(cs - g)}{s}\right]^{1/s} \left[1 + \left(\frac{g}{c - g}\right) P_2 J - \frac{4}{7} \left(\frac{g}{c - g}\right) P_4 D + \frac{1}{2} \left(\frac{g}{c - g}\right)^2 P_2^2 J^2\right]$$
 [20]

$$t = \left[\frac{2as(s-1)}{cs-g}\right]^{1/2} \left[1 - \left(\frac{g}{c-g}\right)P_2J + \frac{4}{7}\left(\frac{g}{c-g}\right)P_4D + \frac{3}{2}\left(\frac{g}{c-g}\right)^2P_2^2J^2\right]$$
 [21]

Set  $P_2 = 1$ ,  $P_4 = 1$  and c = 2g in Equations [19, 20 and 21], and use the values of J and D from Table 1 to obtain the following relations that apply to Earth

$$\ddot{r} = [c - (g/s^2)][1 + 0.003274 - 0.000012]$$
 [22]

$$\dot{r} = \left[\frac{2a(s-1)(cs-g)}{s}\right]^{1/2} [1 + 0.001637 - 0.000005]$$
 [23]

$$t = \left[\frac{2as(s-1)}{cs-g}\right]^{1/2} [1 - 0.001637 + 0.000010]$$
 [24]

Equations [22, 23 and 24] can be used to estimate the magnitude of the second- and fourth-order effects of oblateness. The values used to obtain Equations [22, 23 and 24] consti-

The respective quantities K and  $F(\varphi_1,k)$  in Equation [27] are complete and incomplete elliptic integrals of the first kind; the respective quantities E and  $E(\varphi_1,k)$  are the complete and incomplete elliptic integrals of the second kind. The first term of Equation [26] is the result previously published (1); the remaining terms constitute the new results derived in this paper.

#### **Numerical Example**

A numerical example has been evaluated in order to compare the approximate and the exact solutions. Recall that the boundary conditions require that the rocket start from rest at the equatorial distance a from the center of the planet. This requirement means that the rocket can start from rest from the surface of the planet at the Equator only. At other latitudes (see Fig. 1) the rocket must start from an elevation just sufficient to compensate for the difference in distance to the center of the planet caused by its oblateness. Launching from considerable altitude by means of a plane or a balloon is definitely an engineering possibility. There are considerable advantages to an air launched rocket, since about 94 per cent of the atmosphere lies below 20,000-m altitude (11).

Launching at a latitude other than  $\pi/2$  requires that the rocket, in order to satisfy the imposed boundary conditions, must quickly acquire a component of velocity normal to its trajectory in order to cancel the effect of rotation. At latitudes other than zero and  $\pi/2$ , the rocket must also undergo a slight acceleration normal to its trajectory in order to remain on a radius vector, since the force of gravitation given by  $\nabla U$  is not central. Reference to Equation [1] suggests that the maximum perturbation effect occurs for a rocket launched at a pole where the effect is twice that, and in oppo-

site direction to, the effect produced at the Equator. Reference to Equation [27] suggests that the second-order effects of the oblateness of a planet vanish entirely at the latitude  $35^{\circ}-15'-52''$ . This result follows from the fact that  $P_2(\cos\theta)$  has a root at this value. Similarly, the fourth-order effects vanish at latitudes  $19^{\circ}-52'-33''$  and  $59^{\circ}-26'-40''$ .

In view of the preceding discussion, the problem has been evaluated for a rocket launched at the altitude a-b=21,477 m above a pole of Earth; see Fig. 1. Values of the

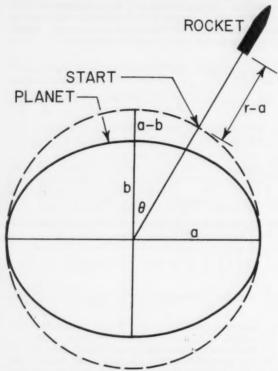


Fig. 1 Rocket moving radially away from an oblate planet.

Dashed circle indicates boundary conditions

g, 1

parameters used in the solution are listed in Table 1. The constant g in Table 1 was determined so that the acceleration due to gravity at the pole is given by Equation [1]; that is,  $g[(a/b)^2 - 2J(a/b)^4 + (8/7)D(a/b)^6]$  is the theoretical value of gravity at the pole (983.2213 cm per sec2).8 The values of the equatorial and polar radii of Earth were taken to be a = 6.378,388 m and b = 6.356,911 m, respectively. The polar axis b is a computed quantity based upon the assumption that a/(a-b) = 297.0, exactly. If Earth were a homogeneous ellipsoid, the coupling constants J and D would be functions of the eccentricity e of Earth; that is, J would be  $(3/10)e^2$  and D would be  $(3/8)e^4$  where  $e^2 = 1 - (b/a)^2$ . The theoretical value of the coupling constants for a homogeneous ellipsoid are:  $J=2.017\times 10^{-3}$  and  $D=16.9\times 10^{-6}$ . The experimental values  $J=(1.637\pm 0.004)\times 10^{-3}$ and  $D = 10.6 \times 10^{-6}$  suggest that the actual gravitational field of Earth is somewhere intermediate between that of a homogeneous ellipsoid and a sphere. Since the mean density of Earth (5.517 g per cm3) is considerably greater than the average density of the continents (2.679 g per cm³), Earth cannot be homogeneous. The value chosen for c in the last column of Table 1 was about 10.5 g. This magnitude of acceleration, chosen for mathematical convenience, represents a reasonable upper limit to the intensity of acceleration that can be sustained for a short time by a well-conditioned human

Table 2 contains the results of the zero-order solution obtained from Equations [5, 6 and 9] by setting J=0 and D=0, and using the value of the other parameters listed in Table 1. The exact values, also listed in Table 2, were obtained from Equations [5, 6 and 9] by the use of all of the parameters listed in Table 1. The difference between an entry for the zero-order and the corresponding entry for the exact value is the sum of differential corrections of the second- and higher even orders. These total differential corrections are listed in Table 3 and are plotted in Fig. 2. The total differential corrections do not differ, to the precision of the numbers tabulated, from the second-order differential corrections. Thus, in this example, the second-order solution is equivalent to the exact solution.

<sup>3</sup> See (11), pp. 2–100. The geodetic quantities chosen in this paper are those of the International Ellipsoid adopted in 1930 by the International Geodetic and Geophysical Union.

Table	1 Parameters	used in the problem	n of a rocket launche	ed from a pole of E	arth
ravity	Radius	Co-latitude	Coupling	Acceleration	
m/sec <sup>2</sup>	a, m	$\theta$ , deg	J	D	c, m/sec <sup>2</sup>
798,288	6,378,388	0	$1.637 \times 10^{-3}$	$10.6 \times 10^{-6}$	102.609

Distance s,	Velocity r,	km/sec	Acceleration	n r, m/sec*	Time	t, sec
Earth radii	zero-order	exact	zero-order	exact	zero-order	exact
1.0	00.000	00.000	92.810	92.842	000.000	000.000
1.1	10.933	10.934	94.511	94.533	117.044	117.025
1.2	15.522	15.524	95.804	95.820	165.282	165.257
1.3	19.074	19.076	96.811	96.822	202.160	202.131
1.4	22.087	22.089	97.609	97.618	233.154	233.122
1.5	24.755	24.756	98.254	98.260	260.389	260.355
1.6	27.175	27.177	98.781	98.786	284.955	284.919
1.7	29.409	29.409	99.218	99.222	307.501	307.463
1.8	31.489	31.491	99.584	99.587	328.449	328.410
1.9	33.449	33.450	99.894	99.897	348.094	348.054
2.0	35.305	35.306	100.159	100.161	366.648	366.607

h

of

R

Ju

Table 3 Differential corrections for velocity, acceleration and elapsed time of a typical rocket

			7.4
Distance 8, Earth radii	Velocity correction $\Delta \dot{r}$ , m/sec	Acceleration correction $\Delta \ddot{r}$ , m/sec <sup>2</sup>	Time correction $\Delta t$ , sec
1.0	0.00	0.031	-0.000
1.2	1.84	0.015	-0.025
1.4	1.95	0.008	-0.032
1.6	1.89	0.004	-0.036
1.8	1.79	0.003	-0.038
2.0	1.68	0.002	-0.040
2.2	1.59	0.001	-0.042
2.4	1.50	0.001	-0.043
2.6	1.42	0.000	-0.044
2.8	1.36	0.000	-0.045
3.0	1.30	0.000	-0.046
	Earth radii 1.0 1.2 1.4 1.6 1.8 2.0 2.2 2.4 2.6 2.8	$\begin{array}{cccccccccccccccccccccccccccccccccccc$	$\begin{array}{c ccccccccccccccccccccccccccccccccccc$

#### Conclusions

The differential correction that pertains to the J coupling constant is relatively small for the illustrative example studied, and the differential correction that pertains to the D coupling constant is negligible. The respective acceleration and velocity differential corrections  $\Delta \vec{r}$  and  $\Delta \vec{r}$  approach zero as a approaches infinity. Fig. 2 indicates that the velocity correction  $\Delta r$  attains a maximum value r = 1.958 m per sec in the neighborhood of the distance s = 1.37. The time correction  $\Delta t$  approaches a maximum value t = -0.05953sec as a approaches infinity.

The restricted problem solved in this paper is characterized by an analytical solution. This result presumably can be generalized by perturbation techniques to the more realistic case where the acceleration and trajectory may vary from the assumed conditions. Results of the restricted problem, however, suggest that the corrections due to the oblateness of a planet are generally small or negligible. This conclusion can be applied directly to the more general case.

#### Acknowledgments

It is a pleasure to acknowledge the assistance of Daniel B. Ray who coded the problem and performed the numerical evaluations on the IBM 704 calculator. The illustrations were done by James W. Rogers.

#### References

- 1 Allen, W. A., "Two Ballistics Problems of Future Transportation,"
- Allen, W. A., "Two Ballistics Problems of Future Transportation," Amer. J. Phys., vol. 21, 1953, pp. 83-89.
   Jeffreys, H., "The Earth. Its Origin, History and Physical Constitution," Cambridge University Press, N. Y., third ed., 1952, p. 129.
   Byerly, W. E., "An Elementary Treatise on Fourier's Series and Spherical, Cylindrical, and Ellipsoidal Harmonics," Ginn and Company, N. Y., first ed., 1893, pp. 151-157.

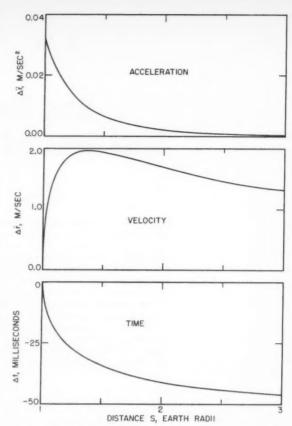


Fig. 2 Differential corrections to zero-order acceleration, velocity and time to obtain second-order solution

- 4 Moulton, F. R., "An Introduction to Celestial Mechanics," The MacMillan Company, Ltd., N. Y., second ed., 1928, p. 119.
  5 Blitzer, L., Weisfeld, M. and Wheelon, A. D., "Perturbations of a Satellite's Orbit Due to the Earth's Oblateness," J. Appl. Phys., vol. 27,
- 1956, pp. 1141-1149.

- 1956, pp. 1141-1149.
  6 Blitzer, L. and Wheelon, A. D., "Oblateness Perturbation of Elliptical Satellite Orbits," J. Appl. Phys., vol. 28, 1957, p. 279.
  7. Blitzer, L., "Apsidal Motion of an IGY Satellite Orbit," J. Appl. Phys., vol. 28, 1957, p. 1362.
  8 Bierens de Haan, D., "Nouvelles Tables D'Integrales Definies," G. E. Stechert and Co., N. Y., edition of 1867, corrected, pp. 89-95.
  9 Byrd, P. F. and Friedman, M. D., "Handbook of Elliptic Integrals for Engineers and Physicists," Springer-Verlag, Berlin, first ed., 1954, pp. 191-195.
- 191-195.
  10 Jahnke, E. and Emde, F., "Tables of Functions with Formulae and Curves," Dover Publications, N. Y., fourth ed., 1945, p. 56.
  11 Gray, D. E., "American Institute of Physics Handbook," McGraw-Hill Book Co., Inc., N. Y., first ed., 1957, pp. 3-58, 2-100.

# Mass Transfer and **Shock Generated Vorticity**

H. HOSHIZAKI<sup>1</sup>

Lockheed Aircraft Corp. Sunnyvale, Calif.

The effects of shock generated vorticity and mass transfer on stagnation point heat transfer rates are investigated. The complete incompressible Navier-Stokes equations are considered in the flow region between the bow shock and the surface of spheres and cylinders. Boundary conditions are applied immediately behind the shock and at the wall. The numerical solutions to the flow equations with air injected into the shock layer, show that the interaction between the vorticity generation ated by the wall and by the curved shock reduces the effectiveness of mass transfer cooling. The reduction in heat transfer rates due to mass injection is substantially less than predicted by boundary layer theory at Reynolds numbers below 105 for spheres and 104 for cylinders. The heat transfer rates with mass injection were found to be 200 to 300 per cent greater than corresponding boundary layer values for the extreme cases investigated (strong shock,  $Re \cong 10^3$  and large air injection rates). These heat transfer rates are, however, less than the zero mass injection values. It is also shown for a sphere and for Pr = 1.0 that the increase in heat transfer is primarily dependent on the inverse of the difference between the vorticity at the wall and the vorticity immediately behind the shock.

MASS transfer is important in several methods for protecting the surface of hypervelocity vehicles. For example, on an ablating body the interface temperature of the liquid sublayer may be sufficiently high to vaporize the liquid. The vaporized mass will subsequently be injected into the air boundary layer. It has been shown by numerous authors (1-5)2 that the injection of mass into boundary layers results in substantial reductions in conductive heat transfer rates. Thus, it is necessary to know the quantitative reduction in heat transfer rates with mass injection in order to accurately compute ablation rates. For a more detailed discussion of ablation the reader is referred to (6 and 7).

Another method of protecting hypervelocity vehicles from severe aerodynamic heating is to use materials, such as graphite and Teflon which sublime at high temperatures. The sublimated mass is injected into the boundary layer, and again one must know the effects of mass injection on heat transfer rates to compute sublimation rates.

Mass transfer cooling, the process whereby fluid is injected into the boundary layer from a porous wall, is also an effective means of alleviating aerodynamic heating. Obviously for such a scheme one must know the effects of mass injection on heat transfer rates.

It is the purpose of this paper to show that the reduction in stagnation point heat rates by mass injection is markedly affected by shock generated vorticity for  $Re \simeq 10^5$  and lower. Reference (8) contains an analysis of the effect of shock generated vorticity on stagnation point heat transfer rates on a hemisphere, without mass injection, at low Reynolds numbers. The results show that the interaction between the vorticity generated by the bow shock and the vorticity at the wall substantially increases the heat transfer rates over the values predicted by classical boundary layer theory. It was also shown for the special case of a sphere and for Pr = 1.0, that the increase in heat transfer rates is primarily dependent on the inverse of the difference between the vorticity at the wall ζ, and the vorticity immediately behind the shock ζ. At high Reynolds numbers (Re > 106), 5 is much greater than ζ, and the heat transfer rates are little affected by shock generated vorticity. As the Reynolds number is decreased, ζω decreases whereas ζ, is only slightly affected. Hence, at low Reynolds numbers, the heat transfer rates are increased over boundary layer values by virtue of the decreased magnitude of the quantity  $(\zeta_w - \zeta_s)$ . Since boundary layer solutions show that mass injection decreases \( \xi\_w \) [see (5) for example], one would expect heat transfer rates considerably higher than those predicted by boundary layer theory when mass is injected into the shock layer at moderately low Rey-

These qualitative conclusions are verified by the results of the present analysis. Numerical solutions to the incompressible Navier-Stokes equations with air injection into the shock layer were obtained for flows in the vicinity of the stagnation point of hemispheres and cylinders. These solutions give heat transfer rates which are as much as 200 to 300 per cent higher than those predicted by boundary layer theory for the same injection rates. Although the present solutions are for single component flows, one can logically expect similar increases in heat transfer rates over the corresponding boundary layer solutions for multicomponent flows, which are more appropriate for ablation and sublimation calculations.

#### Analysis

#### **Basic Equations and Boundary Conditions**

The present analysis is confined to the vicinity of the forward stagnation points of hemispheres and cylinders where the flow is assumed to be incompressible. The results of an incompressible analysis when referenced to the proper boundary layer results will give the correct trends when applied to a compressible flow. The magnitudes of the results of such an analysis should also be very good, since the difference in compressibility effects between a shock layer and boundary

Received June 17, 1959.

Senior Scientist, Thermodynamics Department, Missile Systems Division.

Numbers in parentheses indicate References at end of paper.

628

pect Tr Prol that port shov pape anal erali nort

equa (8) t

wher In o

writt

wher

and

JULY

ARS JOURNAL

layer analysis at moderately low Reynolds number is ex-

pected to be a second-order effect.

In this analysis the region between the body and bow shock (shock layer) is considered to be completely viscous, whereas the shock wave is assumed to be a discontinuity. Adams and Probstein (9) have shown by an order-of-magnitude analysis that these conditions can be expected if the ratio of body radius to the mean free path at the wall  $r_w/\lambda_w$ , which is proportional to  $M_\infty Re_\infty$ , is greater than  $O(10)^2$ . It was also shown for  $M_\infty Re_\infty > 0(10)^2$  that the usual vorticity transport, continuity and energy equations are applicable. In this paper, the development of these equations closely follows the analysis of (8). However, for completeness, pertinent portions of the analysis will be repeated here with a slight generalization to include stagnation points on cylinders aligned normal to the flow. It should also be noted that the analysis can be extended to include other bodies of the conic family.

The vorticity transport, continuity and energy equations in the coordinate system shown in Fig. 1 can be written as:

Vorticity transport

$$r^{n+1} u \frac{\partial}{\partial r} \left( \frac{\zeta}{r^n} \right) + v \sin^n \theta \frac{\partial}{\partial \theta} \left( \frac{\zeta}{\sin^n \theta} \right) = v \left\{ \frac{\partial}{\partial r} \left[ \frac{1}{r^{n-1}} \frac{\partial}{\partial r} \left( r^n \zeta \right) \right] + \frac{\partial}{\partial \theta} \left[ \frac{1}{r \sin^n \theta} \frac{\partial}{\partial \theta} \left( \sin^n \theta \zeta \right) \right] \right\}$$
[1]

Continuity

$$\frac{\partial}{\partial r} (r^{n+1} \sin^n \theta u) + \frac{\partial}{\partial \theta} (r^n \sin^n \theta v) = 0$$
 [2]

Energy

$$\begin{split} \rho C_{p} \left( u \; \frac{\partial T}{\partial r} \; + \; \frac{v}{r} \; \frac{\partial T}{\partial \theta} \right) = \; k \left[ \frac{1}{r^{n+1}} \frac{\partial}{\partial r} \left( r^{n+1} \; \frac{\partial T}{\partial r} \right) \; + \right. \\ \left. \frac{1}{r^{2} \sin^{n} \theta} \; \frac{\partial}{\partial \theta} \left( \sin^{n} \theta \; \frac{\partial T}{\partial \theta} \right) \right] \quad [3] \end{split}$$

where n=1 for the sphere, n=0 for the cylinder, and the vorticity  $\zeta$  is defined by

$$\zeta = \frac{1}{r} \left[ \frac{\partial}{\partial r} (rv) - \frac{\partial u}{\partial \theta} \right]$$
 [4]

The dissipation and pressure gradient terms in the energy equation have been omitted, since these terms were shown in (8) to be negligible.

 ${\bf A}$  stream function is now introduced and is assumed to have the form

$$\psi = (U_{\infty} r_w^{n+1} / \sqrt{Re}) \sin^{n+1} \theta h(\eta)$$
 [5]

where

$$\eta = [(r/r_w) - 1]\sqrt{Re}$$
 [6]

In order to satisfy continuity, the velocity components are written as

$$v = (U_{\infty} \sin \theta / \tilde{\eta}^n) h'(\eta)$$
 [7]

$$u = -\left[(n+1)U_{\infty}\cos\theta/\tilde{\eta}^{n+1}\sqrt{Re}\right]h(n)$$
 [8]

where

$$\tilde{\eta} = r/r_w \tag{9}$$

and the prime denotes differentiation with respect to  $\eta$ . Furthermore, let

$$\begin{split} \bar{\xi}(\eta) &= \frac{r_w^{n+1} \, \xi}{\sqrt{Re} \, U_\infty \sin \theta \, r^n} = \\ &\qquad \qquad \frac{1}{\bar{\eta}^{n+1}} \bigg[ \frac{h''}{\bar{\eta}^{n-1}} + \frac{(1-n)h'}{\bar{\eta}^n \sqrt{Re}} - \frac{(n+1)h}{\bar{\eta}^{n+1} Re} \bigg] \quad [10] \end{split}$$

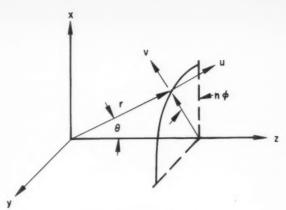


Fig. 1 Coordinate system

$$g(\eta) = (T - T_w)/(T_s - T_w)$$
 [11]

By means of these relations the vorticity and energy equations become:

Vorticity

$$\begin{split} -(n+1)h\overline{\xi}' + (1-n)h'\overline{\xi} &= \\ \left(\widetilde{\eta}^{n+1}\overline{\xi}' + 2n\widetilde{\eta}^n \frac{\overline{\xi}}{\sqrt{Re}}\right) - (1+n)\widetilde{\eta}^{n-1} \frac{\overline{\xi}}{Re} \end{split} [12]$$

Energy

$$-(n+1)hg' = (1/Pr)(\tilde{\eta}^{n+1}g')'$$
 [13]

Although the vorticity equation is a fourth-order equation five boundary conditions are necessary to specify a solution completely. The additional boundary condition is used to determine the unknown shock detachment distance. Two additional boundary conditions on the temperature profile are necessary to solve the energy equation. These boundary conditions are given at the body surface or immediately behind the bow shock, which is assumed to be a concentric sphere or cylinder. At the wall

$$v = 0 ag{14a}$$

$$u = u_w ag{14b}$$

$$T = T_w$$
 [14c]

and immediately behind the shock

$$v_s = U_{\infty} \sin \theta$$
 [14d]

$$u_* = -\overline{\rho}U_{\infty}\cos\theta \tag{14e}$$

$$T = T_s ag{14f}$$

where the strong shock approximations were used to obtain Equations [14d and 14e]. The  $\theta$  momentum equation evaluated immediately behind the shock provides the additional boundary condition necessary to determine the shock detachment distance. The  $\theta$  momentum equation is

$$u \frac{\partial v}{\partial r} + \frac{v}{r} \frac{\partial v}{\partial \theta} + \frac{uv}{r} = -\frac{1}{\rho} \frac{\partial p_s}{r \partial \theta} + \frac{v}{r^n} \frac{\partial}{\partial r} \left\{ r^{n-1} \left[ \frac{\partial (r \ v)}{\partial r} - \frac{\partial u}{\partial \theta} \right] \right\}$$
[15]

where

$$p_s = (1 - \bar{\rho})\bar{\rho}\rho U_{\infty}^2 \cos^2 \theta \qquad [16]$$

629

Transformation of these boundary conditions results in

$$h'(0) = 0 ag{17a}$$

$$h(0) = -\frac{\sqrt{Re}}{(n+1)} \frac{u_w}{U_\infty \cos \theta}$$
 [17b]

$$g(0) = 0 ag{17c}$$

$$h'(\eta_s) = \tilde{\eta}_s^n$$
 [17d]  
 $h(\eta_s) = \tilde{\eta}^{n+1} \bar{\rho} \sqrt{Re}/(n+1)$  [17e]

$$a(\eta_s) = \tilde{\eta}^{n+1} \bar{\rho} \sqrt{Re}/(n+1)$$
 [17e]  
 $a(\eta_s) = 1$  [17f]

The  $\theta$  momentum equation then becomes

Equation [25] it is seen that this reduction in 
$$\zeta_w$$
 and  $\partial \zeta_w/\partial r$  tends to reduce the heat transfer rate, but there is a compensating effect since  $\zeta_w$  also appears in the denominator. The compensating effect increases as  $r_w\zeta_w \to r_s\zeta_s$ . This can be seen more clearly by rewriting Equation [25] in terms of  $h(\eta)$  and the Nusselt number, and taking the limit as  $Re \to \infty$ 

$$\frac{Nu}{\sqrt{Re}} = \frac{2[-h^{\prime\prime\prime}(0) + 2h^{\prime\prime}(0)/\sqrt{Re} - 8h(0)/Re^{3/2}]}{[h^{\prime\prime}(0) - 2h(0)/Re] - [h^{\prime\prime}(\eta_s) - 2h(\eta_s)/Re]} + \left[2h^{\prime}\frac{(\eta_s)}{\tilde{\eta}_s}\sqrt{Re}\right] + \frac{2[h(\eta_s)/\tilde{\eta}_s^2 - h(0)]}{R_e}$$
[26]

$$-h''(\eta_{\epsilon}) = \left[\tilde{\eta}^{n+1}\overline{\rho}\sqrt{Re} - \frac{(n-1)}{\sqrt{Re}}\tilde{\eta}_{\epsilon}^{n}\right]^{-1}\left[2\overline{\rho}(1-\overline{\rho})\tilde{\eta}_{\epsilon}^{2n} + \tilde{\eta}_{\epsilon}^{n+1}h'''(\eta_{\epsilon}) - \frac{2\tilde{\eta}_{\epsilon}^{2n-1}}{Re}(1-\overline{\rho}) - (n-1)\tilde{\eta}_{\epsilon}^{2n}\overline{\rho} - \tilde{\eta}_{\epsilon}^{2n}\right]$$
[18]

#### **Heat Transfer Relations**

The temperature distribution through the shock layer is obtained by integrating the energy equation. Integration of Equation [13] results in

$$g(\eta) = a_0 \int_0^{\eta} \exp\left[-\int_0^{\eta} (n+1) \left(\frac{Prh}{\tilde{\eta}^{n+1}} + \frac{1}{\tilde{\eta}\sqrt{Re}}\right) d\eta\right] d\eta$$
[19]

where the constant of integration is

$$a_0^{-1} = \int_0^{\eta_S} \exp \left[ - \int_0^{\eta} (n+1) \left( \frac{Pr h}{\tilde{\eta}^{n+1}} + \frac{1}{\tilde{\eta}\sqrt{Re}} \right) d\eta \right] d\eta$$

The heat transfer rate at the wall is given by

$$\dot{q}_w = k \frac{\partial T}{\partial r}$$
 [21a]

$$\dot{q}_w = k(\sqrt{Re/r_w})a_0(T_s - T_w)$$
 [21b]

or in nondimensional form

$$Nu/\sqrt{Re} = 2a_0$$
 [22]

where

$$Nu = hD/k [23]$$

$$h = \dot{q}_w / (T_A - T_w) \tag{24}$$

In the most general case, the constant of integration  $a_0$  can only be evaluated after a solution of the vorticity equation has been obtained. However, for the special case of a sphere and Pr=1, Equation [20] can be integrated to obtain the heat transfer rate in terms of quantities evaluated at the wall and immediately behind the shock wave. The integration for the zero mass injection case is presented in (8). In order to include the effects of air injection, the wall boundary condition on the u velocity component is changed from u=0 to  $u=u_v$ . For the heat transfer rate at the wall there results

$$\dot{q}_w = \frac{k(-r_w \, \eth \zeta_w / \eth r + \zeta_w)(T_s - T_w)}{(r_w \zeta_w - r_s \zeta_s) + U_\infty \sin \theta (2 + \overline{\rho}) + u_w \tan \theta} \quad [25]$$

The effect of shock generated vorticity on the heat transfer rate is clearly shown by Equation [25]. At large Reynolds numbers,  $r_w \zeta_w$  is much greater than  $r_s \zeta_s$ , so that the vorticity behind the shock has little effect on the heat transfer rate. At low Reynolds numbers,  $O(r_w \zeta_w)$  is equal to  $O(r_s \zeta_s)$ , and the heat transfer rate will differ markedly depending on whether or not shock generated vorticity is taken into account.

The main effect of mass transfer is in reducing the vorticity  $(\zeta_w)$  and the vorticity gradient  $(\partial \zeta_w/\partial r)$  at the wall. From

Equation [26] shows that the direct effect of the mass injection velocity  $[u_w \ \alpha \ h(0)]$  is relatively small. The limit of Equation [26] as  $Re \rightarrow \infty$  is

$$\frac{Nu}{\sqrt{Re}} = \frac{-2h'''(0)}{h''(0) - h''(\eta_*)}$$
[27]

which can be shown to be equivalent to the result obtained from boundary layer theory when applied to flow fields with external vorticity. Now, h'''(0) is proportional to  $\partial \zeta_w/\partial r$ ,  $h''(0) \propto r_w\zeta_w$  and  $h''(\eta_s) \propto r_s\zeta_s$ , and since mass injection decreases h'''(0) and h'''(0) but has little effect on  $h''(\eta_s)$ , it is easily seen that the effectiveness of mass injection in reducing heat transfer decreases as  $h''(0) \rightarrow h''(\eta_s)$  (or as the Reynolds number decreases). One other observation can be made about the effect of mass injection on heat transfer. Since the increase in heat transfer rates resulting from shock generated vorticity can essentially be attributed to the term  $(r_w\zeta_w - r_s\zeta_s)$  in Equation [25], and since mass injection decreases  $\zeta_w$ , one would expect that the effect of shock generated vorticity on heat transfer rates at a given Reynolds number is larger with injection than without injection.

#### **Numerical Results**

Numerical solutions to the vorticity transport equation (Eq. [12]) were obtained by successive approximations. Equation [12] was first put into integral form by repeated integration. The constants of integration were then evaluated by means of the boundary conditions on the velocities (Eq. [17]).

Estimates were first made of the shock detachment distance  $\eta_s$  and the function  $h(\eta)$  for specified values of the density ratio  $\overline{\rho}$ , the Reynolds number Re, and the injection rate parameter h(0). The integral form of the vorticity equation was then solved, holding  $\eta_s$  constant, by successive approximations. The function  $h(\eta)$  and its first three derivatives were required to converge to within 0.001. The solution thus obtained was then used to evaluate the error in the  $\theta$  momentum equation boundary condition (Eq. [18]). This procedure was repeated for various values of  $\eta_s$  until Equation [18] was satisfied.

Representative numerical results for the sphere and cylinder are presented in this section. Shock layer velocity, temperature and vorticity profiles along with various Nusselt number ratios are discussed. Additional numerical results for the sphere and cylinder are presented in (10).

#### Shock Layer Profiles and Shock Detachment Distance

Velocity, temperature and vorticity profiles in the shock layer are shown in Fig. 2 for both the sphere and the cylinder.

630

rese

the

tion

and

shoy

at th

redu

behi

a re

tion

crea

mas

dista

which

13)

sphe

equa

were

mas

pres

0.06

and

due

The

JUL

R

SI



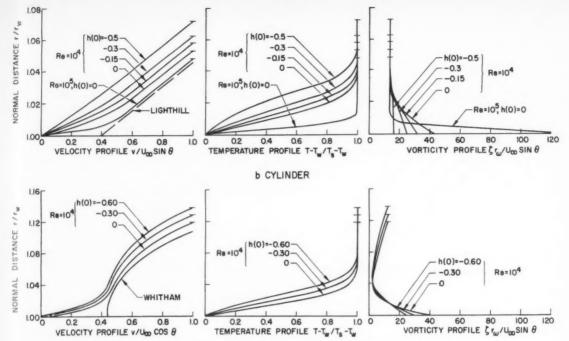


Fig. 2 Shock layer profiles for  $\bar{p} = 0.06$ 

The sphere and cylinder velocity profiles away from the wall resemble the inviscid profile obtained by Lighthill (11) for the sphere and by Whitham (12) for the cylinder. The injection of mass is seen to reduce the velocity gradient at the wall and to thicken the shock layer. The temperature profiles show that mass injection reduces the temperature gradient at the wall, and the vorticity profiles show that mass injection reduces the vorticity at the wall. The vorticity immediately behind the bow shock is affected little by mass injection or by a reduction in Reynolds number.

Shock detachment distances are shown in Fig. 3 as a function of the Reynolds number and the injection rate parameter, for  $\bar{\rho}=0.06$ . The shock detachment distance is seen to increase with decreasing Reynolds number. The injection of mass into the shock layer also increases the shock detachment distance.

# Nusselt Number Ratios

All of the heat transfer data are presented in terms of Nusselt number ratios. The boundary layer Nusselt number, which is used as a reference value, was obtained from (11 and 13) for the zero mass injection case for the sphere. For the sphere mass injection cases, the appropriate boundary layer equations were solved using the digital computer program of (5). The boundary layer Nusselt numbers for the cylinder were obtained from (12 and 14).

Ratios of shock layer theory Nusselt numbers, to the zero mass injection boundary layer theory Nusselt numbers, are presented in Fig. 4 for both the sphere and cylinder, for  $\bar{\rho}=0.06$ . The data are presented for various Reynolds numbers and are plotted as a function of the injection rate parameter h(0). These curves show the reduction in Nusselt number due to mass injection as predicted by shock layer theory. The large effect of vorticity on the sphere with zero mass in-

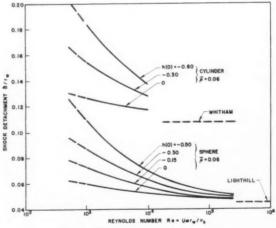


Fig. 3 Shock detachment distances

jection causes the Nusselt numbers at low Reynolds numbers and small injection rates to be higher than the zero mass injection boundary layer Nusselt number. The increase in Nusselt numbers with zero mass injection accounts for a major portion of the percentage difference between shock layer theory and boundary layer theory. The increase in Nusselt numbers owing to shock generated vorticity is much smaller for the cylinder than for the sphere.

The reduction in Nusselt numbers owing to mass injection

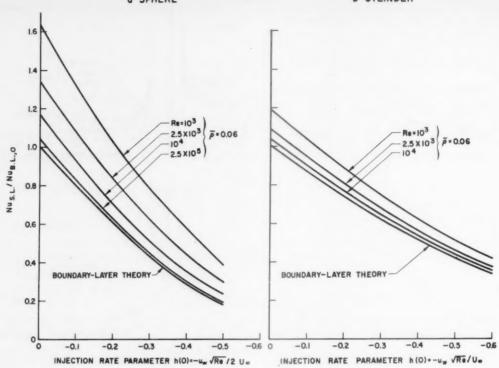


Fig. 4 Ratio of shock layer theory Nusselt number to zero injection boundary layer theory Nusselt number

from the zero mass injection shock layer values is shown in Fig. 5. These curves are similar to those obtained from boundary layer theory. The difference between the curves obtained from shock layer theory and those obtained from boundary layer theory gives the increased effect of shock gen-

erated vorticity when mass transfer is present. This can be seen more easily by considering the ratio of shock layer to boundary layer Nusselt numbers for an arbitrary value of the injection rate parameter. This ratio can be written as

$$\frac{(Nu)_{SL}}{(Nu)_{BL}} = \frac{(Nu)_{SL,0}}{(Nu)_{BL,0}} \left[ \frac{(Nu)_{SL}/(Nu)_{SL,0}}{(Nu)_{BL}/(Nu)_{BL,0}} \right]$$

0.8 - 0.7 - 0.9 - 0.8 - 0.7 - 0.9 - 0.1 - 0.2 - 0.3 - 0.4 - 0.5 - 0.8 - 0.1 - 0.2 - 0.3 - 0.4 - 0.5 -

Fig. 5 Nusselt number reduction as a function of mass injection rate according to shock layer theory,  $\overline{\rho}=0.06$ 

The bracketed quantity is equal to the ratio of the shock layer to the boundary layer curve given in Fig. 5. As an example, for  $Re=10^3$ ,  $\bar{p}=0.06$  and h(0)=-0.50, this ratio for the sphere is equal to 1.30. In other words, under these conditions, the effect of shock generated vorticity on heat transfer is increased 30 per cent by mass injection. Again for the sphere and the same conditions, the ratio of shock layer Nusselt number to boundary layer Nusselt number for zero mass injection is 1.63 (Fig. 4). Therefore, for an injection rate parameter of -0.50, shock layer theory gives a Nusselt number at the stagnation point of a sphere which is 2.12 times as large as the Nusselt number predicted by boundary layer theory for the corresponding value of the injection rate parameter. Note that for a cylinder, the increased effect of shock generated vorticity when mass transfer is present is less than it is for a sphere.

The increase in Nusselt number over the corresponding boundary layer value as predicted by shock layer theory is shown in Fig. 6 as a function of Reynolds number for various injection rates. The increase in Nusselt number becomes significant for Reynolds numbers less than 10<sup>5</sup> for spheres and for Reynolds numbers less than 10<sup>4</sup> for cylinders. At low Reynolds numbers and high mass injection rates, shock layer

twi

cor

Ap

the orb Fig

= (

velo

hen

traj

high pres

rate

obta

flow

prox

bour

rates

theo

ary

para

a fev

Non

JULY

E

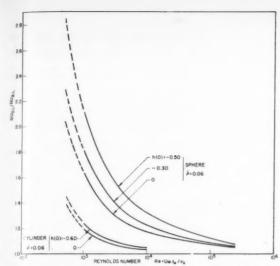


Fig. 6 Shock layer theory Nusselt number to boundary layer theory Nusselt number for specified values of the injection rate parameter  $h(\mathbf{0})$ 

theory for a sphere predicts Nusselt numbers which are about twice the values predicted by boundary layer theory for the corresponding conditions.

# **Application of Results**

The results of the present analysis were used to calculate the heating history of a vehicle re-entering from a satellite orbit. The trajectory used in these calculations is shown in Fig. 7. This trajectory is for  $W/C_DA=100$  lb/ft² and L/D=0.50. The initial re-entry angle is -1.0 deg, and the initial velocity is 25,400 fps. Note that the vehicle begins to skip at about 400 sec.

The heat rates at the stagnation point of a 1.0-ft diameter hemisphere, based on the trajectory shown in Fig. 7, are presented in Fig. 8 for various injection rates. Very early in the trajectory, shock layer theory predicts heat rates which are higher than the free molecule values. This indicates that the present shock layer theory is not valid at these low Reynolds numbers. In Fig. 8, the shock layer and boundary layer heat rates have been extrapolated to the free molecule values to obtain a smooth transition from continuum to free molecule flow.

Early in the trajectory, when the Reynolds numbers are low, the heat rates predicted by shock layer theory are approximately 50 per cent higher than the values predicted by boundary layer theory. Very late in the trajectory, the heat rates predicted by shock layer and boundary layer theory become equal. The total heat input predicted by shock layer theory for an injection rate parameter equal to -0.50 is 24 per cent greater than the total heat input predicted by boundary layer theory. It should be noted that an injection rate parameter equal to -0.50 corresponds to an injection rate of a few hundred lb/sec-ft² under satellite re-entry conditions.



C<sub>n</sub> = Specific heat at constant pressure

D = body diameter

f = modified stream function

 $g = \text{nondimensional temperature, } (T - T_w)/(T_s - T_w)$ 

= modified stream function, also heat transfer coefficient

the thermal conductivity

M = Mach number

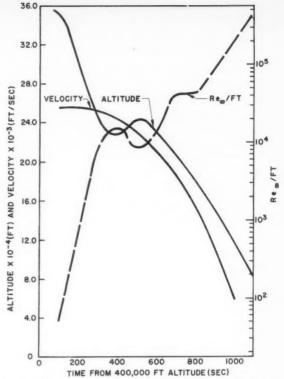


Fig. 7 Lifting re-entry trajectory from satellite orbit,  $W/C_DA=100$ , L/D=0.50

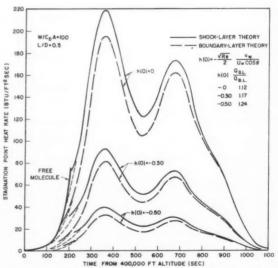


Fig. 8 Re-entry heat rates at the stagnation point of a 1.0-ft diameter hemisphere

Nu = Nusselt number, hD/k

p = pressure

 $Pr = \text{Prandtl number, } C_{p\mu}/k$ 

j = heat transfer rate

coordinate normal to body ReReynolds number,  $U_{\infty}r_{w}/\nu_{s}$ 

body radius 7.00 shock radius T.

nondimensional temperature

T temperature

velocity component in r direction

 $U_{\infty} =$ free stream velocity

velocity component in  $\theta$  direction

shock detachment distance

vorticity component 3

nondimensional normal distance 99

spherical coordinate, body angle λ

mean free path dynamic viscosity kinematic viscosity (see Equation [10])

density

ē density ratio across normal shock,  $\rho_{\infty}/\rho_{\bullet}$ spherical coordinate (circumferential angle)

stream function

#### Subscripts

BL = boundary layer0 = zero mass injection

= conditions behind shock wave

SL = shock layer

= conditions at body surface 20 = free stream conditions Primes denote differentiation.

#### References

1 Low, G. M., "The Compressible Laminar Boundary Layer with Fluid Injection," NACA TN 3404, March 1955.
2 Reshotko, E. and Cohen, C. B., "Heat Transfer at the Forward Stagnation Point of Blunt Bodies," NACA TN 3515, July 1955.
3 Baron, J. R., "The Binary-Mixture Boundary Layer Associated with Mass-Transfer Cooling at High Speeds," MIT Naval Supersonic Laboratory

Fli

cisi

The

req eac

for esc:

ind

grav

thru the the to th segr (1).3Orbi Si turb

sists defin longi plane passa The anon time. the r tion. Th other oscill

Reso Th orbit

Pre Nov. Mem M Meml

EDITO review

JULY

Stagnation Fount of Bruine Boundary Layer Associated with Mass-Transfer Cooling at High Speeds," MIT Naval Supersonic Laboratory TR 160, May 1956.

4 Eckert, J. P., Schneider, P. J., Hayday, A. A. and Larson, R. M. "Mass-Transfer Cooling of a Laminar Boundary Layer by Injection of a Light-Weight Foreign Gas," JEF Properutation, vol. 28, no. 1, Jan. 1958, p. 34.

5 Hoshizaki, H. and Smith, H. J., "Axisymmetric Stagnation Foint Mass-Transfer Cooling," LMBD-48379, Lockheed Missiles and Space Division, Sunnyvale, Calif., Dec. 17, 1958.

6 Scala, S. M. and Sutton, G. W., "The Two-Phase Hypersonic Laminar Boundary Layer—A Study of Surface Melting," Proceedings of the 1958 Heat Transfer and Fluid Mechanics Institute, Stanford University Press, Stanford, Calif., June 19-21, 1958, pp. 231-240.

7 Bethe, H. A. and Adams, M. C. "A Theory for the Ablaticn of Glassy Materials," Avco, Wilmington, Mass., Research Rep. 38, Nov. 1958.

8 Hoshizaki, H., "Shock-Generated Vorticity Effects at Low Reynolds Numbers," LMBD-48381, vol. 1, Lockheed Missiles and Space Division, Sunnyvale, Calif., Jan. 1959, pp. 9-43; ASTIA no. 210401.

9 Adams, M. C. and Probstein, R. F., "On the Validity of Continuum Theory for Satellite and Hypersonic Flight Problems at High Altitudes," JET PROPULSION, vol. 28, no. 2, Feb. 1958, pp. 86-89.

10 Hoshizaki, H., "On Mass-Transfer and Shock-Generated Vorticity, Jet Plant I. Axisymmetric Flow, Part 2—Cylindrical Flow," LMSD-44721, 288075, Lockheed Missiles and Space Division, Sunnyvale, Calif., 1959.

11 Lighthill, M. J., "Dynamics of a Dissociating Gas Part I: Equilibrium," J. Fluid Mech., vol. 2, part 1, Jan. 1957, pp. 1-32.

12 Whitham, G. B., "A Note on the Stand-Off Distance of the Shock in High-Speed Flow Past a Circular Cylinder," Communications on Pure and Applied Math., vol. X, 1957, pp. 531-535.

13 Sibulkin, M., "Heat Transfer Near the Forward Stagnation Point of a Body of Revolution, "J. Aeron. Sci., vol. 19, no. 8, Aug. 1952, p. 570.

14 Brown, W. B. and Livingood, J. N. B., "Solutions of Lamin

# 1960 ARS Meeting Schedule

Date	Meeting	Location	Abstract Deadline	
July 18-19	Liquid Rockets and Propellants Con- ference	Ohio State Univ.	Past	
Aug. 15–20	11th International Astronautical Congress	Stockholm, Sweden	Past	
Sept. 27–30	Power Systems Con- ference	Santa Monica, Calif.	Past	
Oct. 10–12	Human Factors and Bioastronautics Conference	Dayton, Ohio	Past	
Nov. 3-4	Electrostatic Propulsion Conference	Monterey, Calif.	Aug. 5	
Dec. 5-8	ARS Annual Meeting and Astronautical Exposition	Washington, D.C.	Aug. 25	

Send all abstracts to Meetings Manager, ARS, 500 Fifth Ave., New York 36, N.Y.

# Thrust Orientation Patterns for Orbit Adjustment of Low Thrust Vehicles

H. BROWN<sup>1</sup> and J. R. NELSON<sup>2</sup>

Flight Propulsion Laboratory, General Electric Co., Evendale, Ohio

Low thrust propulsion systems can be used for the precision adjustment of space vehicle orbit characteristics. The most effective application of these low levels of thrust requires the use of thrust orientation patterns peculiar to each type of mission. The thrust patterns most suitable for altitude correction, eccentricity reduction and Earth escape missions are identified and typical propulsion times indicated for each.

SPACE vehicles powered by low thrust propulsion systems —heat transfer, plasma and ion rockets—operate in a gravitational field orders of magnitude greater than the applied thrust. The path of the vehicle will at first closely resemble the conic section of an unperturbed orbit. The elements of the conic section, however, will be continuously changing due to the action of the applied thrust. Propulsion effects can be segregated from gravitational effects most effectively by a direct numerical integration of the osculating orbit elements (1).<sup>3</sup>

#### **Orbit Characteristics**

Six elements are required to completely define an unperturbed orbit in inertial space. A typical set of elements consists of: The semi-latus rectum and the eccentricity which define the geometry of the orbit, the inclination angle and the longitude of the node which define the orientation of the orbit plane, and the argument of the perigee and the time of perigee passage which define the orientation of the orbit in its plane. The location of the vehicle in its orbit is given by the true anomaly  $\phi$  which is a function of the orbit elements and the time. The thrust orientation angle  $\lambda$  will be measured from the radius vector to the thrust vector in the direction of rotation. It will be assumed to lie in the orbit plane.

The orbit elements are constant unless propulsive thrust or other perturbations are present. Except for short period oscillations, the elements defining the geometry of the orbit will be effected only by the propulsive thrust.

#### Resonance

The ability of the thrust to produce desired changes in the orbit elements is dependent predominantly upon the true

anomaly and the thrust orientation angle and also upon the values of the elements and the thrust to local vehicle weight ratio. The rates of change of each of the elements can be represented in the  $\lambda$ - $\phi$  plane as illustrated in Fig. 1 for the semi-latus rectum and the eccentricity. Note that the maximum rates of change occur at the midpoints of the positive and negative regions.

It is evident that the use of transverse thrust  $\lambda=90~{\rm deg}$  will result in a continuous increase in the semi-latus rectum and in oscillations in the eccentricity. Similar oscillations will occur in the argument of the perigee. Both the amplitude and the period of these oscillations will increase as the semi-latus rectum increases. A stable "resonance" condition is ultimately reached when the rate of change of the argument of the perigee is equal to the angular velocity of the vehicle. At this point, the true anomaly remains essentially constant—at a value less than  $90~{\rm deg}$ —and the eccentricity increases continuously. Similar resonance phenomena have been encountered with many of the other thrust patterns investigated.

#### Thrust Orientation Patterns

The orbit element characteristics illustrated in Fig. 1 can be used to define specific  $\lambda$ - $\phi$  relationships which will maximize the rate of change of a particular orbit characteristic. The  $\lambda$ - $\phi$  relationship for some of the thrust orientation patterns studied are illustrated in Fig. 2. These are:

1 Tangential, maximizes the rate of increase of total energy (2).

2 Transverse, maximizes the rate of increase of semi-latus rectum, a measure of angular momentum (3).

3 Radial, dissipates excess kinetic energy thereby providing a reduction in eccentricity (4,5).

4 Circularizing, maximizes the rate of decrease of orbit eccentricity.

5 Constant Eccentricity, provides a continual increase in semi-latus rectum without the increase in eccentricity that accompanies the use of the transverse thrust pattern.

6 Constant Perigee Altitude, provides a continual increase in orbit energy without the increase in perigee potential energy that accompanies the use of the tangential thrust pattern.

7 Maximum Eccentricity, the opposite of the circularizing thrust pattern.

The precise shape of the curves is dependent upon the physical shape of the orbit as indicated by the instantaneous eccentricity.

#### Earth Escape Mission Performance

The Earth escape mission shall be assumed to consist of the alteration of an initial low altitude-circular orbit to a parabolic orbit. The pattern identified for this mission will be suitable for both lunar and interplanetary missions. The propulsion system is required to increase both the eccentricity and the total energy of the orbit to the parabolic level. Atmospheric drag must be minimized by maintaining a constant or increasing perigee altitude.

Fig. 3 contains the results of escape mission calculations

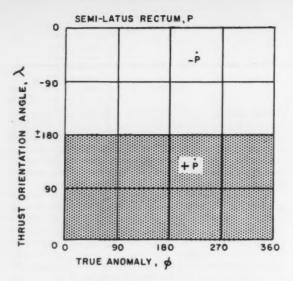
EDITOR'S NOTE: The Technical Notes and Technical Comments sections of ARS JOURNAL are open to short manuscripts describing new developments or offering comments on papers previously published. Such manuscripts are usually published without editorial review within a few months of the date of receipt. Requirements as to style are the same as for regular contributions (see masthead page).

Presented at the ARS Annual Meeting, Washington, D. C., Nov. 16–20, 1959.

<sup>&</sup>lt;sup>1</sup> Supervisor, Space Mechanics, Advanced Propulsion Systems. Member ARS.

 $<sup>^{2}</sup>$  Mission Analysis Engineer, Advanced Propulsion Systems. Member ARS.

Numbers in parentheses indicate References at end of paper.



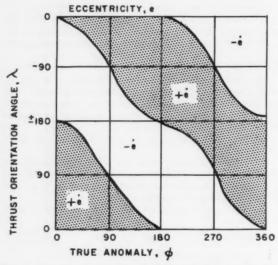


Fig. 1 Orbit element variation, in thrust orientation angle true anomaly plane

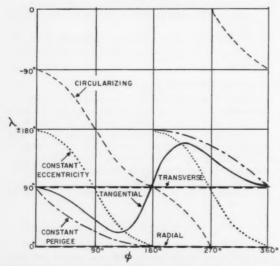


Fig. 2 Thrust orientation programs, in thrust orientation angle true anomaly plane

for a thrust to weight ratio of  $(10)^{-2}$ . The characteristic variation of eccentricity with semi-latus rectum is illustrated for the transverse, tangential, maximum eccentricity and constant perigee thrust orientation patterns. The most effective pattern for achieving the escape condition appears to be tangential thrust orientation.

A propulsion period of 12.25 hr is required for achieving an eccentricity of 1 from an initial 300-mile orbit with tangential thrust and a thrust to weight ratio of (10)<sup>-2</sup>. Calculations for thrust to weight ratios of (10)<sup>-3</sup> and (10)<sup>-4</sup> indicate corresponding times of 153 and 1886 hr, respectively. Escape appears to occur at the semi-latus rectum at which the thrust to local vehicle weight ratio is approximately 1 at 35,000, 110,000 and 375,000 miles for (10)<sup>-3</sup>, (10)<sup>-3</sup> and (10)<sup>-4</sup>, respectively. This is due to the resonance requirements.

ECCENTRICITY, e

Fig.

to

WOL

erro

and

star

teri of t

culs

430

18.5

of c

Sui

ties

orie mis alti

Ju

Although the eccentricity varies continuously during the mission, the actual path of the vehicle closely approximates a circular spiral.

#### **Eccentricity Correction Mission**

The eccentricity correction mission shall be assumed to consist of the alteration of an elliptical orbit resulting from satellite launch to a highly circular orbit. This might be required in order to eliminate guidance or propulsion errors resulting from the launching operation. The propulsion system is required to convert the excess kinetic energy of the elliptical launching orbit to potential energy in order to restore the balance required for a circular orbit.

A comparison of radial and circularizing thrust orientations indicate that eccentricity could be reduced more effectively by the use of the circularizing thrust pattern. Fig. 4 contains the results of several mission calculations with the circularizing thrust pattern. The initial orbit in each case had an eccentricity of 20 per cent and a semi-latus rectum of 25,000 miles.

For a  $(10)^{-2}$  thrust to weight ratio, thrust initiation at apogee appears to result in the minimum time required to circularize the orbit, 0.875 hr. It also results in an increase in orbit semi-latus rectum. For a  $(10)^{-3}$  thrust to weight ratio, thrust initiation at perigee resulted in an increase in the semi-latus rectum and the smaller propulsion time requirements.

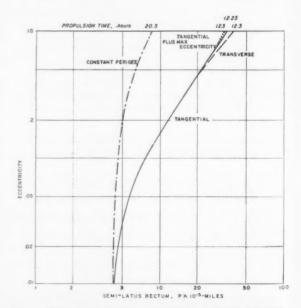


Fig. 3 Earth escape mission. Comparison of thrust orientation programs for thrust to weight ratio of (10)-2

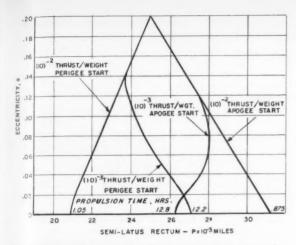


Fig. 4 Eccentricity correction mission. Comparison of starting positions for thrust to weight ratios of (10) -2 and (10) -1

#### **Altitude Correction Mission**

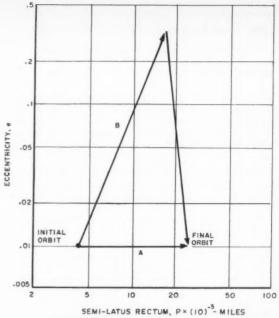
The altitude correction mission shall be assumed to consist of the alteration of an initial low altitude-near circular orbit to a higher altitude orbit of the same eccentricity. This would conceivably be necessary in order to eliminate launch errors or to augment booster capabilities. The propulsion system is required to increase the potential energy of the orbit and to remove any eccentricity developed during the process.

Fig. 5 contains the results of a comparison between the constant eccentricity and the transverse thrust orientation patterns for a thrust to weight ratio of  $(10)^{-2}$ . Note that the use of the transverse pattern must be followed by a period of circularizing thrust orientation. Initial semi-latus rectum was 4301 miles and terminal value 26,000 miles.

The desired altitude is achieved at constant eccentricity in 18.25 hr. The alternate program involves the use of transverse thrust for 9.5 hr, a coasting period of 5.8 hr and the use of circularizing thrust for 1.3 hr. This results in a total propulsion period of 10.8 hr.

### Summary

The precision adjustment of space vehicle orbit characteristies can be accomplished most effectively by the use of thrust orientation patterns peculiar to the requirements of the mission. Propulsion time requirements for converting a low altitude orbit to a parabolic escape orbit can be minimized by the use of tangential thrust orientation. Eccentric orbits can be converted most effectively into circular orbits by the use of



	THRUST PROGRAM	TIME, Hr	TOTAL TIME, HE
A	CONSTANT ECCENTRICITY	18.25	18.25
В	TRANSVERSE	9. 5 5. 8	
	CIRCULARIZE	1.3	16.6

Fig. 5 Altitude correction mission. Comparison of thrust orientation programs for thrust to weight ratio of (10) -2

the circularizing thrust pattern. Altitude corrections can be accomplished most effectively by the use of transverse thrust orientation, a coasting period and a period of circularizing thrust orientation.

#### References

- 1 Baker, R. M. L., Westrom, G. B., Hilton, C. G., Arsenault, J. L., Gersten, R. H. and Browne, E., "Efficient Precision Orbit Computation Techniques," ARS preprint 856-59, June 1959.
  2 Moeckel, W. E., "Continuous Thrust Trajectories," Space Technology Course Notes, NASA, Cleveland, 1958, Lectures 5 and 6.
  3 Levin, E., "Low Thrust Transfer Between Circular Orbits," pre-

- nology Course Notes, NASA, Cleveland, 1958, Lectures 5 and 6.

  3 Levin, E., "Low Thrust Transfer Between Circular Orbits," presented at ASME Aviation Conference, March 1959, preprint 59-AV-2.

  4 Copeland, J., "Interplanetary Trajectories Under Low-Thrust Radial Acceleration," ARS JOURNAL, vol. 29, no. 4, April 1959, pp. 267-271.

  5 Paiewonsky, B., "The Motion of an Orbiting Vehicle Subjected to Continuous Radial Thrust, Including a Study of Planetary Encounters," presented at the 10th IAF Congress, preprint 0/304.

# Minimization of Characteristic Velocity for Two-Impulse Orbital Transfer

H. MUNICK,1 R. McGILL2 and G. E. TAYLOR3

Grumman Aircraft Engineering Corp., Bethpage, N. Y.

Analytic solution is given to the problem treated by Lawden, that of optimum transfer from a point on an elliptical orbit to a circular orbit. More generally, the absolute minimum characteristic velocity path is given for transfer between two arbitrary terminals.

N 1925 Hohmann (1)4 first established the minimum characteristic velocity path between circular orbits. In recent years Lawden (2) gave a suggestive treatment to the more general problem of optimum transfer from a point on an elliptical orbit to a circular orbit. The following problem was first formulated by Vargo (3).

The problem treated here is that of finding the minimum characteristic velocity path between two co-planar terminals, and from a terminal to a "point." For the purposes of this paper a terminal is defined as a locus specified by a radial distance and a velocity vector. A "point" is specified by a velocity vector and a radius vector. The class of orbits considered is that for which the apogee of the ellipse corresponding to the initial terminal is less than the perigee of the ellipse corresponding to the final terminal. This is tantamount to saying that a minimum of two impulses is required to accomplish the transfer.

The formulation here essentially follows that of Lawden

#### **Analytical Treatment**

Consider the problem of optimum transfer of a space vehicle between two terminals in an inverse-square field. Let (u0, vo) be the velocity components of the first terminal at a distance  $\alpha$  from the attractive center. Let  $(u_F, v_F)$  be the velocity components of the second terminal at a distance  $\beta$  from the attractive center. At the first terminal an impulse is applied resulting in new velocity components  $(u_1, v_1)$ . The space vehicle then goes into a transfer orbit arriving at the second terminal with velocity  $(u_2, v_2)$ . Upon arrival at the second terminal a second impulse is applied adjusting the arrival velocity to the desired terminal velocity  $(u_F, v_F)$ . For such a maneuver the characteristic velocity is given by

$$\lambda^* = \sqrt{(u_1 - u_0)^2 + (v_1 - v_0)^2} + \sqrt{(u_2 - u_F)^2 + (v_2 - v_F)^2}$$
 [1]

From conservation of angular momentum

$$u_2 = (\alpha/\beta)u_1 \tag{2}$$

and from conservation of total energy

$$v_2^2 = \left(1 - \frac{\alpha^2}{\beta^2}\right) u_1^2 + v_1^2 + 2\mu \left(\frac{1}{\beta} - \frac{1}{\alpha}\right)$$
 [3]

Introduce dimensionless parameters x, y by

$$u_i = x_i \sqrt{\frac{\mu}{\alpha}}$$
  $v_i = y_i \sqrt{\frac{\mu}{\alpha}}$  [4]

Let the distance ratio r be defined by

$$r = \alpha/\beta$$
 [5]

After nondimensionalizing,5 the physical problem of mini-

This paper is an abridgment of preprint no. 959-59 presented at the ARS 14th Annual Meeting, Nov. 1959.

<sup>1</sup> Research Mathematician. Member ARS.

<sup>2</sup> Research Dynamicist. Member ARS.

<sup>3</sup> Research Engineer. Member ARS.

<sup>4</sup> Numbers in parentheses indicate References at end of paper.

<sup>5</sup> For complete mathematical details see ARS preprint 959-59.

mizing characteristic velocity becomes equivalent to the mathematical problem of minimizing

$$\lambda(x, y) = \sqrt{(x - x_0)^2 + (y - y_0)^2} + \sqrt{(rx - x_F)^2 + [\sqrt{(1 - r^2)x^2 + y^2 + 2(r - 1)} - y_F]^2}$$
 [6]

subject to

$$y_2^2 = (1 - r^2)x^2 + y^2 + 2(r - 1) \ge 0$$
  $0 < r < 1$  [7]

The domain of the independent variables (x, y) is then a region bounded by the ellipse given by Equation [7] and a circle of arbitrarily large radius (Fig. 1).

Now consider the region bounded by the ellipse  $y_2 = y_F$  and a circle of arbitrarily large radius (Fig. 2). For this region, from Equation [6] we have

$$\lambda(x,y) \ge \sqrt{(x-x_0)^2 + (y-y_0)^2} + \sqrt{(rx-x_F)^2} = \lambda_1(x,y)$$
 [8]

At an interior point in the region bounded by the ellipse  $y_2 =$  $y_F$  and a circle of arbitrarily large radius (Fig. 2),  $\lambda_1$  cannot have a relative minimum. This is so since the necessary condition that the partial derivatives of  $\lambda_1$  with respect to x and yvanish simultaneously requires that  $r^2 = 1$ , which is a contra-

Special consideration is given to the coordinate  $(x_0, y_0)$  and points along the line  $x = x_F/r$ . The point  $(x_0, y_0)$  must lie inside the boundary curve  $y_2 = 0$ , otherwise the transfer could be made using one impulse. The points along the line  $x = x_F/r$  will be treated subsequently.

Excluding the point  $(x_0, y_0)$  and points on the line x = $x_F/r$  from the region under consideration insures that both partial derivatives of  $\lambda_1$  exist at all points in the region. function  $\lambda_1$  (x, y) is continuous in and on the region. Since this region is closed, the function  $\lambda_1(x, y)$  will assume its least value somewhere in this region. However, since the function has no relative minima inside the region, it must assume this minimum value on one of the boundary curves. On the arbitrarily large outer boundary curve, we observe from Equation [8] that the function becomes arbitrarily large. The conclusion is that  $\lambda_1$  (x, y) assumes its least value on the curve  $y_2 = y_F$ .

For the region bounded by the curve  $y_2 = y_F$  and a circle of arbitrarily large radius, the smallest value that the function  $\lambda(x, y)$  can hope to attain would be at the point where  $\lambda_1$  (x, y)y) takes its least value. Since this point occurs on the curve  $y_2 = y_F$ ,  $\lambda(x, y)$  also takes its least value on this curve.

Now returning to the true domain given in Fig. 1, we have established that the minimum of  $\lambda(x, y)$  must lie in or on the annular region bounded by the curves  $y_2 = 0$  and  $y_2 = y_F$ (Fig. 2). This drastically reduces the number of possible candidates for the solution.

Investigating the partial derivative of  $\lambda(x, y)$  with respect to x we establish that this derivative is strictly positive along the line  $x = x_F/r$ . Therefore, since this derivative can never vanish along this line, points on the line are not valid candidates for a relative minimum.

Examining the partial derivatives of  $\lambda(x, y)$  on the curve  $y_2 = y_F$  we observe that for both derivatives to vanish simultaneously r must be equal to  $\pm 1$ . Since this is a contradiction we conclude that no relative minima exist on the curve  $y_2 = y_F$ .

Approaching the boundary curve  $y_2 = 0$  along rays parallel to the x axis we observe that in the immediate neighborhood of the boundary curve,  $\partial \lambda / \partial x \rightarrow -\infty$ . Therefore approaching the boundary curve  $y_2 = 0$  along rays parallel to the x axis forces  $\lambda(x, y)$  to increase. We conclude that on the boundary dary curve  $y_2 = 0$ ,  $\lambda(x, y)$  cannot assume its least value.

From these arguments it is finally concluded that the function  $\lambda(x, y)$  must assume a relative minimum at an interior point of the region bounded by the curves  $y_2 = 0$  and  $y_2 =$ 

#### Solution

We have been studying the mathematical problem of minimizing a nonlinear function of two variables subject to an inequality constraint. The foregoing analysis has proved the existence of an absolute minimum for the function at an interior point of a closed region. At this stage we are permitted to apply the necessary conditions for a solution, namely that both partial derivatives of the function  $\lambda(x, y)$  vanish simultaneously.

Setting both partial derivatives to zero, we deduce that a solution must satisfy

$$r^2x^2 - 2rx_Fy_2'x + [x_Fy_2' + (y_2' - 1)\sqrt{2/(1+r)}] \times [x_Fy_2' - (y_2' - 1)\sqrt{2/(1+r)}] = 0$$
 [9]

where  $y_2' = Y_2/y_F$ . Factoring yields

$$\left\{ rx - \left[ x_F y_2' + (y_2' - 1)\sqrt{2/(1+\tau)} \right] \right\} \times \left\{ rx - \left[ x_F y_2' - (y_2' - 1)\sqrt{2/(1+\tau)} \right] \right\} = 0$$
 [10]

From the first factor in Equation [10] and the expressions for the partial derivatives  $\partial \lambda / \partial x$ ,  $\partial \lambda / \partial y$  we conclude

$$\frac{y_2 - y_F}{rx - x_F} = \frac{y_F}{x_F + \sqrt{2/(1+r)}}$$
[11]

$$\frac{y-y_0}{x-x_0} = \frac{y_0}{x_0 + r\sqrt{2/(1+r)}}$$
 [12]

Equation [12] gives y as a linear function of x, and setting this linear function of x into Equation [11] yields a quadratic equation in x whose coefficients depend on the given data. We then solve analytically and determine two exact values of

Using the second factor in Equation [10] and proceeding as before we obtain

$$\frac{y_2 - y_F}{rx - x_F} = \frac{y_F}{x_F - \sqrt{2/(1+r)}}$$
[13]

$$\frac{y - y_0}{x - x_0} = \frac{y_0}{x_0 - r\sqrt{2/(1 + r)}}$$
 [14]

Similarly, the pair of equations [13 and 14] can be solved analytically yielding two more exact values of x. Using Equations [12 and 14], we determine the corresponding yvalues.

We have now determined analytically four solutions (x, y) to the minimum problem. For these four values of (x, y)there correspond four values of \(\lambda\). The smallest of these four values of  $\lambda$  is the absolute minimum for  $\lambda$ . This then gives the complete solution to the terminal-to-terminal problem first formulated by Vargo (3).

#### Acknowledgment

The authors express their gratitude to Derek F. Lawden whose fundamental insights proved extremely useful.

#### Nomenclature

u = normal component of velocity

= radial component of velocity

= nondimensional normal component of velocity just after first impulse

= nondimensional radial component of velocity just after 3/ first impulse

= initial radial distance

8 = final radial distance

= distance ratio,  $\alpha/\beta$ 

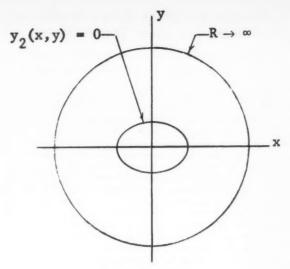


Fig. 1 True domain

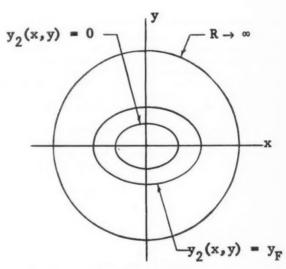


Fig. 2 Annular region

= nondimensional characteristic velocity

 $\lambda^*$  = characteristic velocity of transfer

 $\mu$  = gravitational constant

 $x_2$  = nondimensional normal component of arrival velocity

 $y_2$  = nondimensional radial component of arrival velocity

#### References

1 Hohmann, W., "Die Erreichbarkeit der Himmelskorper," R. Oldenbourg, Munich, 1925.
2 Lawden, D. F., "Entry Into Circular Orbits—1," J. Brit. Interplanet.
Soc., vol. 10, no. 1, Jan. 1951, pp. 5-17.
3 Vargo, L. G., "Optimal Transfer Between Two Coplanar Terminals In a Gravitational Field," preprint 58-20 presented at the Western Regional Meeting, American Astronautical Society, Aug. 18-19, 1958.

# Pierce Gun Design for an Accelerate-**Decelerate Ionic Thrust Device**

MANFRED J. RAETHER1 and ROBERT N. SEITZ2 Army Ballistic Missile Agency, Redstone Arsenal, Ala.

WITHIN the last few years, considerable interest has developed in the possibilities of ionic propulsion systems for low thrust space propulsion applications. Systems and missions analyses have indicated that specific impulse values ranging from 5000 to 10,000 sec will be desirable for ionic propulsion systems in the near future. For heavy ions, this corresponds to acceleration voltages ranging from about 1.6 to 6.4 kv. The current densities that can be obtained at these voltages for technically feasible acceleration structures are rather low (of the order of 1 to 3 ma/cm<sup>2</sup>). Consequently, large emitting areas or a large number of ion sources are required for high currents. This, in turn, results in a considerable increase in weight, volume and complexity.

These difficulties may be avoided to a certain extent by extracting the ions from the ion source with a high voltage and decelerating them to the desired lower voltage. If there is no interception of current by the acceleration electrode, no net power is consumed during the acceleration-deceleration proc-

### **Conditions for Effective Deceleration**

We shall now specify the conditions, under which an accelerate-decelerate technique is feasible. We consider a space charge flow in a parallel plane geometry (Fig. 1).

It will be assumed that the ions are emitted from the anode with zero initial velocity. In region (1) they are accelerated to the potential  $V_a$ . They now enter into region (2) with an initial energy eVa, where they are decelerated to the desired potential V.

The problem is now reduced to the discussion of space charge flow with finite initial velocities in a planar diode. This case has been treated by Fay, Samuel and Shockley (1).3 Their results will be briefly discussed in the following paragraphs.

We introduce the following dimensionless quantities

$$\xi = x/s$$
  $\phi = V/V_a$   $i = I/I_0$ 

where

$$I_0 = \frac{4}{9} \epsilon_0 \left(\frac{2e}{m}\right)^{1/2} \frac{V_a^{3/2}}{e^2}$$

coordinate in the direction of flow measured from the acceleration plane

= distance between the anode and acceleration planes

= distance between the acceleration and deceleration planes

= potential

= current density

absolute magnitude of the electronic charge

= ionic mass

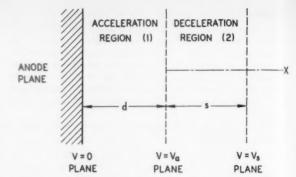
= permittivity of free space =  $8.85 \times 10^{-12}$  coulombs per €0

Mks units are used throughout this paper.

If we inject a space charge limited current into the deceleration region, i becomes  $s^2/d^2$ .

The quantity  $I_0$  is used as a convenient reference current density in the dimensionless ratio  $i = I/I_0$ .

In Fig. 2, the possible types of space charge flow are shown in an  $(i, \phi_s)$  diagram.  $\phi_s$ , the deceleration ratio, is the de-



f

C

C

H

be

80

gt

er

th

aI re

me

th

011

lin

wh

JU

Space charge flow in an accelerate-decelerate parallel plane geometry

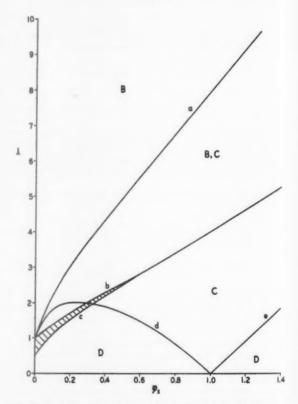


Fig. 2 Possible types of space charge flow in the deceleration region

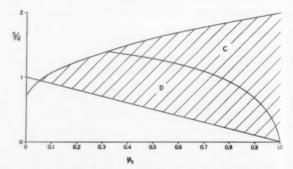


Fig. 3 Diagram of operating conditions for unimpeded space charge flow in the deceleration region (assuming space charge limited injection current)

Presented at the ARS Semi-Annual Meeting, June 8-11, 1959,

Presented at the Arts Semi-Annual Meeting, June 8-11, 1939, San Diego, Calif.

Research Physicist, Structures and Mechanics Laboratory.

Presently, Assistant Professor of Physics, Univ. of Illinois.

Research Physicist, Research Projects Laboratory. Member

<sup>&</sup>lt;sup>3</sup> Numbers in parentheses indicate References at end of paper.

celeration potential measured in units of the acceleration

In region B of this diagram, the potential has a minimum, and  $\phi_{\min} = 0$ ; i.e., a virtual anode is formed. Only part of the injected current is transmitted.

In region C, the potential also has a minimum, but  $\phi_{\min}$  > 0. All the injected current is transmitted. In region D, no minimum occurs; all current is transmitted.

In the overlapping regions B, C and B, C, D, all the respective types of space charge flow are possible, the actual flow pattern depending upon previous variations in the decelerating voltage. The shaded region does not permit stable operation.

If it is necessary that all the injected current be transmitted, we are restricted to the region between the curve c and the  $\phi_s$  axis. It is noted that, theoretically, the ions may be decelerated to zero velocity without loss in current. There may, however, be a practical limitation upon the deceleration ratio. It may be required that the field strength in the deceleration gap must not exceed the field strength in the acceleration gap. This would mean that

$$\frac{V_a - V_s}{s} \leq \frac{V_a}{d}$$

OF

$$s/d \geq 1 - \phi_s$$

Fig. 3 shows the region of interest in an  $(s/d, \phi_s)$  diagram for a space charge limited injection current. The choice of a point inside the shaded area specifies s/d and the deceleration ratio. It is seen, that based upon the foregoing assumption, the maximum practical deceleration ratio would be about 1:20.

#### Application of the Pierce Gun Design Principles

The rectilinear space charge flow discussed previously may be realized by applying the Pierce gun principle to both the acceleration and deceleration region (2) for a rectangular-slit gun geometry. [See Reference (2).] Fringe effects at the ends of the slit are neglected in this treatment.

We shall discuss the application of the Pierce gun design to the deceleration region for a special set of the parameters s/d and  $\phi_s$ . We choose s/d=1 and  $\phi_s=0.1$ ; this point lies within the D region. The potential distribution for the D region is given by (1)

$$\frac{s}{d} \cdot \xi = -\phi^{s/4} \psi \left[ \left( \frac{d}{s} \right)^{1/2} \frac{C}{\phi^{1/2}} \right] + \psi \left[ C \left( \frac{d}{s} \right)^{1/2} \right]$$

where  $(d/s)^{1/2}$   $C/\phi^{1/2}$  and  $C(d/s)^{1/2}$  are the respective arguments of the function  $\psi$ .  $\psi$  is defined by

$$\psi(x) = (1+x)^{1/2}(1-2x)$$

C is a constant of integration which must be determined from the boundary condition that for  $\xi = 1$ ,  $\phi = \phi_s = 0.1$ . For our special example we find

$$C = -0.2$$
  $\psi(C) = 1.25$ 

To obtain the electrode shapes, we follow the method outlined by Pierce and replace  $\xi$  by the complex quantity  $\xi + j\eta$ , where  $j = (-1)^{1/2}$ . We find

$$\frac{s}{d} \, (\xi \, + \, j \eta) \, = \, - \phi^{s/4} \psi \, \left[ \left( \frac{d}{s} \right)^{1/2} \frac{C}{\phi^{1/2}} \right] + \, \psi \left[ \left( \frac{d}{s} \right)^{1/2} \, C \, \right]$$

where  $\phi$  is now a function of  $\xi + j\eta$ .  $\phi$  can be separated into its real and imaginary parts

$$\phi(\xi + j\eta) = R(\xi, \eta) + jJ(\xi, \eta)$$

JULY 1960

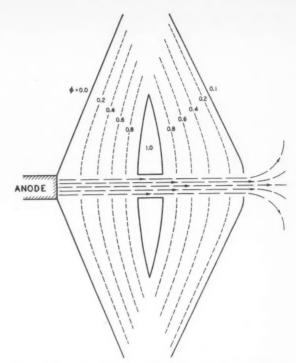


Fig. 4 Electrode configuration for accelerate-decelerate Pierce gun (10:1 deceleration ratio)

This yields

$$\begin{split} \xi + j \eta &= \psi \left[ C \left( \frac{d}{s} \right)^{1/2} \right] - \\ \sqrt{(R + jJ)^{1/2} + C \left( \frac{d}{s} \right)^{1/2}} \left[ (R + jJ)^{1/2} - 2 \left( \frac{d}{s} \right)^{1/2} C \right] \end{split}$$

In our special case, we have

$$\xi + j\eta = 1.25 - \sqrt{(R+jJ)^{1/2} - 0.2} \quad [(R+jJ)^{1/2} + 0.4]$$

This complex equation is equivalent to two real equations from which J must be eliminated. The curves  $R=R(\xi,\eta)=$  constant are then the equipotential lines. Any of these lines may be replaced by an electrode. The foregoing equation, however, does not allow a separation into its real and imaginary part in a convenient way. Therefore, it is better to retain J as a parameter and to present the curves in the parametric representation

$$\xi = \xi(R, J)$$
  $\eta = \eta(R, J)$ 

The inner and outer electrodes are given by

$$\begin{array}{lll} \xi = \xi(1,J) & & \eta = \eta(1,J) \\ \xi = \xi(0.1,J) & & \eta = \eta(0.1,J) \end{array}$$

respectively.

The equipotential lines have been calculated numerically, and the results are shown in Fig. 4, together with the Pierce gun design for the acceleration region.

Between the acceleration region and the deceleration region, a field-free gap remains. The length of this gap is completely arbitrary. However, the length of this gap, as well as the choice of beam width aperture, is contingent upon three major types of electrostatic beam distortion. First, distortion

arises because of the finite extent of the electrodes, which ideally should be infinite. This effect may be minimized by making the field-free gap as long as possible. Second, distortion arises because of the lateral divergence of the ion beam resulting from the mutual repulsion of the ions. This beam spreading effect is dependent upon beam width and depends also upon the length of the field-free gap. This type of distortion may be minimized by making the gap as short as possible. A third type of beam distortion is caused by the divergent-convergent lens effects resulting from the fringing fields at the entrance and exit apertures of the field-free space. It may be minimized by reducing the beam width. Thus, in choosing the length of the field-free gap, an optimum balance exists between the first and second types of distortion. In any event, the beam width should be as small as possible.

#### Conclusions

Since a number of simplifying assumptions have been made in deriving these results, this treatment cannot be regarded as more than a first approximation to a final lens design.

F n o li

to p

th ce

SU Z

so

loc

for

by

tix

en

fin

by

ac

the

the

tai

bo

flo

lin

bo

tio

Hu

ori

tra

dir

Ju

It should be borne in mind that maximum advantage may be realized from an accelerate-decelerate system only if practical structural limitations rather than voltage breakdown limitations determine the acceleration gap d. The available current densities are also limited by the current densities which may be obtained from the ion source.

#### References

1 Fay, C. E., Samuel, A. L. and Shockley, W., "On the Theory of Space-Charge Between Parallel-Plane Electrodes," Bell System Tech. J., vol. 17, 1938, p. 49.

2 Pierce, J. R., "Theory and Design of Electron Beams," Van Nostrand

Co., N. Y., 1954, chap. 10.

# **Magnetohydrodynamic Cavities**

BERNARD STEGINSKY1

Battelle Memorial Institute, Columbus, Ohio

Some features of magnetohydrodynamic cavity formation are discussed in qualitative terms. Examination of the dependence of the final steady-state configuration on the initial conditions in two cases reveals incompatibilities which may arise in the physical interpretation of the problem if a proper "model" is not specified.

SEVERAL theoretical papers have recently appeared dealing with the existence of cavities in magnetohydrodynamics (1-4).2 These cavities arise in connection with the flow of a perfectly conducting fluid past a magnetic field source such as, for example, a line current or a magnetic dipole. A perfectly conducting fluid cannot penetrate a region where the magnetic field is too strong, nor will such a fluid "support" diffusive transport of the field. Consequently, it is possible to demonstrate that the considered flow will result in the formation of a cavity region surrounding the source, around which the fluid flows as it would around a solid body, and in which the entire magnetic field strength is confined. The shape of the cavity-fluid boundary may be determined from the given distribution of current within the cavity, the prescribed type of external flow, and the condition of pressure equality across the interface.

In aerodynamic applications, we are usually interested in obtaining the steady-state solutions corresponding to a final equilibrium configuration. That is, we wish to determine the equilibrium shape of the cavity boundary subject to a given flow, without regard to the nature of the transient formation process from some initial state. All too often, therefore, the role of the initial conditions in determining the ultimate shape acquired by the cavity is overlooked. This oversight has already resulted in the appearance of a paradox in a recent treatment of the problem. The purpose of the present note is to clarify this particular aspect of the problem in qualitative terms.

Now let the fluid be suddenly endowed with infinite conductivity and a general motion past the stationary obstacle. With the start of the motion, in which all parts of the fluid participate, the magnetic lines of force will be swept downstream by the fluid. This follows from the theorem of magnetohydrodynamics which states that magnetic lines of force move about in a perfectly conducting fluid as though rigidly attached to the fluid particles. This sweeping motion

Received Feb. 1, 1960.

<sup>1</sup> Research Engineer, Aeronautics and Thermodynamics <sup>2</sup> Numbers in parentheses indicate References at end of paper.

In considering initial states of the fluid, we shall distinguish between the two limiting cases of zero conductivity and infinite conductivity. In both cases, however, the fluid will be assumed to be in an initial state of rest. When the conductivity of the fluid is infinite, a magnetic field source will produce a cavity region surrounding the source (a circular shape in the case of a line current), the interior of which contains the entire magnetic field but no fluid. At the cavity surface, the hydrostatic pressure outside balances the magnetic pressure just inside the surface. Cole and Huth (2) have studied this problem for the cases where the source is represented by a, a line current and b, a magnetic dipole (the limit of two approaching line currents). They have shown that, when an incompressible flow field is superposed on a, the original shape is distorted into an ellipse with major axis transverse to the direction of flow. The elliptical shape results from a compression of the cavity parallel to the flow direction, because of the increase in stagnation pressure and deficit in hydrostatic pressure at the points of maximum velocity. Although only the static solution for b was obtained, Cole and Huth indicate that the original shape for this case would not be much distorted by a flow.

The second case, of a nonconducting fluid, is fundamentally different from the first one in that there will be no cavity region to begin with, and the magnetic field will penetrate the whole fluid. We may then inquire as to the final configuration of the system if, suddenly, the fluid were endowed with infinite conductivity and a given motion. This problem, considerably more difficult than the previous one, has been

discussed qualitatively in (1 and 6).

The following idealized example will be used to illustrate the interaction between the fluid and the magnetic field leading to the formation of a cavity in the flow. Suppose that, in a nonconducting fluid which is at rest, there is placed a body having in its interior an arrangement of current-carrying coils. The magnetic lines of force pass continuously through the body surface and penetrate the surrounding fluid

results, however, in compression of the lines of force with a corresponding increase in magnetic pressure. The magnetic pressure tends to deflect the fluid away from a region of strong magnetic field concentration. Alternatively, the decay time of the component of fluid velocity transverse to magnetic lines of force varies inversely with the fluid conductivity. Therefore, motion across the lines of force will be annihilated almost instantaneously.

The system will very rapidly equilibrate to a state wherein

the following conditions are satisfied:

1 A cavity region forms around and behind the body, extending far down stream, through which the fluid cannot penetrate; the fluid velocity is tangent to the surface of the

2 The magnetic field is confined to this cavity region. since the field cannot penetrate a perfectly conducting fluid; the magnetic lines of force are tangent to the surface of the cavity, and a current sheet of infinite density forms on the

3 The external hydrostatic pressure balances the mag-

netic pressure across the cavity-fluid interface.

The above conditions, together with the given distribution of current in the body and a prescribed type of flow, are sufficient to determine the shape of the cavity. V. N. Zhigulev (3), making clever use of complex variables, recently solved the two-dimensional problem of this type for the flow past a line current. The flow was chosen to correspond to a Newtonian pressure distribution at the cavity surface.

The final equilibrium configuration could conceivably be achieved by the passage of a high speed shock wave through the initial system, as suggested by Burgers (1). The gas immediately behind the initial shock wave moves at a hypersonic speed which is slightly less than the propagation velocity of the wave. Therefore, a stationary bow shock wave forms ahead of the body. The hot, ionized gas generated by the initial shock wave possesses a relatively high conductivity and can therefore interact with the magnetic field emanating from the body.

Because the electrical conductivity of the fluid actually is finite in practice, the entire cavity region would be occupied by fluid in a state of rest or near-rest since leakage of the fluid across the magnetic force lines is possible. This region, where the essential strength of the magnetic field is concentrated, is

the so-called magnetic boundary layer.

Cavity shapes in perfectly conducting fluids may be obtained to a good approximation from solutions of magnetic boundary layer problems for very large, but finite, magnetic Reynolds numbers. Ludloff (5) has recently shown that the flow of a fluid of large magnetic Reynolds number past a line current results in the formation of a thin magnetic boundary layer which is greatly elongated in the flow direction. This result is markedly different from that of Cole and Huth for the case of a perfectly conducting fluid, in which an originally circular cavity experiences an elongation in the transverse direction and a contraction in the longitudinal direction.

This seemingly anomalous behavior may be resolved by

observing that the superposition of a flow on the two initial states produces a fundamentally different effect in each case, leading to dissimilar end results. In the first case, the conductivity of the fluid was assumed to be infinite prior to the onset of motion. Thus, the fluid cannot interact directly with the magnetic field, which is zero everywhere in the fluid, but distorts the original shape of the cavity by virtue of the redistribution of pressure on the boundary. In the second case, the conductivity of the fluid was considered to be zero in the rest state and only assumed an infinite value simultaneously with or after the commencement of flow. Therefore, in this case, the fluid can interact directly with the magnetic field and, in doing so, sweeps the magnetic force lines down-

In a recent paper, Sakurai (4) studied the problem of the "steady, two-dimensional hypersonic flow of an ideal gas with infinite electrical conductivity around a two-dimensional magnetic dipole, the axis of which is perpendicular to the direction of the uniform flow." The cavity region in the steady-state (or "frozen region," as Sakurai called it) was assumed to have a circular shape, and the magnetic field within the cavity was represented by the solution for the static magnetic dipole.

From a mathematical standpoint, the problem becomes overdetermined if, in addition to the condition of pressure equality at the interface, a given pressure distribution in the external flow and a given magnetic source distribution within the cavity, we also attempt to specify the shape of the cavity. Consequently, it must be assumed that the cavity shape is unknown and is to be determined from the conditions of the

In the light of the previous discussion, it would seem plausible to conclude that the steady-state cavity region could not assume as compact a shape as that of a circle unless the conductivity of the fluid were infinite initially, i.e., before the commencement of flow. In the opposite limiting case of a zero conductivity initially, we would expect the formation of an extended cavity region in the downstream direction. Although neither of the two cases examined is an exact representation of hypersonic flight conditions, the latter furnishes the more accurate "model" for the problem. It would then appear that Sakurai's specification of a circular cavity, apart from its inherent mathematical difficulty, is also incompatible with the conditions of hypersonic flight.

- 1 Landshoff, R. K. M. (Ed.), "Magnetohydrodynamics," Burgers, J. M., in "Penetration of a Shock Wave Into a Magnetic Field," Stanford University Press, Stanford, Calif., 1957, pp. 36-56.

  2 Cole, J. D. and Huth, J. H., "Some Interior Problems of Hydromagnetics," The Rand Corp., Rep. no. P-1695, May 8, 1959.

  3 Zhigulev, V. N., "On Magnetic 'Squeezing' of the Flow of a Conducting Medium," Doklady Akad. Nauk SSSR, vol. 126, no. 3, 1959, pp. 521-523.
- 4 Sakurai, T., "Two-Dimensional Hypersonic Flow of an Ideal Gas With Infinite Electric Conductivity Past a Two-Dimensional Magnetic Dipole," J. Aero/Space Sci., vol. 26, no. 12, 1959, pp. 841-842.
- 5 Ludloff, H. F., "Magnetic Boundary Layers," ARS JOURNAL, vol. 29. no. 8, 1959, pp. 590-591.

6 Steginsky, B., "Magnetohydrodynamics," Battelle Tech. Rev., vol. 9 no. 2, 1960, pp. 3-9.

# **Analytic Formulation for Radiating** Fins With Mutual Irradiation<sup>1</sup>

E. R. G. ECKERT,2 T. F. IRVINE Jr.3 and E. M. SPARROW<sup>2</sup>

Heat Transfer Laboratory, University of Minnesota, Minneapolis, Minn.

THE ABSENCE of convection in the operating environment of a space vehicle has directed attention to radiation as the primary or exclusive transferring mechanism for disposing of waste heat. Radiative collectors are also being proposed for capturing solar energy for power generation purposes. The use of finned surfaces, already a well-known technique in convection heat exchange equipment, is now being considered in the design of space vehicle radiators. The fins would not only augment the heat transfer characteristics of the radiator, but would also provide protection for the base surfaces against bombardment by space particles.

In studying the characteristics of a radiating-conducting fin, the first step which has been taken (1-4)4 is to suppose that there is no radiant interaction with adjacent fins or with the base surface. For such an isolated fin, the conservation of energy principle can be expressed as a differential equation, and results have been obtained for both the plane fin and the circumferential fin of constant thickness. In almost all real situations, there will be a radiant interchange between adjacent fins and with the base surface as well as with the external environment. Part of the radiation leaving a given fin will be intercepted by a neighboring fin or by the base surface, and, if the surfaces are nonblack, there will be reflections and re-reflections. The mathematical description of this complex interchange process, which includes both energy transfers from physically separate surfaces and heat conduction, must be made as an integro-differential equation. The formulation of such problems may be unfamiliar to many heat transfer investigators, and it is the purpose of this report to show how such an analysis is carried out. Prior consideration of the radiant interference between fin and base surfaces has been made in (3 and 5), but in an incomplete and restrictive

Before proceeding to the mathematical formulation, it is worth while to mention some general characteristics of radiating fins. Depending upon the radiation and conduction properties of the material and on geometrical parameters and orientation, the use of radiating fins may result either in an increase or in a decrease in heat transfer. For example, consider a plane wall which is of infinite length in the direction normal to the page [Fig. 1(a)]. For finite fin conductivity and black surfaces, the presence of fins definitely decreases the total heat transferred, relative to the unfinned situation. On the other hand, if the emissivity is less than 1, then it can be said that fins of infinite conductivity will definitely increase the total heat transfer, and that increases are also likely for a range of finite conductivities. As a second illustration, consideration is directed to the long, longitudinally finned cylinder shown in Fig. 1(b). Here, in contrast to the previous example, finning may increase the heat transfer even for finite fin conductivity and black surfaces. For nonblack surfaces, the remarks made in connection with Fig. 1(a) continue to apply. Thus, from this, there is indicated the need for careful analytical study prior to the use of radiative finned surfaces. It is evident that there will be a large number of parameters





Longitudinal fins on a plane surface

Longitudinal fins on a cylinder

Fig. 1 Some fin configurations

which will determine the heat transfer performance of radiating fins, more than are usually found in the convective case. Consequently, analysis of finned radiating surfaces may in many cases have to be carried out with a specific application in mind.

With this as background, we now proceed to describe the mathematical formulation for ensembles of radiating-conducting fins. Attention will first be focused on a fairly general in configuration; then, the governing equations will be given for some specific cases for which numerical calculations are now under way.

#### **General Mathematical Formulation**

The analytical approach to be presented here applies to a variety of geometrical configurations. But, for the sake of concreteness, the derivation will be carried out with reference to an easily visualized physical situation. Consideration is given to the conduction-radiation transfer process for a long circular cylinder which is finned either longitudinally or circumferentially as shown in Fig. 2, in (a) and (b) respectively. The longitudinal fins are assumed to be arranged symmetrically around the cylinder, whereas the circumferential fins are equally spaced along the length of the cylinder. Only a typical pair of neighboring fins is shown in the figures. The thermal conditions within the cylinder and in the external environment are uniform. The radiation coming from the environment is characterized by an equivalent black body radiation e (per unit area) passing uniformly through the area  $S_{\mathfrak{o}}$  connecting the tips of the fins (dashed line in Fig. 2). The surfaces of the fins and of the cylinder are taken as diffuse emitters and reflectors. The surface of the cylinder, i.e., the fin base surface, has a uniform temperature  $T_b$ . Initially, it will be assumed that the surfaces are gray  $(\alpha = \epsilon = 1 - \rho)$ , and also, that the fin surfaces are convex or plane, so that no surface element of a fin "sees" any other part of the same fin. The modifications associated with lifting these assumptions will be discussed later.

The starting point of our study is the basic principle of energy conservation. For steady-state conditions, the application of this law to the cross-hatched element of Fig. 2 yields

$$(Q_{\text{net}})_{\text{cond}} + (Q_{\text{net}})_{\text{rad}} = 0$$
 [1a]

The conduction term is evaluated in the usual fashion using Fourier's law, giving

$$- \frac{d}{dx} \left[ kA(x) \frac{dT(x)}{dx} \right] dx + (Q_{\rm net})_{\rm rad} = 0$$
 [1b]

To characterize the net radiation, it is of advantage to introduce two new quantities. [See (6), pp. 416-418.] First, there is B, which represents the combined radiant flux (emitted plus reflected) which leaves a position on the surface per unit time and area. The second quantity is H, which is the incident radiant flux at a position per unit time and area. With these definitions, the net radiant flux leaving the shaded

$$(Q_{\text{net}})_{\text{red}} = [B(x) - H(x)] dS_x$$
 [2]

Received Feb. 1, 1960.

<sup>1</sup> This work was supported by the Wright Air Development Center under Contract no. AF 33 (616)-5528.

<sup>2</sup> Professors of Mechanical Engineering. Members ARS.

<sup>3</sup> Professor of Mechanical Engineering, North Carolina State College. Members ARS. College. Member ARS.

<sup>4</sup> Numbers in parentheses indicate References at end of paper.

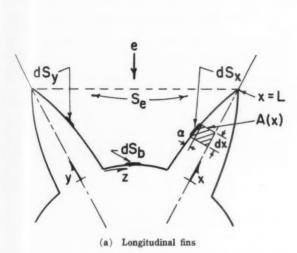
sh

bi

en

Co

th



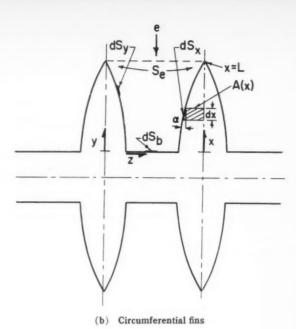


Fig. 2 Diagrams used in derivation of governing heat transer equations

From the geometry of Fig. 2,  $dS_x = l(x)dx/\cos \alpha$ , where l(x) is the fin perimeter. With this, the conservation of energy principle [1b] becomes

$$\frac{d}{dx} \left[ kA(x) \, \frac{dT(x)}{dx} \right] = \frac{\left[ B(x) \, - \, H(x) \right]}{\cos \, \alpha} \, l(x) \tag{3}$$

As it stands, Equation [3] contains three unknowns: T(x), B(x), and H(x). So, it is necessary to invoke other relationships between these quantities. First, we note that the combined radiant flux B leaving a surface is composed of two parts: Emitted energy and reflected energy. The emission is given by the usual expression

$$\epsilon \sigma T^4(x)$$

whereas the reflection is represented in terms of the incident energy and the reflectivity as

$$\rho H(x) = (1 - \epsilon)H(x)$$

With this, the definition of the combined flux B can be evaluated as

$$B(x) = \epsilon \sigma T^4(x) + (1 - \epsilon)H(x)$$
 [4]

The flux H which impinges on x is related to the energy coming from the external environment and to the flux leaving the other surfaces, i.e., the opposite fin and the base surface. Considering first the contribution of the opposite fin, we note that the radiant energy leaving a typical area  $dS_{y}$  in all directions is

$$B(y)dS_y$$
 [5a]

Of this, an amount

$$B(y)dS_ydF_{y-z} [5b]$$

arrives at x, where  $dF_{y-x}$  is the angle factor [see (6), pp. 396–398] under which  $dS_x$  is seen from y. Using the reciprocity relation  $dS_y dF_{y-x} = dS_x dF_{x-y}$ , expression [5b] becomes

$$B(y)dS_x dF_{x-y} ag{5c}$$

So, the energy impinging per unit area at  $dS_x$  due to radiation leaving  $dS_y$  is

$$B(y)dF_{x-y}$$
 [5d]

But,  $dS_x$  receives energy from all positions y, and hence, the total contribution of the opposite fin is found by integrating expression [5d] giving

$$\int_{S_y} B(y)dF_{x-y}$$
 [6]

In the same way, the contributions of the base surface and of the external environment to the incidence at  $dS_x$  can be formulated. With these, H(x) can be written as

$$H(x) = \int_{S_y} B(y)dF_{x-y} + \int_{S_b} B(z)dF_{x-z} + eF_{x-S_x}$$
 [7]

where it is to be remembered that  $dF_{x-y}$  is zero whenever x and y cannot see each other. Because of the symmetry, it is apparent that the distribution of the combined flux B over the right-hand fin will be the same as the distribution over the left-hand fin. So B(x) and B(y) are the same function; only the independent variables have been interchanged.

Summing up thus far, we find that it has been possible to augment the energy conservation Equation [3] with Equations [4 and 7] which essentially express conservation of radiant flux. But, in this process, the previous unknowns T(x), B(x) and H(x) have been joined by the radiant flux B(z) of the base surface. To make the problem determinate, additional flux conservation equations can be written for the base surface in a manner analogous to Equations [4 and 7]. The entire set of governing equations is [3, 4 and 7] and

$$B(z) = \epsilon \sigma T_b^4 + (1 - \epsilon)H(z)$$
 [8]

$$H(z) = 2 \int_{S_{-}} B(x)dF_{z-z} + eF_{z-S_{0}}$$
 [9]

To complete the statement of the problem, the following boundary conditions are prescribed:

When x = 0

$$T = T_b ag{10}$$

$$-k \frac{dT(x)}{dx} = \frac{B(L) - H(L)}{\sin \alpha}$$

OF

$$dT(x)/dx = 0 (1)$$

The second condition at x = L is usually taken as an approximation of the first one.

Once the geometry of the system has been specified, the angle factors F may be evaluated.5 Then, the set of five nonlinear integro-differential equations may be solved to obtain all heat transfer quantities of interest. For example, when B(x) and H(x) have been determined, the local heat loss may be found from Equation [2]. The solution of the governing equations will almost certainly have to be carried out numerically

To extend the equations to fins with concave surface, it is only necessary to add to the right side of Equation [7] a term which accounts for the irradiation of the element dSz by other parts of the surface of the same fin. For fins whose surfaces have absorptivities and emissivities which depend on wave length, Equations [4, 7, 8 and 9] are written for monochromatic radiation. Then, in Equation [3], B and H have to be introduced after integration over all wave lengths. The actual mechanics of carrying out such a calculation appears extremely involved.

For the special case of black surfaces ( $\epsilon = 1$ ), the first three governing equations can be solved without recourse to the last two. After rearrangement, Equations [3, 4 and 7] yield

$$\begin{split} \frac{d}{dx} \left[ kA(x) \, \frac{dT(x)}{dx} \right] &= \\ \frac{l(x)}{\cos \alpha} \left[ \sigma T^4(x) \, - \, \sigma \, \int_{S_y} T^4(y) dF_{z-y} - \, \sigma T_b{}^4F_{z-S_b} - \, eF_{z-S_d} \right] \, [12] \end{split}$$

This same derivation is also valid if pins, rather than fins, are used as the extended surfaces. It is only necessary to reinterpret the integral over  $S_v$  in Equations [7 and 12] as including the surface area of all of the pins which may be seen from the typical pin  $S_z$ . A similar interpretation is to be made of the integral over  $S_z$  in Equation [9].

#### Some Special Cases

The configuration of Fig. 2 has been useful for demonstrating the method of formulating the radiative fin problem, but it contains too many parameters to be an appropriate case for numerical study. Consequently, consideration is being given to two somewhat simpler configurations, Fig. 3(a) and (b), which still have practical utility and whose solutions should provide insight into the behavior of radiating fin ensembles. Fig. 3(a) represents a typical pair of longitudinal fins belonging to a group which are symmetrically arranged around the circumference of a long cylinder. As a simplification, the curved base surface has been neglected, but this should have small influence as long as the fin length L is markedly larger than the cylinder diameter. In Fig. 3(b), there are depicted two members of a set of circumferential fins which are arranged along the length of a cylinder. Once again, the base surface has been neglected.

The governing equations are obtained by specializing Equations [3, 4, 7, 8 and 9], which were derived in the previous section. Only the final dimensionless results are given here. For the radial fins of Fig. 3(a), the derivation yields

$$\frac{d^2\theta(\xi)}{d\xi^2} = N_o[B^*(\xi) - H^*(\xi)]$$
 [13]

$$\begin{split} H^*(\xi) &= (1/2) \int_0^1 B^*(\eta) \, \frac{\xi \eta (1 - \cos^2 \delta)}{(\xi^2 + \eta^2 - 2\xi \eta \, \cos \delta)^{3/2}} \, + \\ &\qquad \frac{N_\epsilon}{2} \left[ 1 - \frac{\cos \delta - \xi}{(1 + \xi^2 - 2\xi \cos \delta)^{1/2}} \right] \end{split} \quad [14]$$

$$B^*(\xi) = \epsilon \theta^4(\xi) + (1 - \epsilon)H^*(\xi)$$
 [15]

where

$$\begin{array}{lll} B^* &= B/\sigma T_b{}^4 \\ H^* &= H/\sigma T_b{}^4 \\ \theta &= T/T_b \\ \xi &= x/L \\ \eta &= y/L \\ N_c &= (L^2/kt)\sigma T_b{}^2 \\ N_s &= e/\sigma T_b{}^4 \end{array}$$

For the circumferential fin ensemble, Equation [15] remains unchanged, and Equations [13 and 14] are replaced by

$$\frac{1}{\xi} \frac{d}{d\xi} \left[ \xi \frac{d\theta(\xi)}{d\xi} \right] = N_e [B^*(\xi) - H^*(\xi)]$$
 [17]

$$H^{*}(\xi) = 2\gamma^{2} \int_{\tau_{1}^{*}}^{*1} B^{*}(\eta) \frac{\eta(\gamma^{2} + \xi^{2} + \eta^{2})}{[(\gamma^{2} + \xi^{2} + \eta^{2})^{2} - 4\xi^{2}\eta^{2}]^{3/2}} d\eta + \frac{N_{s}}{2} \left[ \frac{\gamma^{2} + \xi^{2} - 1}{[(\gamma^{2} + \xi^{2} + 1)^{2} - 4\xi^{2}]^{1/2}} \right]$$
[18]

where  $\gamma = h/L$  and  $r_i^* = r_i/L \ll 1$ . The boundary conditions on both problems are

$$\theta(0) = 1 \qquad d\theta/d\xi(1) = 0$$

Inspection of the governing equations shows that the solutions will depend on three parameters: The conduction parameter  $N_c$ , the environmental irradiation parameter  $N_c$ , and a geometric parameter—either the angle  $\delta$  or the aspect ratio  $\gamma = h/L$ . Numerical calculations are already under way, but there are no noteworthy results to report at this time.

- 1 Mackay, D. B. and Leventhal, E. L., "Radiant Heat Transfer from a Flat Plate Uniformly Heated on One Edge," North American Aviation, Inc., MD 58-187, Aug. 1958.
  2 Lieblein, S., "Analysis of Temperature Distribution and Radiant Heat Transfer Along a Rectangular Fin of Constant Thickness," NASA TN D-196, 1950.
- 1959.
  3 Bartas, J. G. and Sellers, W. H., "Radiation Fin Effectiveness," J. Heat Transfer, Trans. ASME, Series C, vol. 82, 1960, pp. 73-75.
  4 Chambers, R. L. and Somers, E. V., "Radiation Fin Efficiency for One-Dimensional Heat Flow in a Circular Fin," J. Heat Transfer, Trans. ASME, Series C, vol. 81, 1959, pp. 327-329.
  5 Callinan, J. P. and Berggren, W. P., "Some Radiator Design Criteria for Space Vehicles," J. Heat Transfer, Trans. ASME, Series C, vol. 81, 1959, pp. 327-344.
- pp. 237-244.
- 6 Eckert, E. R. G. and Drake, R., "Heat and Mass Transfer," McGraw-Hill Book Co., Inc., N. Y., 1959.

  7 Jakob, M., "Heat Transfer," vol. 2, John Wiley and Sons, Inc., N. Y.,

(a) Longitudinal fins

(b) Circumferential fins

Fig. 3 Simplified fin configurations

 $<sup>^{5}</sup>$  For surfaces of infinite extent normal to the page,  $dF_{x-y}=(1/2)d(\sin\varphi)$ , where  $\varphi$  is the angle between the normal at  $dS_{x}$  and the connecting line from  $dS_{x}$  to  $dS_{y}$ .  $dF_{x-z}$ ,  $dF_{x-x}$ ,  $F_{x-S_{z}}$ , etc. are found in the same way. [See Jakob (7), Eqs. 31-49.]

# Low Thrust Correction of Orbital Orientation

#### L. RIDER<sup>1</sup>

Convair (Astronautics), San Diego, Calif.

A method for performing small corrections of orbital orientation is described. It is found that the orientation parameters of inclination angle and nodal longitude can be varied by a low thrust device continuously applied perpendicularly to the orbital plane with sense of application reversed twice in every revolution.

IN A RECENT paper (1),<sup>2</sup> Lorell and Lass have determined that the effect of a constant radial perturbing force on the orbit of a satellite is to cause the line of apsides to advance while maintaining the apogee and perigee distances constant. In terms of our notation, the rate of advance of the line of apsides reduces to

$$2\pi\lambda\sqrt{1-\epsilon^2}$$
 radians per revolution [1]

where  $\lambda$  is the ratio of the perturbative accleration (assumed

## Derivation of Equations

Moulton (2) gives the rates of change of i and  $\Omega$  due to a normal disturbing acceleration W as

$$\frac{di}{dt} = \frac{r\cos(\nu + \omega)}{na^2\sqrt{1 - \epsilon^2}}W$$
 [2]

$$\frac{d\Omega}{dt} = \frac{r \sin{(\nu + \omega)}}{na^2 \sqrt{1 - \epsilon^2} \sin{i}} W$$
 [3]

in standard notation.

Conservation of angular momentum provides the relation

$$\frac{dt}{dy} = \frac{r^2}{c} \tag{4}$$

Substitution of Equation [4] in [2 and 3] and conversion to the present notation provides

$$\frac{di}{d\nu} = \lambda (1 - \epsilon^2)^2 \frac{\cos(\nu + \omega)}{(1 + \epsilon \cos \nu)^3}$$
 [5]

$$\frac{d\Omega}{d\nu} = \frac{\lambda(1-\epsilon^2)^2}{\sin i} \frac{\sin (\nu+\omega)}{(1+\epsilon\cos\nu)^3}$$
 [6]

Equations [5 and 6] can be integrated as

$$\int di = \lambda \left\{ \frac{(1 - \epsilon^2)}{2(1 + \epsilon \cos \nu)^2} \left[ \sin \nu \cos \omega - \left( \frac{1 - \epsilon^2}{\epsilon} \right) \sin \omega \right] + \frac{(1 + 2\epsilon^2) \sin \nu \cos \omega}{2(1 + \epsilon \cos \nu)} - \frac{3\epsilon \cos \omega}{(1 - \epsilon^2)^{1/3}} \arctan \left[ \left( \frac{1 - \epsilon}{1 + \epsilon} \right)^{1/2} \tan \frac{\nu}{2} \right] \right\}$$
[7]
$$\int d\Omega = \frac{\lambda}{\sin i} \left\{ \frac{(1 - \epsilon^2)}{2(1 + \epsilon \cos \nu)^2} \left[ \sin \nu \sin \omega + \left( \frac{1 - \epsilon^2}{\epsilon} \right) \cos \omega \right] + \frac{(1 + 2\epsilon^2) \sin \nu \sin \omega}{2(1 + \epsilon \cos \nu)} - \frac{3\epsilon \sin \omega}{(1 - \epsilon^2)^{1/2}} \arctan \left[ \left( \frac{1 - \epsilon}{1 + \epsilon} \right)^{1/2} \tan \frac{\nu}{2} \right] \right\}$$
[8]

In terms of eccentric anomaly E, these equations are

$$\int di = \lambda \left\{ \frac{\cos \omega}{2\sqrt{1 - \epsilon^2}} \left[ (2 - \epsilon \cos E + 2\epsilon^2) \sin E - 3\epsilon E \right] - \frac{\sin \omega}{2\epsilon} (1 - \epsilon \cos E)^2 \right\}$$
 [9]
$$\int d\Omega = \frac{\lambda}{\sin i} \left\{ \frac{\sin \omega}{2\sqrt{1 - \epsilon^2}} \left[ (2 - \epsilon \cos E + 2\epsilon^2) \sin E - 3\epsilon E \right] + \frac{\cos \omega}{2\epsilon} (1 - \epsilon \cos E)^2 \right\}$$

[10]

constant) to the gravitational acceleration at a distance from the center of Earth equal to the semimajor axis of the perturbed orbit.

In the present note, a method employing low thrust is investigated for the purpose of changing two other conventionally chosen parameters which describe the orientation of any orbit: Inclination and nodal angle. This method in conjunction with that found by Lorell and Lass provides a relatively simple way to adjust the orientation of any orbit using a low thrust device.

Assumptions for the analysis are a constant perturbing acceleration always applied normal to the orbital plane and those of a simplified two-body problem.

Received Feb. 9, 1960.

<sup>1</sup> Senior Research Engineer, Preliminary Design Group. Member ARS.

<sup>2</sup> Numbers in parentheses indicate References at end of paper.

#### **Determination of the Thrust Program**

### Maximum orientation parameter changes per revolution

If Equations [7 and 8] or [9 and 10] are evaluated over a complete revolution in an arbitrary orbit and if the thrust (perpendicular to the orbital plane) has a programmed sense as shown in Fig. 1, we obtain the maximum change in either of the orientation parameters as shown in Fig. 2. Generally, such a maximum change in one of the parameters will be associated with a nonzero change in the other parameter.

It is of interest to note from Fig. 2 that when  $\omega = \pi/2$ ,  $\Delta i = 4\lambda$ , i.e., the maximum change in inclination per revolution is independent of the shape (eccentricity) of the elliptic orbit.

Similarly, for  $\omega = 0$ ,  $\Delta\Omega = 4\lambda/\sin i$  and is independent of orbital eccentricity.

## Single orientation parameter changes

Circular orbits have the unique property that when the

sense of the perturbing acceleration is such that maximum inclination change occurs (see Fig. 3), no nodal change will occur. Alternately, when maximum nodal change is programmed, no inclination change occurs.

When  $\omega = 0$  and thrust is programmed for maximum inclination change in any elliptic orbit, no nodal change will

occur.

THRUST APPLIED OUT OF THE PLANE OF THE PAPER THRUST APPLIED INTO THE PLANE OF THE PAPER CHANGEOVER POINTS 0

#### MÁXIMUM INCLINATION CHANGE (Δi)

 $\Delta\Omega \neq 0$ 

 $\pi/2$ LINE OF NODES LINE OF APSIDES

#### MAXIMUM NODAL CHANGE (49) $\Delta i \neq 0$

LINE OF NODES LINE OF APSIDES

Fig. 1 Sense of normal thrust for maximum orientation changes (elliptic orbits)

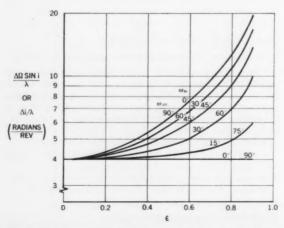


Fig. 2 Maximum inclination or nodal change per revolution

When  $\omega = \pi/2$  and thrust is programmed for maximum nodal change in any elliptic orbit, no inclination change will occur.

In general, for a single orientation change of particular magnitude (or a change of both orientation parameters of particular magnitudes), an interrupted thrust program and/ro a new location of the thrust change-over points must be determined. Equations [7 and 8] or [9 and 10] can facilitate the calculation of such a program.

#### Nomenclature

= orbital inclination

= longitude of ascending node

= perigee angle measured in the plane of the orbit from the ascending node to perigee  $\Delta i = \text{change in inclination per orbital revolution, radians per}$ 

revolution

 $\Delta\Omega$  = change in nodal longitude per orbital revolution, radians per revolution

= true anomaly

E= eccentric anomaly

= semimajor axis a

=  $\mu^3/a^2$ , acceleration of gravity at a distance equal to a = small constant perturbative acceleration applied perpen-

dicularly to the orbital plane

= Earth gravitational constant, GMe

= angular momentum per unit mass c

#### References

Lorell, J. and Lass, H., "Low Thrust Takeoff From Satellite Orbit,"
 ARS preprint 872-59, 1959.
 Moulton, F. R., "An Introduction to Celestial Mechanics," The Macmillan Co., N. Y., 1958, p. 404.

THRUST APPLIED OUT OF THE PLANE OF THE PAPER THRUST APPLIED INTO THE PLANE OF THE PAPER **CHANGEOVER POINTS** 0

#### MAXIMUM INCLINATION CHANGE (Ai)

 $\Delta\Omega = 0$ LINE OF NODES

#### MAXIMUM NODAL CHANGE (ΔΩ)

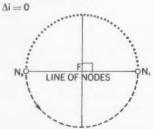


Fig. 3 Sense of normal thrust for maximum orientation changes (circular orbits)

J

# Some New Satellite Equations

#### RAIMOND A. STRUBLE<sup>1</sup>

North Carolina State College, Raleigh, N. C.

RECENTLY the writer has derived completely general equations of motion of a satellite relative to the true orbital plane, i.e., the plane which at each instant contains the satellite and its velocity vector. For the familiar gravitational potential

$$V = \frac{gR^2}{r} + \frac{JgR^4}{r^3} \left( \frac{1}{3} - \cos^2 \theta \right)$$
 [1]

they reduce (without approximation) to the third order system (see Fig. 1 for notation)

$$\frac{di}{d\beta} = -\frac{JgR^4u\cos^3i\sin i\sin 2\beta}{p^2 + JgR^4u\cos^4i(1-\cos 2\beta)} \eqno[2]$$

$$k \frac{d}{d\beta} \left( k \frac{du}{d\beta} \right) + u \sec^2 i =$$

$$\frac{gR^2}{p^2} + \frac{JgR^4u^2}{p^2} (1 - 3 \sin^2 i \sin^2 \beta) \quad [3]$$

where

0

p = angular momentum (constant) about the polar axis

$$k = \sec i + (2/p^2) JgR^4u \cos^3 i \sin^2 \beta$$

$$u = 1/r$$

It should be noted that the argument of the line of nodes  $\Omega$  does not appear at all, and hence the radial motion (orbit shape) is independent of the precessional motion of the orbital plane, a fact well-disguised by recent (approximate) satellite theories. On the other hand, the variations of i(the angle of incidence of the orbital plane) are of first importance to the

Received Feb. 15, 1960. Associate Professor of Mathematics.

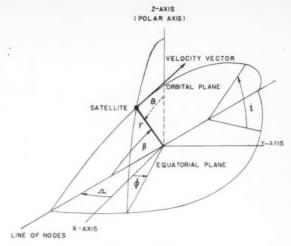


Fig. 1 Notation

radial motion. An exact orbit (corresponding to [1]) is prescribed by the system [2 and 3], and once it has been obtained, the (exact) precession of the orbital plane is given by a quadrature of

$$\frac{d\Omega}{d\beta} = \frac{JgR^4u\cos^3i\left(1-\cos2\beta\right)}{p^2 + JgR^4u\cos^4i\left(1-\cos2\beta\right)}$$
[4]

From [4] we see that the rate of regression of the line of nodes is not uniform but varies (in each half revolution of the satellite) from zero to approximately twice the familiar mean

Several facets of these equations which concern satellite engineering are to be developed in future papers.

# Simple Method for Approximating the Characteristics of Low Thrust **Trajectories**

PAUL D. ARTHUR,1 HANS K. KARRENBERG1 and HAROLD M. STARK<sup>2</sup>

Systems Corporation of America, Los Angeles, Calif.

OW THRUST trajectories are of interest for interplane-Thrus trajectories are of an area to the tary travel. Unfortunately, general solutions for these trajectories do not exist in closed form, and simple approximate solutions are needed. The method of trajectory approximation presented here is similar to perturbation methods standard to celestial mechanics. Only deviations from a reference ballistic (two-body) orbit are calculated. The first approximation to these deviations is the expected  $s = \frac{1}{2} \times$ at2. However, this expression is not sufficiently accurate for most purposes. More accurate approximations are derived in this paper.

#### **Derivation of Equations**

In the following presentation a simplified model of the solar system as discussed in (1),3 is assumed. The orbits of the planets are assumed to be co-planar concentric circles about the sun. During its interplanetary travels the vehicle is assumed to be solely under the gravitational influence of the sun's central force field. In addition, any thrust vector is assumed to lie in the plane of the planets' orbits. Thus, the motion is two-dimensional.

The vehicle acceleration A due only to the thrust vector Tis aligned at some angle  $\theta$  with respect to the radius vector from the sun as indicated in Fig. 1.  $A_r$  and  $A_c$  are the radial and circumferential components of A. The position of the vehicle at any time t is defined by a radius vector R and a polar angle o.

The equations of motion are

$$\frac{d^2R}{dt^2} - R\left(\frac{d\phi}{dt}\right)^2 = -g_0\left(\frac{R_0}{R}\right)^2 + A_r$$
 [1a]

$$\frac{1}{R}\frac{d}{dt}\left(R^2\frac{d\phi}{dt}\right) = A_c$$
 [1b]

Received Feb. 9, 1960. <sup>1</sup> Member Scientific Staff. <sup>2</sup> Member Scientific Staff.

Member ARS.

<sup>&</sup>lt;sup>3</sup> Numbers in parentheses indicate References at end of paper.

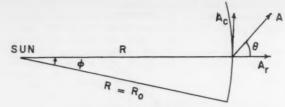


Fig. 1 Parameter definitions

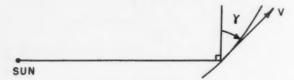


Fig. 2 Additional parameter definitions

where

 $R_0 = 1$  astronomical unit

 $g_0$  = gravitational acceleration of the sun at  $R_0$ 

Changing variables, as in (2, 3 and 4)

$$\tau = \frac{R}{R_0}$$
  $a = \frac{A}{g_0}$   $\tau = t \left(\frac{g_0}{R_0}\right)^{1/2}$   $\frac{dr}{d\tau} = \frac{dR/dt}{\sqrt{g_0 R_0}}$  [2]

Equations [1] thus become

$$\tilde{r} - r(\dot{\phi})^2 = -\frac{1}{r^2} + a_r$$
 [3a]

$$\frac{1}{r}\frac{d}{d\tau}\left(r^2\,\dot{\phi}\right) = a_c \tag{3b}$$

where the dots indicate differentiation with respect to  $\tau$ .

This ballistic (two-body) orbit which osculates with the actual trajectory at  $\tau=0$  will be used as a reference orbit. The equations of motion of this reference orbit are (subscript b denotes ballistic orbit)

$$\tilde{r}_b - r_b (\dot{\phi}_b)^2 = -\frac{1}{r_b^2}$$
 [4a]

$$\frac{1}{r_b} \frac{d}{d\tau} (r_b{}^2\!\dot{\phi}_b) = 0 \xrightarrow{\text{integrates to}} r_b{}^2\!\dot{\phi}_b = H$$
 [4b]

where  $\boldsymbol{H}$  is the constant angular momentum of the reference orbit.

Equations [3 and 4] may be combined as follows:

- 1 Define  $X \triangleq r r_b$  and substitute into Equation [3].
- 2 Subtract [4a] from [3a] and expand for  $X/r_b \ll 1$

$$\ddot{X} - r_b \left( 1 + \frac{X}{r_b} \right) (\dot{\phi})^2 + r_b (\dot{\phi}_b)^2 = \frac{2X}{r_b^3} + a_r$$
 [5a]

3 Integrate Equation [3b] and expand for  $X/r_b \ll 1$ 

$$r_b^2 \left(1 + \frac{2X}{r_b}\right) \dot{\phi} = \int_0^\tau r_b \left(1 + \frac{X}{r_b}\right) a_c d\tau' + H$$
 [5b]

4 Assuming  $r_b$  and  $a_c$  to be constants, Equation [5b] may be integrated from 0 to  $\tau$  and substituted into [5a]

$$\ddot{X} + \left[\frac{3H^2}{r_b^4} - \frac{2}{r_b^3}\right]X = \left[\frac{2Ha_c}{r_b^2}\right]\tau + a_r$$
 [6]

Using the fact that X = 0 = X at  $\tau = 0$ , Equation [6] may be integrated to obtain

$$X = \frac{C}{B} \left( \tau - \frac{\sin \sqrt{B} \tau}{\sqrt{B}} \right) + \frac{a_{\tau}}{B} (1 - \cos \sqrt{B} \tau)$$
 [7]

Expanding this solution into a series but collecting only the second- and third-degree terms in  $\tau$  (terms beyond  $\tau^{\sharp}$  are affected by the assumptions made earlier), we have

$$X = \frac{a_r \tau^2}{2} + \frac{H}{r_*^2} \frac{a_e \tau^2}{3}$$
 [8]

Now, from Equations [4b and 5b] we have

$$\frac{d\phi_b}{d\tau} = \frac{H}{r_b^3} \qquad \frac{d\phi}{d\tau} = \frac{r_b a_c \tau + H}{r_b^2 (1 + 2X/r_b)}$$
[9]

By integrating the difference between Equations [9]

$$r_b(\phi - \phi_b) = \frac{a_c \tau^2}{2} - 2 \frac{H}{r_b^2} \int_0^{\tau} X d\tau'$$
 [10]

Utilizing Equation [7]

$$r_b \left(\phi - \phi_b\right) = \frac{a_c \tau^2}{2} - 2 \frac{H}{r_b^2} \times \left[ \frac{C}{B} \left( \frac{\tau^2}{2} + \frac{\cos\sqrt{B}\tau}{B} - \frac{1}{B} \right) + \frac{a_r}{B} \left( \tau - \frac{\sin\sqrt{B}\tau}{\sqrt{B}} \right) \right]$$
[11]

Expanding this solution and collecting second- and third-degree terms

$$r_b \left( \phi - \phi_b \right) = \frac{a_c \tau^2}{2} - \frac{H}{r_b^2} \frac{a_r \tau^3}{3}$$
 [12]

Thus, Equations [7 and 11] in trigonometric form and Equations [8 and 12] in series form present the radial and circumferential deviations from the ballistic reference orbit.

The position of the vehicle has now been obtained; also useful are two additional parameters: The vehicle velocity V and the inclination angle  $\gamma$ . See Fig. 2.

Velocity may be obtained from an energy balance. The total energy at time  $\tau$  equals the energy of the ballistic reference orbit plus the subsequent work done by the radial and circumferential components of thrust as follows

$$\frac{V^2}{2} - \frac{1}{r} = \frac{V_b^2}{2} - \frac{1}{r_b} + a_r(r - r_{b \text{ at } r = 0}) + a_c \int_0^r r d\phi \quad [13]$$

Again neglecting higher degree terms, this equation becomes

$$\frac{V^2}{2} - \frac{1}{r} = \frac{V_b^2}{2} - \frac{1}{r_b} + a_r(r - r_{b \text{ at } \tau = 0}) + a_v \frac{H}{r_b} \tau \quad [14]$$

The parameter  $\gamma$  may be determined from a consideration of angular momentum. The angular momentum at time  $\tau$  equals the angular momentum of the ballistic reference orbit plus the angular momentum produced by the circumferential component of thrust as follows

$$rV\cos\gamma = H + a_e \int_0^{\tau} rd\tau' \qquad [15]$$

Substituting from Equation [8] and neglecting higher degree terms we have

$$\gamma = \cos^{-1}\left(H + a_c r_b \tau\right) / rV \tag{16}$$

Summarizing, the parameters r,  $\phi$ , V and  $\gamma$  have been determined as functions of  $\tau$ . The parametric assumptions made in the derivation were that  $a_{\tau}$  and  $a_{\varepsilon} = \text{constant} \ll 1$ , that  $X/r_b \ll 1$ , and that  $r_b = \text{constant}$ .

m

at

da

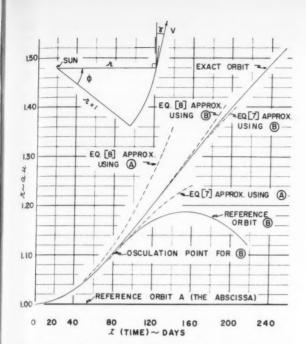
tw

re

m

tic

JU



31

)]

)]

Fig. 3 Approximate and exact characteristics of departure trajectories from Earth's orbit for  $a_r = \frac{1}{8}$  and  $a_c = 0$ 

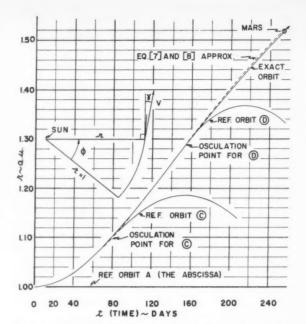


Fig. 4 Approximate and exact characteristics of a trajectory from Earth's orbit to Mars' orbit for  $a_7=\frac{1}{8}$  and  $a_c=0$ 

#### Comparisons of Approximate and Exact Trajectory Characteristics

Analytic solutions to the general equations of motion (Eq. [3]) cannot be determined. However, Copeland (3, 4), has determined analytic solutions for the case of radial thrust only. His analytic solutions for  $a_7 = \frac{1}{8}$  (this value is approximately  $0.8 \times 10^{-4}$  Earth surface g) will now be utilized for comparison with the foregoing approximate solutions.

Exact and approximate solutions of r as a function of t are presented in Fig. 3. The dashed line approximations which range from 0 < t < 150 days are solutions of Equations [7 and 8], where the reference ballistic orbit is taken as Earth's orbit about the sun  $(r_b = 1 \text{ for all } t)$ . It may be seen that at  $t \approx 79$  days the differences between the approximations of Equations [7 and 8] and the exact solution are  $\Delta r \approx 0.002$  and  $\Delta r \approx 0.014$ , respectively.

Another ballistic reference orbit, specified by the requirement that its point of osculation coincide with the exact orbit at r=1.10 ( $t\approx 79$  days), was determined from the equations of (1) and is also presented in Fig. 3. Approximations from Equations [7 and 8] are presented in the range 79 < t < 200 days and were found to be more accurate than those corresponding to the previous range. For example, at  $t\approx 158$  days (time from osculation plus 79 days) the differences between the approximations of Equations [7 and 8] and the exact solutions are only  $\Delta r \approx 0.001$  and  $\Delta r \approx 0.005$ , respectively.

Figs. 4 and 5 present an important application of the foregoing approximations. The fact that new reference orbits may be periodically determined from the approximate equations permits the calculation of trajectories which closely agree with the exact solutions for long periods of time. This procedure was used to calculate a trajectory for the distance to Mars.

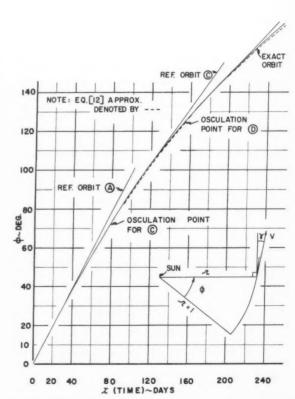


Fig. 5 Approximate and exact characteristics of a trajectory from Earth's orbit to Mars' orbit for  $a_\tau=\frac{1}{8}$  and  $a_c=0$ 

 $<sup>^4</sup>$  In Equation [7] a constant value of  $r_b$  was assumed. The value chosen was approximately an average value for the time interval of interest.

Experience gained from the calculations for Fig. 3 dictated the use of Equation [7] because of its initial accuracy for the departure phase of the trajectory and the use of Equation [8] because of its extreme simplicity for the remaining phases. New reference orbits were calculated at  $t \approx 79$  days and  $t \approx$ 153 days. The results, r and  $\phi$ , are presented as a function of t in Figs. 4 and 5, respectively.

The deviations at the distance of Mars ( $r \approx 1.52$ ) per parameter interval for the time interval  $0 \le t \le 253$  days were

$$\frac{\Delta_{\rm r}}{1.52 - 1.00} = 0.8 \text{ per cent}$$
  $\frac{\Delta \phi}{173.5 - 0} = 0.9 \text{ per cent}$ 

From another viewpoint, the deviation in time between the approximate and exact solutions at r = 1.52 is approximately 2.3 days out of 255.3 days. Although not presented, excellent comparisons were also obtained for V and  $\gamma$ .

These results are quite suitable for feasibility studies or preliminary engineering estimates. Although these results were obtained for the case of radial thrust only, it is felt that similar results could be obtained for the general case of constant thrust at an arbitrary angle  $\theta$ . Unfortunately, no accurate numerical solutions of these latter cases were available for comparative purposes.

The equations of this paper can also be applied to other

types of trajectories. For instance, trajectories utilizing variable thrust programs may be approximated by a sequence of steps of constant thrust at a given angle. Another type of trajectory for which the simple approximate methods are ideally suited is a ballistic trajectory which utilizes application of low thrust for corrective maneuvers.

The foregoing results are not limited to heliocentric applications. In fact, planetocentric maneuver or escape trajectories may be obtained from the previous calculations of heliocentric trajectories by merely changing the gravitational constants. For example, if we wish to consider geocentric orbits, we need only let Ro equal 1 Earth-radius and go equal the gravitational acceleration of the Earth at  $R_0$ .

The authors wish to express appreciation to Dr. A. Kartveli, Vice President of Republic Aviation Corp., for permission to publish this analysis.

#### References

1 Karrenberg, H. K. and Arthur, P. D., "Interplanetary Ballistic Orbits,"
ARS preprint 870-59, 1959.
2 Tsien, H. S., "Take-Off from Satellite Orbit," Jet Propulsion, vol. 23, no. 4, July-Aug. 1953, pp. 233-236.
3 Copeland, J., "Interplanetary Trajectories Under Low Thrust Radial Acceleration," ARS JOURNAL, vol. 29, no. 4, April 1959, pp. 267-271.
4 Karrenberg, H. K., "Note on 'Interplanetary Trajectories Under Low Thrust Radial Acceleration'," ARS JOURNAL, vol. 30, no. 1, Jan. 1960, pp. 130-131.

# Normal Dispersion of a Re-Entry Body

R. A. NORLING

Bendix Corp., Advanced Development Lab., South Bend,

A solution is obtained for the normal dispersion or displacement of a re-entry body from its static path due to a small aerodynamic trim misalignment for the planar case. An expression is obtained which relates the normal dispersion as a variable function of altitude. The solution has been further simplified for selected parameters of the ballistic factor  $\beta$  and re-entry path angle  $\gamma_E$ .

ONSIDER a nonspinning re-entry body on the straight CONSIDER a nonspinning recent of the trajectory shown in Fig. 1. Furthermore, assume that the body possesses an inherent trim misalignment  $\alpha_T$ . Since it has been shown in (1)2 that the effect of oscillatory terms on the normal displacement is negligible provided that the re-entry body is relatively stable, the angle of attack for our purposes can be considered constant  $\alpha = \alpha_T$ , i.e., equal to the trim angle.

As the body penetrates into the sensible atmosphere, the straight line nature of the trajectory will be altered by virtue of the perturbing lift forces resulting from the small trim angle  $\alpha_T$ . The base or static velocity can be represented by the expression derived in (2)

$$V = V_E e^{-a\overline{\rho}}$$
  $(V_E = \text{re-entry velocity})$  [1]

$$a = \text{static trajectory parameter}^3 = \rho_{S.L.} g/2c\beta \sin \gamma_E$$
 [2]

$$\bar{\rho}$$
 = atmospheric density ratio,  $\rho/\rho_{S-L} = e^{-cy}$  [3]

 $a = \text{static trajectory parameter}^3 = \rho_{S. L.} g/2c\beta \sin \gamma_E$ 

Received Jan. 29, 1960. <sup>1</sup> Chief Engineer, Applied Sciences Laboratory. Member ARS

Numbers in parentheses indicate References at end of paper. \* The  $\beta$  in this expression is not to be confused with the definition given in (1).

For the planar case, the transverse equation of motion for small trim angles becomes

$$-mV\dot{\gamma} = (1/2)\bar{\rho}\rho_{S.L.}V^{2}C_{L\alpha}\alpha_{T}A \qquad [4]$$

St 7b

Si

fui

lin

Si

by

Ei(

Fo

ter

tion

equ

Jui

In this equation,  $\gamma$  is considered as the deviation from a straight line trajectory, and along with its derivatives, to be of perturbation order. Equation [4] can be rewritten in the

$$-V\dot{\gamma} = \left(\frac{C_{L\alpha}}{C_D}\right)\alpha_T \frac{g\rho_{S-L}}{2\beta} \bar{\rho}V^2 \qquad [5]$$

Measuring time from the initiation of re-entry, the velocity normal to the trajectory and in the plane of the resulting lift force becomes

$$\dot{\xi} = \int_0^t -V\dot{\gamma}dt = \left(\frac{C_{L\alpha}}{C_D}\right) \frac{\alpha_{Tg}\rho_{S-L}}{2\beta} \int_0^t \overline{\rho} V^2 dt$$
$$\frac{d\overline{\rho}}{dt} = \frac{d\overline{\rho}}{dy} \frac{dy}{dt} = -\frac{d\overline{\rho}}{dy} V \sin \gamma_E$$

which when combined with Equation [3] give

$$dt = d\bar{\rho}/c\bar{\rho}V \sin \gamma_E$$
 [6]

Performing the change of variable, the normal velocity becomes

$$\label{eq:energy} \dot{\xi}(\overline{\rho}) \,=\, \left(\frac{C_{La}}{C_D}\right) \,\alpha_T \, \frac{g \rho_{S \cdot L}}{2c \beta \, \sin \, \gamma_E} \int_0^{\overline{\rho}} \, e^{\,-\, a \, \overline{\rho}} \, d\overline{\rho}$$

assuming that  $\bar{p} \to 0$  as  $y \to \text{high}$ . Upon integration the preceding equation yields

$$\dot{\xi}(\tilde{\rho}) = (KV_E/a)(1 - e^{-a\rho})$$
 [7a]

where

$$K = \left(\frac{C_{L\alpha}}{C_D}\right) \alpha_T \frac{g\rho_{S-L}}{2c\beta \sin \gamma_E}$$
 [7b]

Similarly, the normal displacement becomes

$$\xi = \int_0^t \dot{\xi} \, dt = \frac{K V_E}{a} \int_0^{\overline{\rho}} (1 - e^{-a\overline{\rho}}) \left( \frac{d\overline{\rho}}{c\overline{\rho} V \sin \gamma_E} \right)$$

which upon integration and substitution of limits yields

$$\xi(a\overline{\rho}) = \frac{K}{ac \sin \gamma_E} \left[ \int_0^{a\overline{\rho}} \frac{e^{a\overline{\rho}} d(a\overline{\rho})}{a\overline{\rho}} - (\ln a\overline{\rho} - \ln 0) \right] \quad [8]$$

The first term which appears in the brackets may be rewritten in the following manner

$$\int_{0}^{a_{\overline{\rho}}} \frac{e^{a_{\overline{\rho}}} d(a_{\overline{\rho}})}{a_{\overline{\rho}}} = \int_{0}^{-\infty} \frac{e^{a_{\overline{\rho}}} d(a_{\overline{\rho}})}{a_{\overline{\rho}}} + \int_{-\infty}^{a_{\overline{\rho}}} \frac{e^{a_{\overline{\rho}}} d(a_{\overline{\rho}})}{a_{\overline{\rho}}} = \lim_{z \to 0} \int_{z}^{+\infty} \frac{e^{-a_{\rho}} d(a_{\overline{\rho}})}{a_{\overline{\rho}}} + Ei(a_{\overline{\rho}})$$
[9]

where  $Ei(a\bar{p})$  is the exponential integral of argument  $a\bar{p}$ . Sub-tituting Equation [9] into [8] and recognizing that the Euler constant may be written as (3)

$$-\gamma = \lim_{z \to 0} \left[ \int_z^{\infty} \frac{e^{-t}}{t} dt + \ln z \right] = -0.5772$$

We obtain the result

$$\xi(a\overline{\rho}) = \frac{K}{ac \sin \gamma_E} \left[ Ei(a\overline{\rho}) - \ln a\overline{\rho} - \gamma \right]$$

Substituting the appropriate values for K and a (Eqs. [2 and 7b]), we obtain the expression

$$\xi(a\bar{\rho}) = \left(\frac{C_{L\alpha}}{C_D}\right) \left(\frac{\alpha_T}{c \sin \gamma_E}\right) [Ei(a\bar{\rho}) - \ln a\bar{\rho} - \gamma]$$
 [10]

Similarly, we may rewrite the expression for the normal velocity (Eq. [7b]) as

$$\dot{\xi}(a\overline{\rho}) = \left(\frac{C_{L\alpha}}{C_D}\right) \alpha_T V_E \left(1 - e^{-a}\right)$$
 [11]

Equation [10] expresses the normal deviation from a straight line trajectory for a small trim condition in terms of tabulated functions. The equation is subject to the restrictions imposed by the assumption that re-entry occurs along a straight line, i.e., gravity is neglected (2).

### **Simplified Approximation**

Equation [10] can be rewritten in terms of an infinite series by noting that (4)

$$Ei(a\bar{\rho}) = 0.5772 + \ln(a\bar{\rho}) + a\bar{\rho} +$$

$$\frac{(a\bar{p})^2}{2!2} + \frac{(a\bar{p})^3}{3!3} + \frac{(a\bar{p})^4}{4!4} + \dots$$

then

$$Ei(a\bar{p}) - \ln(a\bar{p}) - 0.5772 = a\bar{p} \left[ 1 + \frac{a\bar{p}}{212} + \frac{(a\bar{p})^2}{313} + \dots \right]$$

For  $a\bar{\rho} \leq 0.4$ , the error is 11 per cent or less if all higher degree terms are neglected. Equation [10] then becomes

$$\xi(a\overline{\rho}) = \left(\frac{C_{L\alpha}}{C_D}\right) \left(\frac{\alpha_T}{c\sin \gamma_E}\right) a\overline{\rho}$$
 [12]

assuming that

$$\rho_{S.L.} = 0.0027 \text{ slug/ft}^3$$

$$g = 32.2 \text{ fps}^2$$

$$c = 1/23,500 \text{ ft}^{-1}$$

we obtain  $a=1020/\beta\sin\gamma$ . Therefore, for the approximation [12] to be valid to within 11 per cent, the following inequality must be satisfied

$$\beta \sin \gamma_E/\bar{\rho} \ge 2540 \tag{13}$$

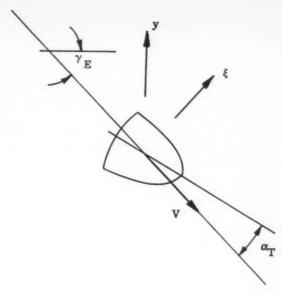


Fig. 1 Re-entry geometry

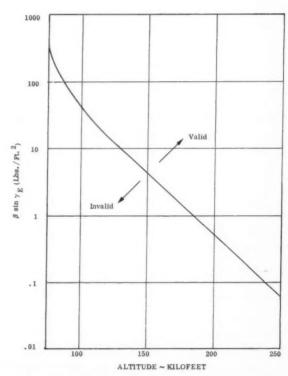


Fig. 2 Valid values of  $\beta \sin \gamma_E$  for approximate solution

Fig. 2 is a graph of the inequality [13] indicating the region where the approximate expression [12] is valid.

In terms of the trajectory parameters, Equation [12] becomes

$$\xi = 24 \times 10^6 \left(\frac{C_{L\alpha}}{C_D}\right) \left(\frac{\alpha_T}{\beta \sin^2 \gamma_E}\right) \bar{\rho}$$
 [14]

An approximate expression can be similarly obtained for the velocity expression [11] by expansion of the exponential

$$\begin{split} \dot{\xi} &= \left(\frac{C_{L\alpha}}{C_D}\right) \alpha_T V_B \left[1 - \left(1 - a\bar{\rho} + \frac{(a\bar{\rho})^2}{2} - + \ldots\right)\right] \\ \dot{\xi} &\cong \left(\frac{C_{L\alpha}}{C_D}\right) \alpha_T V_B a\bar{\rho} \end{split}$$

Letting  $a = 1020/\beta \sin \gamma_E$ , the expression for the normal velocity becomes

$$\dot{\xi} = 1020 \left( \frac{C_{L\alpha}}{C_D} \right) \left( \frac{\alpha_T V_B}{\beta \sin \gamma_E} \right) \bar{\rho}$$
 [16]

Equations [14 and 16] represent simplified expressions for the normal displacement and velocity histories in the plane, which include the resultant lift and drag forces. These forces may not be coincident with the plane of the trajectory, and, therefore, the normal dispersion described here will, in general, manifest itself as a combined range and azimuth error to the overall missile trajectory. The dispersion described here may be greatly attenuated by spinning the missile about its longitudinal axis, thereby averaging out the lift perturbation about that axis. For most bodies, the constant nature of the aerodynamic quantities  $C_{L\alpha}$  and CD are maintained for continuum flow for Mach numbers in excess of 4. The altitudes at which a certain velocity or Mach number occurs remain a function of  $\beta$  by virtue of Equation [1].

#### Nomenclature

static trajectory parameter, ps. L. g/2c\(\theta\) sin \(\gamma E\)

Acharacteristic area, ft2

atmospheric density term, 1/23,500, ft-1 drag coefficient, assumed constant  $C_{L\alpha} = \text{lift curve slope (1/radian), assumed constant}$ 

acceleration of gravity defined in Equation [7a]

mass of re-entry body, slugs

time, sec

 $V_E =$ initial re-entry velocity velocity, fps, VEe-ap

W weight of re-entry body, lb

altitude, ft 21

 $\alpha_T =$ trim angle, radians

ballistic factor,  $W/C_DA$ , assumed constant B re-entry path disturbance, Euler constant

initial re-entry path angle

displacement normal to the static re-entry path

= atmospheric density ratio,  $\rho/\rho_{S.L.}$ = atmospheric density,  $\rho_{S.L.}$   $e^{-cy}$ . [See (5)]

 $\rho_{S.L.} = \text{sea level density, } 0.0027 \text{ slug/ft}^3$ 

#### References

1 Allen, H. J., "Motion of a Ballistic Missile Angularly Misaligned With the Flight Path upon Entering the Atmosphere and Its Effect upon Aerodynamic Heating, Aerodynamic Loads and Miss Distance," NACA TN 4048, Oct. 1957.

TN 4048, Oct. 1957.

2 Allen, H. J. and Eggers, A. S., "A Study of the Motion and Aerodynamic Heating of Missiles Entering the Earth's Atmosphere at High Supersonic Speeds," NACA TN 4047, Oct. 1957.

3 Snedden, I. N., "Special Functions of Mathematical Physics and Chemistry," Interscience Pub., Inc., N. Y., 1956, p. 12.

4 E. Jahnke and F. Emde, "Tables of Functions," Dover Pub., Inc.,

N. Y., 1945, p. 2.

5 Chapman, D. R., "An Approximate Analytical Method for Studying Entry Into Planetary Atmospheres," NACA TN 4276, May 1958.

# Structural Effects and Particle Content of Interplanetary Space

L. REIFFEL<sup>1</sup>

Armour Research Foundation, Chicago, Ill.

Calculations on structural damage by solar plasmas are presented which show that solar helium is the dominant influence in sputtering, whereas solar hydrogen dominates radiation damage effects. Newly available laboratory data are used to calculate erosion rates in space.

KNOWLEDGE of the particle content of interplanetary space is important to our understanding of a wide variety of astrophysical phenomena. Information on densities, velocity distributions and chemical composition of the interplanetary gas also assumes significance in evaluating the effect of the environment of space on manmade structures, especially those involving thin sections or surface films. We have treated some of these effects previously (1).2 Estimates on most important parameters of the interplanetary medium have been largely inferential, as discussed in (1). Generally, protons and electrons are considered to be present in equal number densities ranging from 102 to 103 per cm3 under quiet solar conditions to perhaps 105 per cm3 in intense streams

issuing from an active sun. Corresponding velocities, suggested by time correlations between solar and terrestrial events as well as other data, appear to lie between 500 and 1500 km per sec or more. The magnitude of the velocity under quiet conditions is unfortunately particularly uncertain. Note that a proton velocity of 1000 km per sec corresponds to an energy of 5 kev.

Direct measurements on the density of particles in interplanetary space have apparently not yet been carried out, with the exception of one set of observations made by the The Russian results indicated densities fluctuating between 102 and 103 particles per cm3. It is interesting to note that these fluctuations did not show any obvious correlation with interplanetary magnetic field fluctuations on which observations were also made. Attempts to measure the velocities of the particles in the interplanetary gas were not successful.4

In our earlier work, both radiation damage and sputtering effects on thin films or surface coatings for average conditions and encounters with intense streams issuing from an active sun were considered. In treating sputtering effects, we originally employed an average sputtering yield  $\beta$  ( $\beta$  = number of atoms per incident ion) of unity, while explicitly noting the uncertainty of the value and the simplicity of scaling to other values of yield as more complete data became available. Recently, Grønlund and Moore (7) have made an extensive study of the sputtering of silver by hydrogen and helium using

din 9

in

in

so

m

G

ot

gre

ele

ah

th

du

de

wh

arı

of

Dro

Ju

Received Feb. 18, 1960.

<sup>&</sup>lt;sup>1</sup> Director of Physics Research, Physics Division. Member

Numbers in parentheses indicate References at end of paper. <sup>3</sup> We take this opportunity to note some pertinent referen (2 through 6), accumulated since the submission of (1) to ARS JOURNAL.

<sup>4</sup> Information on the USSR measurements of particle densities, magnetic field fluctuations and attempts at velocity measurement was provided for the author by L. I. Sedov and V. I. Krasovskii during conversations in Chicago, Nov. 20, 1959. Unfortunately, information on Soviet estimates of the average interplanetary gas density was not obtained.

magnetically analyzed ion beams. Their results, for normal incidence, indicate substantially lower yields than have been obtained heretofore by gas discharge methods, such as employed by Wehner (8). The discrepancy apparently arises from the presence of heavy ions in the gas discharge which are avoided by use of analyzed beams. The gas discharge technique can also be modified to eliminate the effects of undesired ions and may be combined with spectroscopic detection methods to provide a very sensitive means of measuring yields near threshold (9). Wehner's measurements indicate that threshold values of about 50 ev are appropriate for most materials; yields in the neighborhood of threshold are  $\beta = 10^{-4}$  to  $10^{-5}$ , but rise very rapidly to values of the order of  $\beta = 10^{-1}$  for energies  $\geq 150$  ev.

Grønlund and Moore's detailed study of Ag covered the range 2 to 12 kev, in which range  $\beta$  exhibits a broad and flat maximum for light bombarding ions. At 5 kev, \$\beta\$ for H+ is 0.035, whereas for He<sup>+</sup>,  $\beta$  is 0.48. Thus normal incidence sputtering by helium is 14 times that due to hydrogen, a ratio which is roughly maintained over the entire energy range studied. It is important to note that with the high  $\beta$  for He<sup>+</sup> as compared with H<sup>+</sup>, the sputtering of objects in space will actually be dominated by solar helium (10). This rather surprising result occurs if helium travels along with hydrogen in the outward streaming solar gas and if relative abundances characteristic of the solar atmosphere are retained in the streams. Aller (11) has recently suggested a relative atomic abundance for H/He of 7/1 as the best estimate available.

The overall effect of using the new absolute values for  $\beta$ including the effects of solar helium is to give an effective  $\beta$ to be used with proton density figures of 0.1 at normal incidence. To account for increased yields at other than normal incidence [for some materials  $\beta$  at 30 deg is 10 times  $\beta$  at 90 deg (9)], a good average value for the effective  $\beta$  of a 1000 km per sec solar stream is probably about 0.2 for materials similar to silver. This is one fifth the yield assumed previously and therefore reduces the sputtering rates given in (1) for any particular proton density by a factor of 5.

Were we to include effects of the heavy element admixture in the extended solar corona, using the same assumptions as we applied to He+ and H+ computations, the sputtering rates would be increased somewhat. Unfortunately, the gaps in our knowledge of the details of heavy element concentration, acceleration and sputtering efficiency are all very great, so that even rough estimates of the erosion are difficult to make. However, besides their work with H+ and He+ Grønlund and Moore have measured yields for a variety of other ions bombarding Ag surfaces at 5 kev and find for N<sup>+</sup> $\beta$ is 4.0, for  $O^+\beta$  is 4.4 and for  $Ne^+\beta$  is 5.5. Thus, the efficiency of sputtering for ions of mass 20 is roughly 160 times greater than for protons. The average atomic weight for the heavy elements in the solar atmosphere may be taken as roughly 32, and the relative abundance, by weight, for these elements appears to be about 2 per cent (1) so their numerical abundance is of order 10<sup>-3</sup>. If we simply assume that the heavy components behave as 5-kev neon ions, then it follows that the sputtering they cause, when compared with that produced by solar protons and helium, will result in an increase in erosion rates not exceeding 10 per cent. Ignoring this contribution tends to compensate for somewhat reduced proton densities which would be inferred from those observations which depend upon electron densities and charge neutrality arguments.

Using  $\beta = 0.2$ , the calculated time for complete removal of an optically opaque, 300-A thick, silver film under bombardment by a 1000 km per sec solar stream containing 600 protons per cm3, with accompanying heavier ions, is readily shown to be  $1.5 \times 10^7$  sec or 6 months. It is of interest to compare this result with etching rates derived from meteorite

cosmic ray age information, since in such a calculation one can avoid assumptions about absolute sputtering yields and particle densities. Whipple and Fireman (12) have recently suggested an upper limit etching rate of 30 Å per year for an iron meteorite in an orbit near that of Earth. The calculation was based on a cosmic ray age, for the particular meteorite fall (Sikhote-Alin) involved, of 5 × 108 years together with a cosmic ray attenuation length of 72 cm. Work by Fisher and Schaeffer (13) using argon, helium and neon age data5 has meanwhile shown that the correct age for the meteorite is nearer 1.7 × 108 years. This has the effect of raising the etching rate limit to about 100 Å per year for an evenly exposed spherical body. For an oriented iron surface, the erosion rate limit would then be 400 Å per year. The relative sputtering rate for Ag is two to three times higher than that for Fe if results for bombardments with 400-ev argon ions are typical (9). Thus, the erosion limit, from meteoritic data, for an oriented Ag surface would be 800 to 1200 Å per year as compared with the result calculated here of 600 Å per year. Uncertainties in meteoritic etching rate information are unfortunately considerable for reasons discussed elsewhere (10) and because of questions concerning cosmic ray constancy in time and attenuation length in iron

The radiation damage calculations given in (1) remain essentially unchanged by the present considerations, since the particle densities are of the same order as used previously. Thus charring of plastics or other organic materials to depths of a few thousand angstroms in short times is to be expected. For thin films, such effects could be quite significant. Changes in inorganic surface coatings, as a result of color-center and defect production and similar radiation induced phenomena, are also to be anticipated. In addition to being a function of particle density, the importance of any of these possibilities is directly dependent on the velocity and hence the range of the incident ions. If actual velocities are much lower than those used in the computations, the smaller depths in which radiation induced changes would then be produced might make them tolerable. However, calculations using only a considerably reduced particle density figure (e.g., 10 to 100 particles per cm³) would still suggest appreciable radiation effects with many materials. Final conclusions on both sputtering and radiation damage effects must await direct measurements on the density, velocity and chemical composition of the interplanetary gas as a function of solar activity.

- 1 Reiffel, L., "Structural Damage and Other Effects of Solar Plasmas," ARS JOURNAL, vol. 30, no. 3, March 1960, pp. 258-262.
  2 Rees, M. H. and Reid, G. C., "The Aurora, the Radiation Belt and the Solar Wind: A Unifying Hypothesis," Nature, vol. 184, 1959, p. 539.
  3 Gold, T., "Plasma and Magnetic Fields in the Solar System," J. Geophys. Res., vol. 64, 1959, pp. 1665-1674.
  4 Parker, E. N., "Extension of the Solar Corona into Interplanetary Space," J. Geophys. Res., vol. 64, 1959, pp. 1675-1681.
  5 Biermann, L. and Lust, R., "Radiation and Particle Precipitation Upon the Earth From Solar Flares," Proc. Inst. Radio Engrs., vol. 47, 1959, pp. 209-210.

- pp. 209-210.
  6 Whipple, F. L., "Solid Particles in the Solar System," J. Geophys.
- 6 Whipple, F. L., "Solid Particles in the Solar System," J. Geophys. Res., vol. 64, 1959, p. 1655.
  7 Grønlund, F. and Moore, W. J., "Sputtering of Silver by Light Ions With Energies from 2 to 12 kev," J. Chem. Phys., to be published.
  8 Wehner, G. K., "Advances in Electronics and Electron Physics," vol. 7, Academic Press, N. Y., 1955, p. 289.
  9 Wehner, G. K., "Recent Developments in the Field of Sputtering," Invited paper no. R5, American Physical Society Meeting, N. Y., Jan. 29, 1969.

- 1960.
  10 Reiffel, L., "Erosion of Meteorites and the Density of Interplanetary Gas," Nature, vol. 185, 1960, p. 821.
  11 Aller, L. H., private communication.
  12 Whipple, F. L. and Fireman, E. L., "Calculation of Erosion in Space From the Cosmic-Ray Exposure Ages of Meteorites," Nature, vol. 183, 1820.
- 1959, p. 1315.
  13 Fisher, D. E. and Schaeffer, O. A., "Cosmogenic Nuclear Reactions in Iron Meteorites," Bull. Amer. Phys. Soc., Series II, vol. 5, 1960, p. 23.
  14 Whipple, F. L., private communication.

nd

c.,

ng

d

V

n.

r-

t.

10

ıg

0

Γ-

n

re

ne

g

ıs

re

re

]-

g

0

e.

e

g

L

<sup>&</sup>lt;sup>5</sup> The author is indebted to Dr. Fisher for helpful comments and communication of results on Sikhote-Alin prior to publication.

# Magnetic Effect in a T-Tube

BOYD W. HARNED

General Electric Co., Evendale, Ohio

Data observed with five return lead variations in a T-tube electromagnetic plasma accelerator have been analyzed for a possible correlation between energy conversion efficiency and geometrical configuration. An attempt has been made to separate out the magnetic portion of the total accelerative process.

AFURTHER analysis of data (1)<sup>2</sup> on the conversion of electrical energy to kinetic energy of air contained in a

Brass electrodes separated by a 30-mm gap in a 39-mm ID Pyrex T-tube were connected to a 10- $\mu$ f capacitor source through a triggered spark gap switch. In order to determine the nature of the effect of the magnetic field at the gaseous discharge of the ordinary backstrap configuration (2), several other return lead connections were made to provide a variation of magnetic field. Air pressure before discharge was held at 250  $\mu$  of mercury, and capacitor energy in all cases was 500 joules.

If the T-tube is visualized in Cartesian coordinates with the electrodes along the x axis and the desired magnetic field which repels the discharge along the y axis, then the exhaust arm of the T-tube will extend along the z axis. Ordinarily, the backstrap is parallel to the electrode alignment in the x direction, and the y component of the field at the arc is produced because of the circular pattern of the magnetic field due to the discharge current passing through the strap. Five cases will be reported here:

 $1\,$  The return lead located so as to minimize the magnetic field at the discharge—"no field" case.

2 A length of  $\frac{1}{4}$ -in. copper tubing used as a backstrap in the x direction.

3 A two-turn coil wound of copper tubing, one on either side of the discharge section of the tube, so that the magnetic field is in the *y* direction.

4 A four-turn coil similar to that of case 3, with two turns on either side of the tube and the magnetic field in the y direction.

5 A two-turn coil similar to that of case 3 but oriented with one turn in front and one behind the discharge in order to provide a field in the z direction and thus accelerate the gaseous conductor in the y direction—"wrong field" case.

The data reported were: Frequency of the discharge ringing circuit, inductance and resistance calculated from the damped wave form observed with an oscilloscope, velocity of the accelerated gases as observed by a photomultiplier through an aperture system and a "light pipe," and momenta of the gases as observed by means of a lightweight plastic disk pendulum. From these data were calculated an energy conversion efficiency value. The T-tube was shorted out completely so that the inductance and resistance of the external circuit could be observed and subtracted from the values in the various return lead cases, thus providing an estimate of how the added circuit inductance affected the action. Reproducible velocity data were obtained which showed a variation with distance along the exhaust tube, as reported by Kolb (2) and Kash et al. (3). All measurements referred to here apply to a distance of 18 cm from the discharge, accounting in part for the low efficiencies

Shown in Table 1 are data for the five cases. The resistance values are exclusive of external circuit; the velocity values are those of the first shock only, although subsequent shocks

Table 1 Operating characteristics Configurations 2 1 5 3 52.6 64.5 51.2 37.0 51 2 Frequency, kc/sec 0.064 0.0830.024 0.032 0.049 T-tube discharge resistance, ohms 3 7 7 4 5.8 Efficiency, per cent 4 4 1.0 Velocity, cm per 1.51 0.93 1.65 1.26 1.80 microsec Energy dissipated in T-tube dur-125 56 85 131 90 ing first half cy-

cle, joules

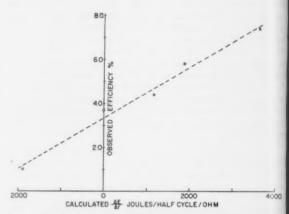


Fig. 1 Energy per unit resistance vs. efficiency for various T-tube configurations

due to successive current maxima in the ringing contributed to the observed momenta. Dissipated energy values are calculated from observed circuit parameters. Resistance and inductance values of the gaseous discharge must be considered as average values throughout the energy dissipation process. T-tube resistance includes that of the electrodes, excluding the return lead.

The equation of motion for a partially or fully ionized gas (4) subjected to combined electric and magnetic fields contains two terms of interest here, namely, a pressure gradient term and a j x B term. It seemed possible that the data would provide a means of separating these two terms in crude fashion, if a few simple assumptions might be imposed. Since ringing frequencies differed in all these cases, and hence current values and magnetic fields varied with time, an attempt was made to correlate the data in terms of energy dissipated in the T-tube during the first half cycle of the discharge. This seems reasonable, since it is assumed that the first shock, whose velocity is reported, is caused by the first half cycle of the current. Case 1, the "no field" case, served as a criterion for the pressure gradient term, by which the additional T-tube circuit resistances and dissipated energies observed for the other cases with magnetic fields were obtained by subtraction. A ratio was made of these energy differences divided by the resistance differences and was plotted against the efficiencies observed. Since the "wrong field" case 5 deflected the arc perpendicularly to the exhaust direction and resulted in a reduced efficiency, this case was plotted as a negative effect. The resulting curve is shown in Fig. 1.

(Continued on page 705)

Supervisor, Plasma Propulsion Unit, Flight Propulsion Laboratory Department.

<sup>&</sup>lt;sup>2</sup> Numbers in parentheses indicate References at end of paper.

us

ed alnd ed ss. he
as nnt ta de ce
pt ed ge. k,
of on be he
ies ered he

5) AL